



CHARACTERIZATION OF NOISE TECHNOLOGY RADAR (NTR)
SIGNAL DETECTABILITY USING A NON-COOPERATIVE RECEIVER

THESIS

Daniel V. Atienza, Captain, USAF

AFIT/GE/ENG/11-01

DEPARTMENT OF THE AIR FORCE
AIR UNIVERSITY

AIR FORCE INSTITUTE OF TECHNOLOGY

Wright-Patterson Air Force Base, Ohio

APPROVED FOR PUBLIC RELEASE; DISTRIBUTION UNLIMITED.

The views expressed in this thesis are those of the author and do not reflect the official policy or position of the United States Air Force, Department of Defense, or the United States Government. This material is declared a work of the U.S. Government and is not subject to copyright protection in the United States.

AFIT/GE/ENG/11-01

CHARACTERIZATION OF NOISE TECHNOLOGY RADAR (NTR)
SIGNAL DETECTABILITY USING A NON-COOPERATIVE RECEIVER

THESIS

Presented to the Faculty
Graduate School of Engineering and Management
Air Force Institute of Technology
Air University
Air Education and Training Command
in Partial Fulfillment of the Requirements for the
Degree of Master of Science in Electrical Engineering

Daniel V. Atienza, B.E.E.E.
Captain, USAF

March 2011

APPROVED FOR PUBLIC RELEASE; DISTRIBUTION UNLIMITED.

AFIT/GE/ENG/11-01

CHARACTERIZATION OF NOISE TECHNOLOGY RADAR (NTR)
SIGNAL DETECTABILITY USING A NON-COOPERATIVE RECEIVER

Daniel V. Atienza, B.E.E.E.
Captain, USAF

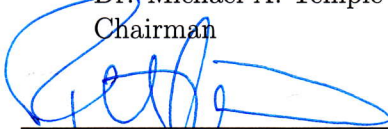
Approved:



Dr. Michael A. Temple
Chairman

9 Mar 2011

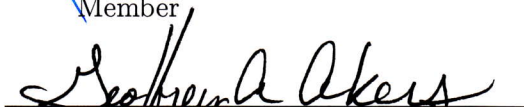
Date



Dr. Peter J. Collins
Member

8 MAR 2011

Date



Maj. Geoffrey A. Akers, PhD
Member

8 Mar 2011

Date

Abstract

The basic concepts for implementing today's Noise Technology Radar (NTR) were first introduced circa 1950. However, practical implementability was severely limited early on due to the computational intensity of analog signal correlation. Subsequent advances in Digital Signal Processing (DSP) have greatly reduced the computational complexity of signal correlation using a Fast Fourier Transform (FFT) and increased algorithm efficiency for performance optimization. This has revived NTR development to the point where it is now a near-worldwide activity, with deployment likely to occur in the not too distant future. This has gotten the attention of Radio Frequency Intelligence (RFINT) researchers who are tasked with ensuring the arsenal of Radio Frequency (RF) situational awareness tools remains up to date; as new NTR technology emerges so does the need for non-cooperative, non-matched filter detection and exploitation.

There are two distinct veins of ongoing research at AFIT involving NTR technology, including: 1) NTR *developmental* work aimed at improving NTR performance from a *cooperative* radar detection perspective and 2) NTR *exploitation* work aimed at assessing NTR exploitability using *non-cooperative* detection methods—the focus of this research. Activity in these areas is based on AFIT's Noise Network (NoNET) radar system that is an integrated group of NTR nodes with centralized processing for data acquisition, digital processing, and multi-sensor image fusion. The NTR nodes operate in Continuous Wave (CW) mode and transmit low power signals with random temporal-spectral structure. Thus, the signals inherently possess characteristics that are commonly associated with Low Probability of Detection/Intercept (LPD/LPI) waveforms.

As adopted for this research, Quadrature Mirror Filter Banks (QMFB) have been effectively used for non-cooperatively detecting *structured* LPD/LPI waveforms and extracting various waveform characteristics (modulation, pulse width, bandwidth, etc.). The goal here was to determine the effectiveness of QMFB process for extracting features from AFIT's *unstructured* NTR signals which contain no intentional temporal or spectral modulation. As a first step, this was done through graphical visual assessment of energy-based graphics generated directly from various QMFB outputs—denoted here as *non-transformed* QMFB. As with previous research, the QMFB process was effective at detecting *structured* signal features. However, the QMFB process performance with *unstructured* NTR signals proved to be more challenging and motivated the need to consider *transformed* QMFB.

The initial approach for *transformed* QMFB was based on AFIT research by Gronholz and Mims (G-M), who successfully demonstrated a method for non-cooperatively detecting LPD/LPI Ultra Wideband (UWB) communication signals. The G-M process uses a multi-channel receiver containing a bank of Narrowband (NB) contiguous filters that span the UWB signal bandwidth. The filter outputs are synchronously sampled and the resulting data are used to represent the signal's Time-Frequency (T-F) response. Given common LPD/LPI characteristics of UWB and NTR signals, the resultant *G-M transformed* QMFB with NTR signals proved to be as effective as what was demonstrated with UWB signals: 1) For collected *unstructured* NTR signals, there was minimal discernible difference between NTR_{OFF} and NTR_{ON} conditions, and detection was very challenging, and 2) For synthesized *structured* NTR signals, there were distinct differences between NTR_{OFF} and NTR_{ON} conditions with detection occurring through visually-observed features that corresponded to the induced phase features. Overall, the research goal was met—the resultant *G-M transformed* QMFB is useful for both NTR development (desire to maximize LPD/LPI potential) and exploitation (desire to minimize LPD/LPI potential) research.

Table of Contents

| | Page |
|---|------|
| Abstract | iv |
| List of Figures | viii |
| List of Tables | xi |
| List of Symbols | xii |
| List of Abbreviations | xv |
| I. Introduction | 1 |
| 1.1 Research Motivation | 1 |
| 1.1.1 Operational Motivation | 1 |
| 1.1.2 Technical Motivation | 2 |
| 1.2 Research Objective and Goal | 4 |
| 1.3 Document Organization | 5 |
| II. Background | 6 |
| 2.1 AFIT's NTR-Based Noise Network (NoNET) | 6 |
| 2.1.1 NoNET NTR Implementation | 7 |
| 2.1.2 NTR Signal Detection | 9 |
| 2.1.3 LPD/LPI Signal Detection | 9 |
| 2.2 QMFB Processing | 10 |
| 2.3 Gronholz-Mims (G-M) Processing | 13 |
| III. Methodology | 17 |
| 3.1 Pre-Conditioning Operations | 18 |
| 3.2 RF Signal Collection | 20 |
| 3.2.1 RFSICS Characteristics | 21 |
| 3.3 Simulated FMCW Signal | 21 |
| 3.4 Experimental NTR Signal | 23 |
| 3.4.1 Configuration #1: Direct NTR Noise Source | 25 |
| 3.4.2 Configuration #2: Direct NTR Tx Output | 25 |
| 3.4.3 Configuration #3: Over Air Tx/Rx | 27 |
| 3.5 Post-Collection Processing | 28 |
| 3.5.1 Analysis Signal Generation | 28 |

| | Page |
|---|------|
| 3.5.2 Baseband Butterworth Filtering | 28 |
| 3.5.3 QMFB Processing | 28 |
| 3.6 Multiple Realizations | 29 |
| 3.6.1 Pre-Conditioning: <i>Non-transformed QMFB</i> . . | 29 |
| 3.6.2 Pre-Conditioning: <i>G-M Transformed QMFB</i> . | 30 |
| 3.7 Graphic Visual Assessment | 30 |
| 3.8 Wealth of Available Data | 32 |
| IV. Results | 35 |
| 4.1 FMCW Signal Processing | 36 |
| 4.2 NTR Signal Processing | 37 |
| 4.2.1 Collection and Butterworth Filtering | 40 |
| 4.2.2 QMFB Processing | 41 |
| 4.3 NTR G-M Processing | 47 |
| 4.3.1 Single NTR Realization | 47 |
| 4.4 Multiple NTR Realizations: Pre-Conditioned Q_{CTM}^{GM} . . | 50 |
| 4.4.1 Configuration #1: Direct NTR Noise Source . | 52 |
| 4.4.2 Configuration #2: Direct NTR Tx Output . . | 57 |
| 4.4.3 Configuration #3: Over Air Tx/Rx | 62 |
| 4.5 Near-Term Research Opportunities | 68 |
| 4.5.1 Spectral Scalloping | 68 |
| 4.5.2 Synthesized Bi-Phase Coding | 71 |
| V. Conclusion | 75 |
| 5.1 Research Summary | 75 |
| 5.2 Recommendation for Future Research | 77 |
| Appendix A. Additional FMCW Non-Transformed QMFB Figures . | 80 |
| Appendix B. MATLAB® Code | 85 |
| B.1 QMFB Process | 85 |
| B.2 G-M Process | 91 |
| Bibliography | 96 |

List of Figures

| Figure | | Page |
|--------|---|------|
| 2.1. | AFIT's NTR-Based NoNET Radar System | 7 |
| 2.2. | Typical NoNET Monostatic NTR Node | 7 |
| 2.3. | QMFB Process Overview | 10 |
| 2.4. | QMFB Process Graphics for FMCW Signal | 11 |
| 2.5. | G-M UWB Channelized Receiver | 14 |
| 2.6. | G-M Process Overview | 14 |
| 3.1. | Process for Assessing NTR Detectability | 18 |
| 3.2. | Spectral Response of the Simulated FMCW Signal | 22 |
| 3.3. | WB RFSCIS PSD Snapshot of the NTR Signals | 24 |
| 3.4. | NTR Configuration #1, Direct NTR Noise Source | 26 |
| 3.5. | NTR Configuration #2, Direct NTR Tx Output | 26 |
| 3.6. | NTR Configuration #3, Over Air Tx/Rx | 27 |
| 3.7. | Post-Collection Processing | 28 |
| 3.8. | Multiple Realizations for Pre-Conditioned Q_{CTM}^{GM} | 29 |
| 3.9. | G-M Process | 31 |
| 3.10. | Pre-Conditioning Operations for G-M Transformed QMFB | 32 |
| 4.1. | FMCW signal: Q_n Contour Graphics – Layer #1 to Layer #6 With $N_Q=2^{13}$ Samples | 38 |
| 4.2. | FMCW signal: Q_n Contour Graphics – Layer #7 to Layer #12 With $N_S = 2^{13}$ Samples | 39 |
| 4.3. | FMCW signal: Q_6 Contour Graphics – With $N_S = 2^{13}$ and $N_S = 2^{14}$ Samples. | 40 |
| 4.4. | NTR responses for NTR_{OFF} and NTR_{ON} Conditions | 41 |
| 4.5. | Post-Collection Butterworth Filtered NTR responses for NTR_{OFF} and NTR_{ON} Conditions | 42 |

| Figure | | Page |
|--------|--|------|
| 4.6. | <i>Non-Transformed</i> QMFB (Q_6) for NTR_{OFF} – Four Graphical Representation Using $N_Q = 2^{13}$ Samples. | 43 |
| 4.7. | <i>Non-Transformed</i> QMFB (Q_6) for NTR_{ON} – Four Graphical Representation Using $N_Q = 2^{13}$ Samples. | 44 |
| 4.8. | Pre-Conditioned Q_6 <i>Contour</i> Graphic (dB Scale) Using $N_Q = 2^{13}$ Samples for NTR_{OFF} and NTR_{ON} Conditions | 46 |
| 4.9. | Pre-Conditioned Q_6 <i>Pcolor</i> Graphic (dB Scale) Using $N_Q = 2^{13}$ Samples for NTR_{OFF} and NTR_{ON} Conditions | 46 |
| 4.10. | <i>G-M Transformed</i> Q_6 <i>Pcolor</i> Graphic using Non-Correlated TTM and SSM data with $N_Q = 2^{13}$ Samples | 48 |
| 4.11. | <i>G-M Transformed</i> Q_6 <i>Pcolor</i> Graphic using Non-Correlated CTM and CSM data with $N_Q = 2^{13}$ Samples | 49 |
| 4.12. | Pre-Conditioned Q_{CTM}^{GM} Q_6 <i>Pcolor</i> Graphics Using the Absolute <i>Real</i> Q_{TTM}^{GM} and $ Q_{TTM}^{GM} $ with $N_Q = 2^{13}$ Samples | 51 |
| 4.13. | Six Sequential Realizations of the Pre-Conditioned Q_{CTM}^{GM} <i>Pcolor</i> Graphics for NTR_{OFF} Using $N_S = 2^{13}$ Samples. | 53 |
| 4.14. | Six Sequential Realizations of the Pre-Conditioned Q_{CTM}^{GM} <i>Pcolor</i> Graphics for NTR_{ON} Using $N_S = 2^{13}$ Samples. | 54 |
| 4.15. | $N_Q = 2^{13}$ & $N_R = 3000$: Multiple Realizations of the Pre-Conditioned Q_{CTM}^{GM} Using <i>Pcolor</i> Graphics. | 55 |
| 4.16. | Config.#1, $N_Q = 2^{13}$, $N_R = 3000$, $f_c = 580$, 1618 MHz: Multi-Real. of the Pre-Conditioned Q_{CTM}^{GM} for NTR_{OFF} / NTR_{ON} | 56 |
| 4.17. | Config.#1, $N_Q = 2^{16}$, $N_R = 600$, $f_c = 580$, 1618 MHz: Multi-Real. of the Pre-Conditioned Q_{CTM}^{GM} for NTR_{OFF} / NTR_{ON} | 58 |
| 4.18. | Config.#1, $N_Q = 2^{18}$, $N_R = 210$, $f_c = 580$, 1618 MHz: Multi-Real. of the Pre-Conditioned Q_{CTM}^{GM} for NTR_{OFF} / NTR_{ON} | 59 |
| 4.19. | Config.#2, $N_Q = 2^{13}$, $N_R = 3000$, $f_c = 373$, 581, 800 MHz: Multi-Real. of the Pre-Con. Q_{CTM}^{GM} for NTR_{OFF} / NTR_{ON} | 61 |
| 4.20. | Config.#2, $N_Q = 2^{16}$, $N_R = 600$, $f_c = 373$, 581, 800 MHz: Multi-Real. of the Pre-Con. Q_{CTM}^{GM} for NTR_{OFF} / NTR_{ON} | 63 |

| Figure | | Page |
|--------|--|------|
| 4.21. | Config.#2, $N_Q = 2^{18}$, $N_R = 210$, $f_c = 373, 581, 800$ MHz: Multi-Real. of the Pre-Con. Q_{CTM}^{GM} for NTR_{OFF} / NTR_{ON} . | 64 |
| 4.22. | Config.#3, $N_Q = 2^{13}$, $N_R = 3000$, $f_c = 497, 686, 797$ MHz: Multi-Real. of the Pre-Con. Q_{CTM}^{GM} for NTR_{OFF} / NTR_{ON} . | 66 |
| 4.23. | Config.#3, $N_Q = 2^{16}$, $N_R = 600$, $f_c = 497, 686, 797$ MHz: Multi-Real. of the Pre-Con. Q_{CTM}^{GM} for NTR_{OFF} / NTR_{ON} . | 67 |
| 4.24. | Config.#3, $N_Q = 2^{18}$, $N_R = 210$, $f_c = 497, 686, 797$ MHz: Multi-Real. of the Pre-Con. Q_{CTM}^{GM} for NTR_{OFF} / NTR_{ON} . | 69 |
| 4.25. | WB RFSICS snapshot Scalping | 70 |
| 4.26. | Synthesized Bi-Phase Coded NTR: Process Block Diagram . | 71 |
| 4.27. | Synthesized Bi-Phase Coded NTR: Coding Waveform | 72 |
| 4.28. | Collected and Bi-Phase Coded NTR Signal PSDs | 72 |
| 4.29. | <i>Contour</i> Graphic for <i>non-transformed</i> QMFB Output Q_6 : Syn- thesized Bi-Phase Coded NTR Signal | 73 |
| 4.30. | <i>Pcolor</i> Graphics for <i>G-M Transformed</i> (Q_{CTM}^{GM}) QMFB Q_6 : Un- coded and Synthesized Bi-Phase Coded NTR Signals. | 73 |
| 1. | QMFB Process Graphics for FMCW Signal | 81 |
| 2. | QMFB Process Graphics for FMCW Signal | 82 |
| 3. | QMFB Process Graphics for FMCW Signal | 83 |
| 4. | QMFB Process Graphics for FMCW Signal | 84 |

List of Tables

| Table | | Page |
|-------|---|------|
| 3.1. | Simulated FMCW Signal Parameters | 22 |
| 3.2. | NTR System Components Configuration | 23 |
| 3.3. | RFSICS f_c Used for NTR Collections | 24 |
| 4.1. | Summary of Multiple NTR Realization Results | 74 |

List of Symbols

| Symbol | | Page |
|--------------|---|------|
| W_{NTR} | Bandwidth of the NTR Signal | 3 |
| W_{RF} | Bandwidth of the Collection Receiver | 4 |
| NTR_{OFF} | Background Noise Present | 4 |
| NTR_{ON} | Background Noise Plus NTR Signal Present | 4 |
| $s_T(t)$ | Transmitter Output Signal | 8 |
| $s_{Ref}(t)$ | Transmitter Reference Signal | 8 |
| $s_R(t)$ | Transmitter Reference Signal | 8 |
| $s_{Ref}[n]$ | Discrete Samples of $s_{REF}(t)$ | 8 |
| $s_R[n]$ | Discrete Samples of $s_R(t)$ | 8 |
| $S_{Ref}[k]$ | Discrete Fourier Transform of $s_{Ref}(n)$ | 9 |
| $S_R[k]$ | Discrete Fourier Transform of $s_R(n)$ | 9 |
| Q_n | QMFB Process Output for Layer n | 11 |
| Δt | QMFB Process Time Resolution | 12 |
| Δf | QMFB Process Frequency Resolution | 12 |
| N_L | Total Number of QMFB Process Layers | 12 |
| N_F | Total Number of Tiles on the Frequency Dimension | 12 |
| N_T | Total Number of Tiles on the Time Dimension | 12 |
| f_s | Sampling Frequency | 12 |
| S | Modified Sinc Scaling Variable | 12 |
| C | Modified Sinc Compression Variable | 12 |
| N | Number of Coefficients for the Modified Sinc | 12 |
| $w[n]$ | Hamming Window | 12 |
| N_Q | Number of Input Samples to the QMFB Process | 12 |
| M_G | Number Narrowband Receiver Channels | 14 |
| N_G | Number of Synchronous Time Samples for Each Channel | 14 |

| Symbol | | Page |
|--------------------|--|------|
| N_{IFFT} | Number IFFT Points | 15 |
| N_{FFT} | Number FFT Points | 15 |
| $\mathbf{Q}(j, k)$ | Arbitrary Complex Matrix at a j^{th} Row and k^{th} Column | 18 |
| N_j | Number of j rows | 18 |
| N_k | Number of k columns | 18 |
| Q_N^{GM} | G-M transformed QMFB General Case | 18 |
| Q_{TTM}^{GM} | G-M transformed QMFB Using TTM | 18 |
| Q_{CTM}^{GM} | G-M transformed QMFB Using CTM | 18 |
| Q_{SSM}^{GM} | G-M transformed QMFB Using SSM | 18 |
| Q_{CSM}^{GM} | G-M transformed QMFB Using CSM | 18 |
| $\{R(k)\}$ | RFSCIS Collected Data Sequence | 21 |
| N_S | Number of RFSICS I&Q Collected Samples | 21 |
| f_c | Center Frequency | 21 |
| W_{IF} | Bandwidth of the Intermediate Frequency | 21 |
| b | Bits | 21 |
| W_{BP}^{Noise} | Bandwidth of the Noise | 21 |
| f_c^{Noise} | Noise Center Frequency | 21 |
| W_{BP}^{FM} | Bandwidth of the FM | 21 |
| T_M | FM Period | 21 |
| f_c^{FM} | FM Center Frequency | 21 |
| W_{BP}^{FMCW} | Bandwidth of the FMCW | 22 |
| f_c^{FMCW} | FMCW Center Frequency | 22 |
| T_T | FMCW Waveform Period | 22 |
| P_N | Noise Power | 22 |
| $W_{config\#1}$ | Bandwidth of Configuration#1 | 25 |
| $W_{config\#2}$ | Bandwidth of Configuration#2 | 26 |
| $W_{config\#3}$ | Bandwidth of Configuration#3 | 27 |

| Symbol | | Page |
|-----------------|---|------|
| T_c | RFSICS Collection Time Period | 28 |
| W_{BB} | Baseband Bandwidth | 28 |
| N_R | Number of Realizations | 29 |
| N_{CC} | Number of Collection Configurations | 32 |
| N_{SB} | Number of NB Sub-Band collections | 32 |
| N_{CL} | Number of Chosen Layer(s) | 33 |
| N_{GM} | Number of G-M transformations | 33 |
| N_G^Q | Number of QMFB Graphics | 33 |
| N_G^{preQ} | Number of Pre-Conditioned QMFB Graphics | 33 |
| N_G^{GM} | Number of G-M Graphics | 33 |
| $N_G^{pre\ GM}$ | Number of Pre-Conditioned G-M Graphics | 33 |

List of Abbreviations

| Abbreviation | | Page |
|---------------|---|------|
| NTR | Noise Technology Radar | 1 |
| DSP | Digital Signal Processing | 1 |
| FFT | Fast Fourier Transform | 1 |
| SAR | Synthetic Aperture Radar | 2 |
| RF | Radio Frequency | 2 |
| RFINT | Radio Frequency Intelligence | 2 |
| AFIT | Air Force Institute of Technology | 2 |
| NoNET | Noise Network | 2 |
| CW | Continuous Wave | 3 |
| LPI | Low Probability of Intercept | 3 |
| LPD | Low Probability of Detection | 3 |
| EW | Electronic Warfare | 3 |
| QMFB | Quadrature Mirror Filter Banks | 3 |
| T-F | Time-Frequency | 3 |
| FMCW | Frequency Modulated Continuous Wave | 3 |
| BPSK | Binary Phase Shift Keyed | 3 |
| UWB | Ultra Wideband | 3 |
| NB | Narrowband | 3 |
| G-M | Gronholz-Mims | 4 |
| SOI | Signal of Interest | 4 |
| PSD | Power Spectral Density | 8 |
| <i>Tx Out</i> | Transmitter Output Signal | 8 |
| <i>Tx Ref</i> | Transmitter Reference Signal | 8 |
| <i>Rx In</i> | Transmitter Reference Signal | 8 |
| DFT | Discrete Fourier Transform | 9 |

| Abbreviation | | Page |
|--------------|--|------|
| IDFT | Inverse Discrete Fourier Transform | 9 |
| RSR | Random Signal Radar | 9 |
| RNR | Random Noise Radar | 9 |
| I&Q | In-Phase and Quadrature-Phase | 10 |
| QMF | Quadrature Mirror Filter | 10 |
| FIR | Finite Impulse Response | 12 |
| TTM | Temporal-Temporal Matrix | 13 |
| CTM | Cross-Temporal Matrix | 13 |
| SSM | Spectral-Spectral Matrix | 13 |
| CSM | Cross-Spectral Matrix | 13 |
| CDM | Channelized Data Matrix | 13 |
| RFSICS | Radio Frequency System Intercept and Collection System | 17 |
| ADC | Analog-to-Digital Converter | 20 |
| IF | Intermediate Frequency | 21 |
| AWGN | Additive White Gaussian Noise | 21 |
| n/a | Not Applicable | 23 |

CHARACTERIZATION OF NOISE TECHNOLOGY RADAR (NTR) SIGNAL DETECTABILITY USING A NON-COOPERATIVE RECEIVER

I. Introduction

This chapter introduces the research motivation, objective and goal, and document organization. The research motivation is provided in two subsections, with one providing the Operational Motivation and the other providing Technical Motivation. The operational motivation provides the big picture concept and the technical motivation identifies key concepts that served as the research foundation. This foundation was used to formalize the research objective and achieve the goal of advancing the capability to non-cooperatively detect and characterize Noise Technology Radar (NTR) signals. This chapter concludes with an overview of the document's organization.

1.1 Research Motivation

1.1.1 Operational Motivation. The concept of noise radar was first introduced circa 1950 [12, 18] with its initial implementability primarily limited by the computational intensity required for correlation using analog circuits [13]. Subsequent advances in computers, technology, and software have revived NTR development to the point where NTR research is proliferating throughout the world. In particular, advances in Digital Signal Processing (DSP) have greatly reduced the required computational complexity for correlating signals using a discrete Fast Fourier Transform (FFT). At the same time, the DSP improvements enable implementation of more computationally-efficient algorithms and performance optimization. There are two distinct veins of ongoing NTR research, including: 1) NTR *developmental* work aimed at improving NTR performance from a *cooperative* radar detection

perspective [3–5, 10, 13, 17, 18, 25, 30–32] and 2) NTR *exploitation* work aimed at assessing NTR exploitability using *non-cooperative*, “non-matched filter” detection methods [11, 27].

NTR research is currently underway in various countries, including: the United States, Ukraine, Poland, United Kingdom, Canada, Austria, Montenegro, France, Germany, Italy, Russia, Sweden, Norway, China, South Korea, and India [5, 10, 13, 17, 18, 25, 30–32]. A couple specific examples of global research abroad include: 1) Swedish researchers seeking to improve NTR system performance using beam-forming, waveform coding for Doppler enhancement, and Synthetic Aperture Radar (SAR) [2–4] imaging; and 2) Polish researchers working to improving NTR system performance using impulse-based sources [14]. In essence, NTR research is being conducted worldwide and spans a vast range of applications from SAR imaging to collision avoidance [2, 18, 19].

The near-worldwide interest in NTR system development and its likely deployment in the not-too-distant future have gotten the attention of researchers in the Radio Frequency (RF) Intelligence (RFINT) community. As with all new technology deployments, the RFINT community is always looking forward to ensure that their arsenal of RF awareness tools remains up-to-date. This includes the capability to non-cooperatively exploit identify information from emerging signals of interest.

1.1.2 Technical Motivation. NTR research remains an ongoing area of interest at the Air Force Institute of Technology (AFIT). Specifically, AFIT’s NTR technology is being developed to support the Noise Network (NoNET). AFIT’s NoNET radar system is an integrated group of NTR nodes with centralized processing for data acquisition, digital processing, and multi-sensor image fusion. Of the two research veins noted earlier, NTR *developmental* work has been the primary focus at AFIT [16, 25, 28, 30]. This is due to the low power, random structure of the NTR signal which result in electromagnetic properties that cause minimum RF inter-

ference and allow the NTR system to share frequency bands with other devices [13]. Furthermore, the Continuous Wave (CW) NTR implementation being used by AFIT provides range resolution that is on par with conventional CW radar.

The emerging NTR signals inherently fall into the class of Low Probability of Intercept (LPI) signals given that they are relatively low power, wide bandwidth, and have frequency variability that make non-cooperative detection very challenging [11,27]. Under less stricter definitions, they are also Low Probability of Detection (LPD) signals given that their “presence” is difficult to determine using conventional power-based detectors such as radiometers [8,21]. Thus, the LPD/LPI characteristics of NTR signals being developed at AFIT provide good Electronic Warfare (EW) counter-countermeasure capability [13]. This is what motivated the need for the second vein of NTR *exploitation* research as conducted under this research.

The LPD/LPI research in [11,27] provides the foundation for the research conducted. Most importantly, these previous works identified the Quadrature Mirror Filter Bank (QMFB) process as a viable approach for extracting LPD/LPI signal features. The QMFB process decomposes the LPD/LPI signal using orthogonal wavelets [6,11] and has been used as a form of spread spectrum intercept receiver [6]. By considering the QMFB output Time-Frequency (T-F) data for a given layer, graphic representations can be used to provide relatively good estimates of parameters used to generate *structured* signals, i.e., modulation type, bandwidth, center frequency, phase modulation, signal duration, etc. [27]. It is important to note that the LPD/LPI detection work in [11,27] was based on *structured* signals containing distinct modulation features, i.e., Frequency Modulated CW (FMCW) and Binary Phase Shift Keyed (BPSK) signals. Furthermore, the instantaneous bandwidth of the non-cooperative receiver spanned the entire bandwidth of the FMCW and BPSK signals. This differs considerably from the research conducted here which is based on *unstructured* Ultra Wideband (UWB) NTR signals that are collected using a Narrowband (NB) collection receiver, i.e., the bandwidth of the NTR signal (W_{NTR}) is

greater than the collection receiver bandwidth (W_{RF}) such that only a fraction of the NTR signal's spectral response is used for any given assessment ($W_{RF} \approx W_{NTR}/10$).

Detection and estimation of *unstructured* signals such as those used for NTR is very challenging. Thus, more robust detection and estimation methods were sought under this research using QMFB outputs and transformation methods investigated previously by Grohholz-Mims (G-M) for UWB communication signals [7, 8, 22, 23]. The G-M process is a non-cooperative multi-channel detection method that was demonstrated using a bank of NB contiguously-spaced filters that spanned the UWB communication signal bandwidth. Given the characteristic similarity between the UWB communication signal and the UWB NTR signal considered under this research, the incorporation of the G-M process was a reasonable next step for non-cooperative NTR signal detection. As demonstrated, the G-M process exploits inherent temporal and spectral differences using four detection methods. Each of these four methods were assessed for the NTR signal of interest, (SOI).

1.2 Research Objective and Goal

The overall research objective was to collect, detect, and assess NTR signal characteristics using qualitative graphical visualization. This objective was formalized relative to the two veins of research being supported, including development (desire to maximize LPD/LPI potential) and exploitation (desire to minimize LPD/LPI potential). The goal was to improve upon existing QMFB signal processing and graphical visualization methods to enable non-cooperative detection of NTR signals. The resultant analysis graphics are similar to what was envisioned for an input to a human interface device to enable an operator to detect NTR signals (declare NTR presence). The detection approach used a non-cooperative collection receiver and empirical pair-wise assessment of graphics obtained for NTR_{OFF} and NTR_{ON} collection conditions. The emergence of distinguishable feature characteristics and/or differences between the two conditions constituted NTR signal detection.

1.3 Document Organization

This document includes five chapters and three appendices. This section outlines what is provided in each chapter. Chapter II provides relevant technical background information on three major concepts used to support the research, including 1) AFIT's NTR-Based NoNET, 2) QMFB processing, and 3) G-M processing.

Chapter III provides the overall approach, process, and techniques used to visually assess and characterize the NTR signal. A detailed description of the collection process and NTR configurations is first presented. This is followed by descriptions of various post-collection processes that were implemented in MATLAB®.

Chapter IV provides qualitative graphical results and assessments using the process outlined in Chapter III. Verification of the QMFB process is first provided, followed by the step-by-step application of processes outlined in Chapter III with key down-selection details highlighted where appropriate. Finally, the overall results are presented for selected scenarios; the amount of available graphical data is quite immense and only a fraction of it is presented to ensure that a succinct textual presentation is made on NTR detectability.

Chapter V concludes the thesis and provides an overall summary of the research motivation, goals, techniques, results, and follow-on recommendations. This section is followed by three appendices that provide supplementary graphical results and the MATLAB® code to implement select post-collection processes.

II. Background

This chapter presents relevant technical background information on three major concepts and techniques used to conduct this research, including: 1) AFIT's NTR-Based Noise Network (NoNET), 2) Quadrature Mirror Filter Bank (QMFB) processing, and 3) Gronholz-Mims (G-M) processing. As described in Section 2.1, the primary Signal of Interest (SOI) is the Noise Technology Radar (NTR) signal being developed for use in AFIT's NoNET. The non-cooperative, "non-matched filter" detection, estimation, and exploitation of NTR signal features are addressed using the QMFB process described in Section 2.2. Improvement in NTR detectability through graphical visual assessment is addressed using the G-M process in Section 2.3. For both non-transformed QMFB and G-M transformed QMFB processes, NTR signal detectability is assessed using comparative analysis of graphics generated under NTR_{OFF} and NTR_{ON} conditions.

2.1 AFIT's NTR-Based Noise Network (NoNET)

The NTR signals considered for this research were generated using one of the NTR systems (nodes) in AFIT's Noise Network (NoNET) operating a monostatic configuration in Figure 2.1. The NoNET was first established at AFIT in 2009 [30] and is based on the developmental work by Dr. Narayanan at Pennsylvania State University [24]. Since that time, work has continued at AFIT to improve NoNET monostatic and multistatic radar performance [25]. Currently, there are two distinct veins of research involving NoNET research, including 1) NTR developmental work to improve NoNET performance from a radar perspective [16, 28] and 2) NTR exploitation work to assess NoNET exploitability—the focus of this research. The NTR development component aims to improve cooperative transmit-reflect-receive signal detectability while the exploitation component aims to improve the non-cooperative detectability of transmit-only NTR signals.

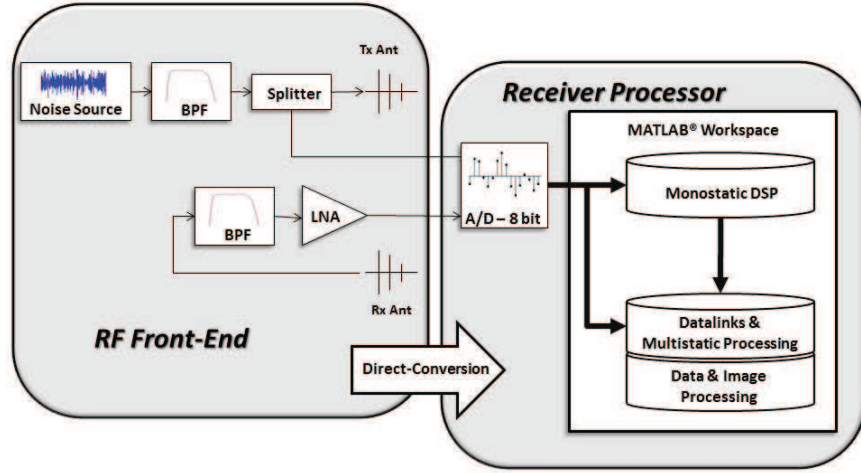


Figure 2.1: Functional diagram of AFIT's NTR-Based Noise Network (NoNET) radar system [28]

2.1.1 NoNET NTR Implementation. As detailed in Figure 2.2 and used for this research, each NoNET node can be operated as an independent monostatic NTR. The basic NTR system is comprised of three main components, including a: 1) Transmitter, 2) Receiver and 3) Receiver Processor. A majority of the NTR system complexity resides in the receiver processor, which is where correlation is used to detect target responses.

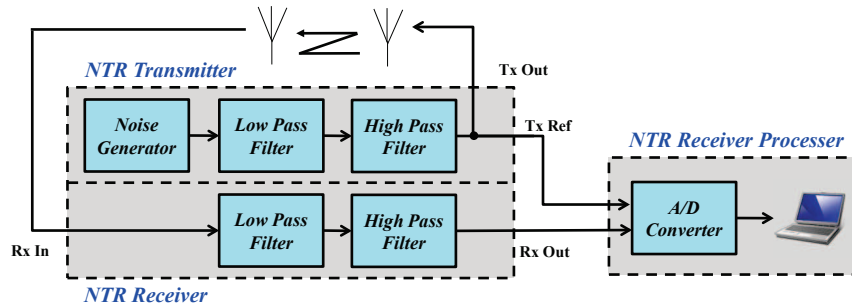


Figure 2.2: Implementation diagram of typical monostatic NTR node in AFIT's NoNET radar system.

As currently configured, the NTR operates as a CW radar that ideally transmits a purely random signal produced by a solid-state thermal noise source. The

thermal noise response can be characterized as bandlimited white Gaussian noise given that its Power Spectral Density (PSD) is nearly uniform over a finite bandwidth [25, 26]. The noise source output is effectively bandpass-filtered using a series of low-pass and high-pass filters. The resultant NTR transmit bandwidth is $W_{NTR} \approx 400$ MHz [30]. The filtered signal is power-divided to create the transmitter output signal (*Tx Out*), $s_T(t)$, which is fed to a high gain log-periodic antenna for over-the-air transmission. The other output is fed to the receiver processor and serves as the transmitter reference (*Tx Ref*), $s_{Ref}(t)$. The *Tx Out* signal propagates through the channel, reflects off a target(s), and is received by another high gain log-periodic antenna. The received input signal (*Rx In*), $s_R(t)$, is filtered to extract desired frequency components and passed to the receiver processor for digital correlation with a stored copy of $s_{Ref}(t)$ [25, 30].

The correlation process in the NTR receiver processor effectively distinguishes the target return signal (NTR noise signal) from undesired random noise responses induced by the channel and present in the received signal. Given that the transmitted signal response is known, $s_{Ref}(t) = s_T(t)$ and cross-correlation can be used to determine the target presence in the return signal. This is implemented using

$$C_{Ref,R}(\tau) = \int_0^T s_{Ref}(t)s_R(t + \tau)dt, \quad (2.1)$$

where T is the time duration of the recorded transmitted signal at each frequency and t is the time delay. The function in (2.1) provides a measure of “likeness” between the signals being correlated. When $s_{Ref}(t)$ is present in $s_R(t)$, the system produces a high cross-correlation value and a “thumbtack” like graphical response which is referred to as auto-correlation. At sufficiently high SNR, this peak response rises above the noise-only response and the presence of an NTR signal is detected.

The correlation in (2.1) is functionally implemented digitally for computational efficiency. The notations $s_{Ref}[n]$ and $s_R[n]$ are introduced here to represent sampled

versions of $s_{Ref}(t)$ and $s_R(t)$, respectively. Specifically, the digital implementation includes 1) converting $s_{Ref}[n]$ and $s_R[n]$ to the spectral domain using a discrete Fourier Transform (DFT), 2) multiplying the resultant Fourier components, and 3) taking the inverse discrete Fourier Transform (IDFT) returns the resultant to the sampled time domain. DFT and IDFT are computed using FFT. This is analytically expressed as

$$C_{Ref,R}[n] = IDFT \{S_{Ref}(k)S_R^*(k)\} , \quad (2.2)$$

where $S_{Ref}[k]$ and $S_R[k]$ the DFT of $s_{Ref}[n]$ and $s_R[n]$, and $*$ is the complex conjugate. With a known transmitted signal and correlation, the NTR system is a very robust and effective process to detect a returned target signal.

2.1.2 NTR Signal Detection. There are various terminologies used throughout the NTR community that refer to specific implementations of NTR systems, two of which include Random Signal Radar (RSR) and Random Noise Radar (RNR) [9, 11, 15]. RNR refers to a system using a *non-modulated* unstructured noise signal [11, 15] while RSR refers to a system using a *modulated* structured random noise signal [9, 11]. Collectively considering all of these related works, NTR developmental research appears to be a global activity. When considering the non-cooperative exploitation of NTR the work appears to be limited to a few researchers [11, 27]. These non-cooperative activities generally classify NTR signals as being Low Probability of Detection (LPD) and Low Probability of Intercept (LPI)–complex signals that are difficult to detect and which possess covert characteristics.

2.1.3 LPD/LPI Signal Detection. The work in [11, 27] considered four different detection methods for LPD/LPI signals, including: Wigner-Ville, Choi-Williams, QMFB, and cyclostationary processes [27]. Based on this earlier research, QMFB process emerged as the technique that provided the most potential for reveal-

ing signal features in “structured” signals, i.e., signals containing distinct features in a given signal domain(s) (time, frequency, etc.). The QMFB process decomposes the LPD/LPI signal using orthogonal wavelets [6, 11] and has been used as a form of spread spectrum intercept receiver [6]. By considering the QMFB output Time-Frequency (T-F) data for a given QMFB layer, graphic visualization can be used to provide relatively good estimates of the structured signal parameters, i.e., modulation type, bandwidth, center frequency, phase coding, and signal duration [27]. The previous research in [11, 27] was limited to considering structured signals, i.e. FMCW and BPSK signals.

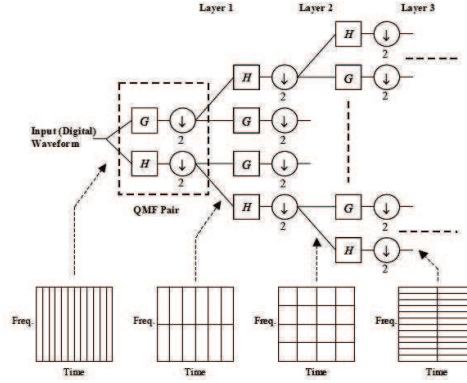


Figure 2.3: QMFB process overview [11, 27].

2.2 QMFB Processing

The QMFB process sequentially “breaks down” the in-phase and quadrature-phase (I&Q) components of the input signal using modified sinc-shaped filters in a series of Quadrature Mirror Filter (QMF) pairs and layers as illustrated in Figure 2.3. The output of each layer is T-F data for each QMF pair, with the amount of QMF pairs increasing by a power of two with each increasing layer number. As illustrated in the bottom of Figure 2.3, the QMFB layer outputs can be represented as rectangular T-F “tiles” with the tile dimensions (T-F resolution) varying as a function of layer number. For this research, the QMFB process output for layer n is

denoted by Q_n and referred to as the *non-transformed* QMFB response. Representative graphics for a QMFB processed FMCW waveform are provided in Figure 2.4 for illustration. These particular graphics are based on Layer #6 output data (Q_6) and were generated using MATLAB[®] graphic functions—*contour*, *mesh*, *surface* and *Pseudo-Color* (denoted henceforth as *Pcolor*).

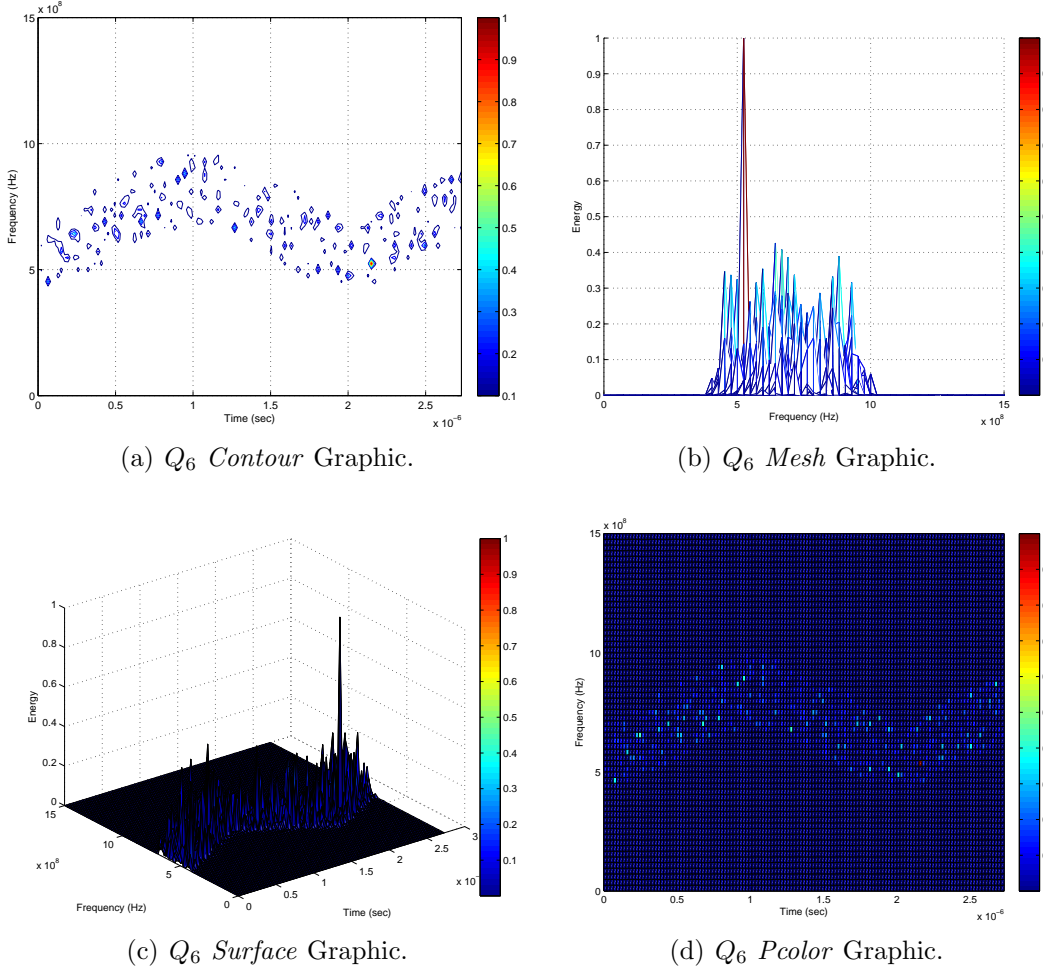


Figure 2.4: Four graphical representation (as indicated) of the *Non-Transformed* QMFB (Q_6) for Layer #6 NTR_{ON} condition using $N_Q = 2^{13}$ samples.

With each increase in layer number, there is a corresponding trade-off in T-F resolution [27], i.e., frequency resolution increases along the frequency dimension (F) as the signal is decomposed (filtered) at each stage into low and high frequency com-

ponents. Correspondingly, the time resolution decreases along the time dimension (T) given the inversely proportional T-F relationship [6]. The time resolution (Δt) and frequency resolution (Δf) are given by [27]

$$\Delta f = \frac{f_s}{2(2^{N_L-1} - 1)} = \frac{f_s}{N_F} , \quad (2.3)$$

$$\Delta t = \frac{2^{N_L}}{f_s(2^{N_L-1} - 1)} = \frac{2^{N_L}}{f_s N_T} , \quad (2.4)$$

where N_L is the total number of QMFB layers, N_F is the number of tiles along the frequency dimension, N_T is the number of tiles along the time dimension, and f_s is the sampling frequency. Consistent with the T-F inverse proportional relationship, lower numbered layers have higher time resolution and lower frequency resolution when compared to higher numbered layers which have reduced time resolution and higher frequency resolution.

The frequency decimation in the QMFB process is implemented here using a “modified sinc” Finite Impulse Response (FIR) filters having a response given by [6]

$$h[n] = \sqrt{\frac{S}{2}} \operatorname{sinc}\left(\frac{n + 0.5}{C}\right) w[n] , \quad -\frac{N}{2} \leq n \leq \frac{(N-2)}{2} , \quad (2.5)$$

where S is the scaling variable, C is the compression variable, N is the number of coefficients, and $w[n]$ is a Hamming window weighting. The Hamming window is used to suppress the effects of Gibb’s phenomena resulting from truncation of n [6]. These particular filters have a flat pass region and produce the maximum amount of desired signal energy within each tile while rejecting other unwanted responses. Based on research in [6], the ideal filter coefficients for $N = 512$ are $C = 1.99375872338059$ and $S = 1.00618488680080$ which provide a set of “nearly orthogonal filters with cross-correlation of less than .001” [6, 11, 27].

There are some special conditions to consider when implementing QMFB process. For example, the number of input samples to the QMFB process (N_Q) must

satisfy $N_Q = 2^n$ for n a positive integer. This produces N_L QMFB layers:

$$N_L = \log_2 (N_Q) . \quad (2.6)$$

For a collected signal sample size of $N_S \neq 2^n$, the collected signal can either be parsed to a power-of-two producing N_L layers per (2.7) or zero-padded and extended to a power-of-two to produce N_L layers per (2.8).

$$N_L = \text{floor}[\log_2(N_S)] . \quad (2.7)$$

$$N_L = \text{ceil}[\log_2(N_S)] . \quad (2.8)$$

The resultant matrices (Q_n) from QMFB process may be used for signal detection (establishing presence) and/or assessment of signal features as captured in the Q_n T-F data. Generally, Q_n matrices contain different information that can be visualized through various graphical representations. The amount of information revealed is a function of the layer number, n , and the specific graphic used to visualize the transformed data (surface, contour, etc.)

2.3 Gronholz-Mims (G-M) Processing

As adopted here, the Gronholz-Mims (G-M) process was developed in [7, 8, 22, 23] to enable Narrowband (NB) processing and exploitation of Ultra Wideband (UWB) Communication Signals. The main goal in the G-M process is to exploit potential temporal and spectral differences in NB signal responses by transforming T-F data to produce four alternate data matrices, including: Temporal-Temporal Matrix (TTM), Cross-Temporal Matrix (CTM), Spectral-Spectral Matrix (SSM), and the Cross-Spectral matrix (CSM). The G-M process is depicted in Figure 2.6 which shows the complex Channelized Data Matrix (CDM) as the input.

For previous G-M demonstrations in [7, 8, 22, 23] the input CDM was generated using the channelized receiver architecture illustrated in Figure 2.5. In this case, the CDM effectively represents the $M_G \times N_G$ T-F response of the input signal, where $r(t)$ is the UWB communication signal, M_G is the number NB receiver channels, N_G is the number of synchronous time samples taken for each channel, and H_{RF} is the input UWB communication signal bandwidth. The receiver is a bank of equal bandwidth, NB bandpass filters with different center frequencies that collectively span the full bandwidth of the UWB input signal. For general application, the G-M process in Figure 2.6 can be applied using any input matrix representing T-F data. The process flow for G-M transformation per Figure 2.6 is described in the next paragraph.

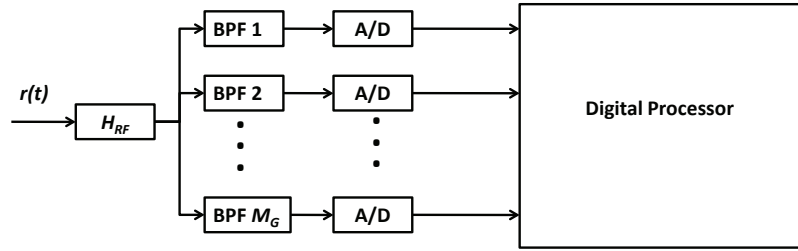


Figure 2.5: G-M UWB Channelized Receiver [7, 8, 22, 23].

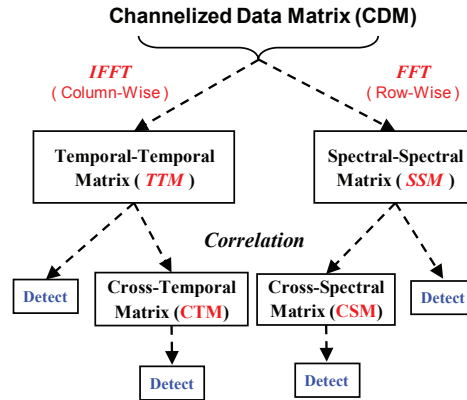


Figure 2.6: Gronholz-Mims (G-M) process overview [7, 8, 22, 23].

In order to generate the TTM and corresponding CTM matrices, the input CDM is first transformed using an N_{IFFT} -point IFFT on a column-by-column basis (*column-wise*) to produce the TTM. If $N_{IFFT} > M_G$ zero-padding can be used and if $N_{IFFT} < M_G$, the higher frequency elements may be neglected. The corresponding column-wise and row-wise CTM is easily generated using [7, 8, 22, 23]

$$CTM_{Col} = \frac{1}{N_{IFFT}} \left| TTM^H \cdot TTM \right|, \quad (2.9)$$

or

$$CTM_{Row} = \frac{1}{N_{IFFT}} \left| TTM \cdot TTM^H \right|, \quad (2.10)$$

where the superscripted H denotes the Hermitian, or conjugate transpose operation. Also, the CTM can be created using the rows of TTM.

The SSM and corresponding CSM matrices are generated using a similar process, with the input CDM is first transformed using an N_{FFT} -point FFT on a row-by-row basis (*row-wise*) to produce the SSM. If $N_{FFT} > N_G$ zero-padding may be used and if $N_{FFT} < N_G$, the higher time elements may be neglected. The corresponding column-wise and row-wise CSM is easily generated using [7, 8, 22, 23]

$$CTM_{Col} = \frac{1}{N_{FFT}} \left| SSM^H \cdot SSM \right|, \quad (2.11)$$

or

$$CSM_{Row} = \frac{1}{N_{FFT}} \left| SSM \cdot SSM^H \right|. \quad (2.12)$$

The resultant matrices from (2.9) through (2.12) may be used for signal detection (establishing presence) and/or assessment of signal features as captured in the input CDM T-F data. Generally, the four resultant G-M matrices contain different information that can be visualized through graphical representation using *Pcolor* graphic function in MATLAB®. The amount of information revealed is a function of

where the information exists (temporal domain, spectral domain, or cross-correlation thereof).

Summary

This chapter presented the relevant background information on key technical concepts required to conduct this research. This included a summary of 1) AFIT's NTR-Based Noise Network (NoNET), 2) Quadrature Mirror Filter Bank (QMFB) Processing, and the 3) Gronholz-Mims (G-M) Processing. Sufficient references are provided in respective sections if more detailed information is required.

III. Methodology

This chapter provides the research methodology used for assessing NTR signal detectability by applying the process illustrated in Figure 3.1. This process was used to support the technical contribution of this research in two aspects:

1. This research represents the first known assessment of NTR detectability using the (Quadrature Mirror Filter Bank) QMFB process and the *Previous* graphics that are commonly used [27]. Thus, the *Previous* label in Figure 3.1 simply indicates that the graphic visualization is the same as used previously with structured signals. The importance of applying the end-to-end process in Figure 3.1 with NTR signals, i.e., from NTR signal collection through post-collection processing and visualization with *Previous* graphics should not be overlooked.
2. The dashed-box with the *Current* label in Figure 3.1 represents implementation of multi-channel processing and graphic visualization used previously by Gronholz [7, 8] and Mims [22, 23] to qualitatively assess the detectability of Ultra Wideband (UWB) communication signals. Of direct relevance to this research, these previous methods are based on (Narrowband) NB assessment of UWB signals—the approach adopted here for NTR signals. To identify the application of these previous methods with results generated here, the (G-M) notation is introduced here and used henceforth in the document.

This chapter includes six major subsections: 1) Pre-Conditioning Operations, 2) RF Signal Collection, 3) Simulated FMCW Signal, 4) Experimental NTR Signal, 5) Post-Collection Processing, 6) Graphic Visualization, and 6) Wealth of Available Data. Section 3.2 provides an understanding of the collection system, Radio Frequency System Intercept and Collection System (RFSICS). Next, Section 3.3 and Section 3.4 describe the SOI FMCW and NTR with detailed descriptions of the

three NTR configurations. Section 3.5 goes into the main research area covering the post-collection and post-QMFB processing, minus the graphic visualizations which are covered in the next section.

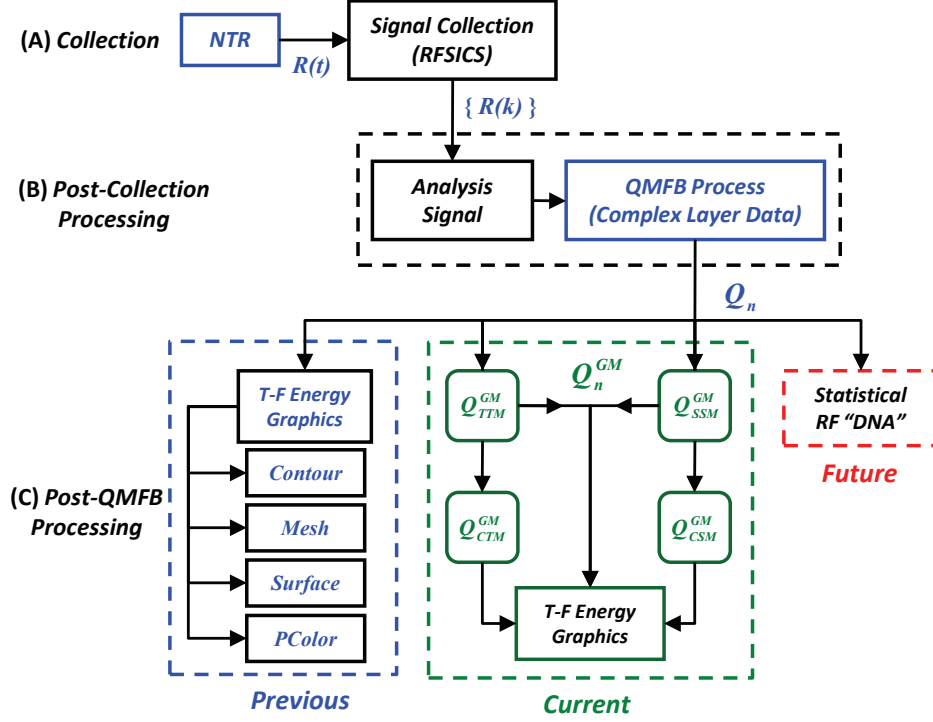


Figure 3.1: Overview of process used to assessing NTR detectability.

3.1 Pre-Conditioning Operations

This section provides details of pre-conditioning operations that were applied to various complex data matrices throughout the overall process detailed in Figure 3.1. The operations are presented in no particular order using the notation $Q(j, k)$ to represent the j^{th} row and k^{th} column of an *arbitrary* Complex Matrix having N_j rows and N_k columns. As ultimately used for the research and detailed in Section 3.6.1 and Section 3.6.2, the pre-conditioning operations can be applied in any order to:

1. Any of the complex matrices shown in Figure 3.1, including the direct QMFB output Q_n and the G-M transformed Q_N^{GM} : Q_{TTM}^{GM} , Q_{CTM}^{GM} , Q_{SSM}^{GM} , Q_{CSM}^{GM} .

2. Any resultant output matrix from previous pre-conditioning operations, i.e., the operations can be sequentially applied. For example, the input matrix $Real[\mathbf{Q}]$ may be first row-wise magnitude normalized using (3.3), followed by row-wise cross-correlated using (3.10), and converted to dB using (3.1) before graphics are generated.

The available pre-conditioning operations include:

1. Available Inputs: $\mathbf{Q}(\mathbb{C})$, $Real[\mathbf{Q}](\mathbb{R})$, $Imag[\mathbf{Q}](\mathbb{I})$, and $|\mathbf{Q}|$ (Magnitude).
2. Converting to Energy in dB:

$$E_{dB}^Q = 10 \log_{10} (|\mathbf{Q}|^2) \quad (3.1)$$

3. Global *Maximum Magnitude* Normalization:

$$\bar{\mathbf{Q}}(j, k) = \mathbf{Q}(j, k) / \max [|\mathbf{Q}|] \quad \forall j, k \quad (3.2)$$

4. Row-Wise and Column-Wise *Maximum Magnitude* Normalization:

$$\bar{\mathbf{Q}}(j, :) = \mathbf{Q}(j, :) / \max [|\mathbf{Q}(j, :)|] \quad \forall j \quad (3.3)$$

$$\bar{\mathbf{Q}}(:, k) = \mathbf{Q}(:, k) / \max [|\mathbf{Q}(:, k)|] \quad \forall k \quad (3.4)$$

5. Row-Wise and Column-Wise *Power* Normalization:

$$P_Q(j) \approx \frac{1}{N_k} \sum_{k=1}^{N_k} \mathbf{Q}(j, k)^2, \quad \forall j \quad (3.5)$$

$$\bar{\mathbf{Q}}(j, k) = \frac{1}{\sqrt{P_Q(j)}} \times \mathbf{Q}(j, k), \quad \forall j, k$$

$$P_Q(k) \approx \frac{1}{N_j} \sum_{j=1}^{N_j} \mathbf{Q}(j, k)^2, \quad \forall k \quad (3.6)$$

$$\bar{\mathbf{Q}}(j, k) = \frac{1}{\sqrt{P_Q(k)}} \times \mathbf{Q}(j, k), \quad \forall j, k$$

6. Row-Wise and Column-Wise *Amplitude* Normalization:

$$A_Q(j) = \max [|\mathbf{Q}(j, :)|], \quad \forall j \quad (3.7)$$

$$\bar{\mathbf{Q}}(j, k) = \mathbf{Q}(j, k) / A_Q(j), \quad \forall j, k$$

$$\begin{aligned}
A_Q(k) &= \max [|\mathbf{Q}(:, k)|] , \forall k \\
\bar{\mathbf{Q}}(j, k) &= \mathbf{Q}(j, k)/A_Q(k) , \forall j, k
\end{aligned} \tag{3.8}$$

7. Thresholding/Flooring:

$$\begin{aligned}
\textit{Calculate} : t_Q &= \min [\mathbf{Q}] \\
\textit{Initialize} : \mathbf{Q}^F(j, k) &= \mathbf{Q}(j, k) , \forall j, k \\
\textit{Floor} : \mathbf{Q}^F(j, k) < t_Q &\implies \mathbf{Q}^F(j, k) = t_Q , \forall j, k
\end{aligned} \tag{3.9}$$

8. Thresholding/Flooring, Pair-Wise Associated NTR_{OFF} and NTR_{ON} :

$$\begin{aligned}
\textit{Calculate} : t_Q &= \max \{ \min [\mathbf{Q}_{OFF}], \min [\mathbf{Q}_{ON}] \} \\
\textit{Initialize} : \mathbf{Q}_{OFF}^F(j, k) &= \mathbf{Q}_{OFF}(j, k) , \forall j, k \\
\textit{Initialize} : \mathbf{Q}_{ON}^F(j, k) &= \mathbf{Q}_{ON}(j, k) , \forall j, k \\
\textit{Floor} : \mathbf{Q}_{OFF}^F(j, k) < t_Q &\implies \mathbf{Q}_{OFF}^F(j, k) = t_Q , \forall j, k \\
\textit{Floor} : \mathbf{Q}_{ON}^F(j, k) < t_Q &\implies \mathbf{Q}_{ON}^F(j, k) = t_Q , \forall j, k
\end{aligned} \tag{3.10}$$

9. Row-Wise and Column-Wise Cross-Correlation [7, 8]:

$$\begin{aligned}
\mathbf{Q}_C^{Row} &= \frac{1}{N_k} (\mathbf{Q} \cdot \mathbf{Q}^H) \\
\mathbf{Q}_C^{Col} &= \frac{1}{N_j} (\mathbf{Q}^H \cdot \mathbf{Q})
\end{aligned} \tag{3.11}$$

where superscripted H denotes Hermitian or conjugate-transpose, N_j is the number of rows and IFFT operations, and N_k is the number of columns and FFT operations.

3.2 RF Signal Collection

The RFSICS is used to collect NTR signals using the procedures detailed in Appendix A of [29]. A description of key RFSICS characteristics is provided in Section 3.2.1. The RFSICS was used for the three NTR collection configurations detailed in Section 3.4.1, Section 3.4.2, and Section 3.4.3. For all configurations the RFSICS was first set up to collect with the NTR_{ON} condition to enable setting of the Analog-to-Digital converter (ADC) dynamic range to avoid clipping the

collected signals. The NTR system was then switched off and collected signals for the NTR_{OFF} condition. Thus, for all comparative NTR_{OFF}/NTR_{ON} assessment, the variability due to collection system bias is minimal given that the RFSICS settings were identical for the pair of NTR_{OFF} and NTR_{ON} signals being assessed. Comparing the collection conditions is a start to determine if the NTR systems is detectable and reveal any information that is inherent to the transmitter. Following collection, the signal was converted from the Agilent® proprietary “capture” file (*.cap) to standard MATLAB® (*.mat) format for post-collection processing [29]. The resultant collected data sequence, denoted as $\{R(k)\}$, contains (N_S) collected complex I&Q samples.

3.2.1 RFSICS Characteristics. The RFSICS is an Agilent®-based receiver system that AFIT uses for RF signal collection and experimentation [1]. The RFSICS has a Narrowband (NB) instantaneous collection bandwidth (W_{RF}) of $W_{RF} = 36$ MHz. This is coupled with Wideband (WB) search capability across the range of $f_c \in [0.02, 6.00]$ GHz [29]. The WB search is sometimes rendered as WB RFSICS snapshots by displaying a compilation of $W_{RF} = 36$ MHz sweeps. Within the RFSICS, the collected signal is down-converted to an intermediate frequency (IF) of $W_{IF} = 70$ MHz and sampled at $f_s = 47.5$ Msps using a $b = 12$ -bit analog-to-digital converter [29]. Finally the signal is converted to baseband.

3.3 Simulated FMCW Signal

Generation of the simulated FMCW signal was based on the model in [27]. First, the noise was created using an Additive White Gaussian Noise (AWGN) model with a sample frequency $f_s = 3.0$ GHz. The generated noise was bandpass-filtered using a bandwidth of $W_{BP}^{Noise} = 300$ MHz centered at $f_c^{Noise} = 350$ MHz. Then, a triangular FMCW modulated signal is created with a modulation bandwidth of $W_{BP}^{FM} = 300$ MHz, frequency modulation period of $T_M = 1.0$ μ s, and center frequency of $f_c^{FM} = 350$ MHz. Finally, the noise signal was convolved with a triangular FMCW

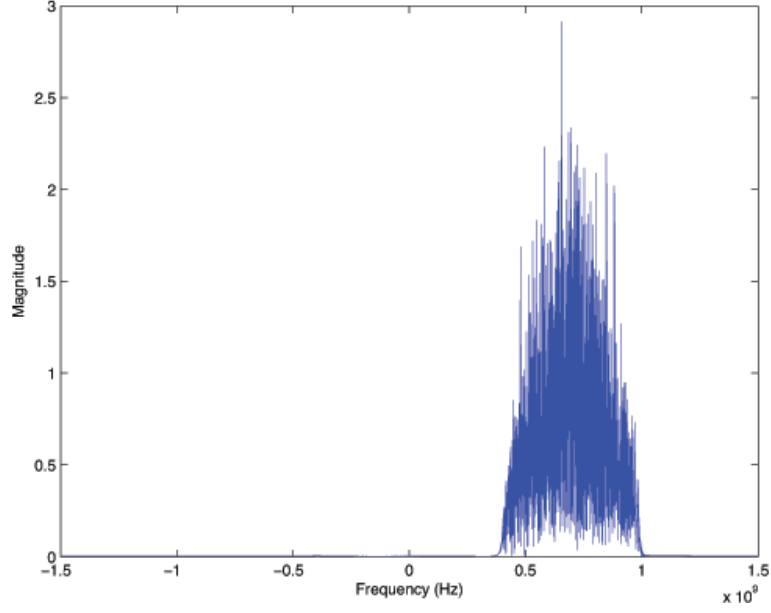


Figure 3.2: Spectral response of the simulated FMCW signal.

modulated signal and then was high pass filtered, removing the duplicate baseband signal. This produced a noise plus FMCW signal, which is the simulated FMCW signal with the following parameters in Table 3.1. The simulated FMCW signal produced has $N_S = 12.0$ k samples, a bandwidth of $W_{BP}^{FMCW} = 600$ MHz centered at $f_c^{FMCW} = 700$ MHz, waveform period of $T_T = 2.0 \mu s$, frequency modulation period of $T_M = 1.0 \mu s$, and is spectrally illustrated in Figure 3.2.

Table 3.1: Simulated FMCW Signal Parameters

| Parameter | Value |
|--|-------------|
| Sample Frequency (f_s) | 3.0 GHz |
| Noise Power (P_N) | -40 dBW |
| Bandwidth (W_{BP}^{FMCW}) | 600 MHz |
| Noise Bandwidth (W_{BP}^{AGWN}) | 300 MHz |
| FM Bandwidth (W_{BP}^{FM}) | 300 MHz |
| FMCW Center Frequency (f_c^{FMCW}) | 700 MHz |
| Frequency Modulation Period (T_M) | 1.0 μs |
| Waveform Period (T_T) | 2.0 μs |

Table 3.2: NTR System Components Configuration

| Hardware | Number |
|-------------------|-------------------------|
| Laptop | S/N: 3MMGRB1 |
| Transmitter ID | AFIT #4 |
| A/D Converter | AL 83 GTE 8054929 |
| High Gain Antenna | PCB Log Periodic WA5VJB |
| Stand | n/a |
| Cables | n/a |

3.4 Experimental NTR Signal

The section below describes the three collection configurations and their collection frequencies. Each configuration is a slight modification of the implementation monostatic NTR system described in Section 2.1 and is illustrated in Figure 2.2. Table 3.2 is the NTR system hardware configuration used during the collections. These configuration capture different levels of NTR signal “coloration” from the hardware with the goal of extracting the NTR characteristics and difference between NTR_{OFF} and NTR_{ON} conditions. Any definable characteristics in the NTR Source configuration, Configuration #1, should propagate forward into the other two configurations, Configurations #2 and Configuration #3. Also, any characteristics revealed in a higher number configuration and not in a lower number configuration can be attributed to the “coloration” in that particular configuration.

The NTR noise generator is a WB thermal noise source [25, 30]. For each collection configuration, the corresponding bandwidth was determined using WB RFSICS snapshots that were generated from the $W_{RF} = 36$ MHz NB filter scanning across the $f_c \in [0.02, 1.6]$ GHz range. The resultant Power Spectral Density (PSD) for collected NTR signals and each configuration are provided in Figure 3.3. The response in Figure 3.3 illustrates the NTR signals on a frequency and power axis which span $f \approx [0.02, 2.020]$ MHz and $[-110, -40]$ dBm. The center frequencies for NTR detectability analysis and demonstration were selected to coincide approximately with the center of the NTR signal bandwidth (W_{NTR}) and with the lower/upper roll-off

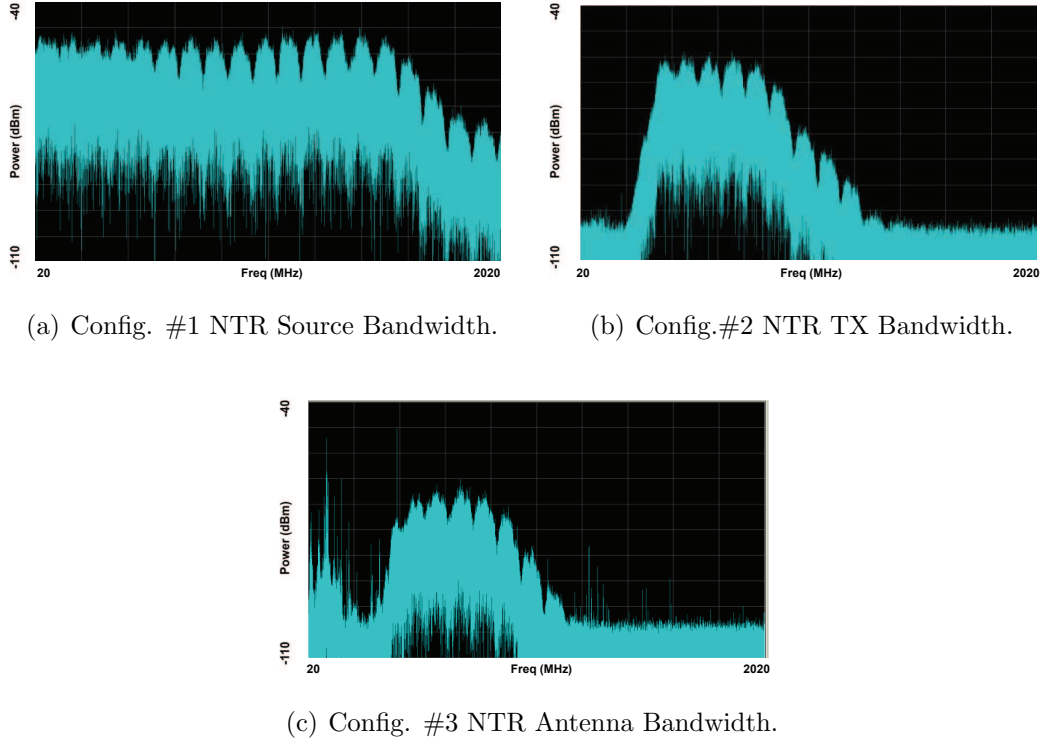


Figure 3.3: WB RFSICS PSD snapshot of the collected NTR signals for each configuration.

regions of W_{NTR} , as reflected in Figure 3.3(a), Figure 3.3(b), and Figure 3.3(c). The selected f_c for each of the configurations are listed in Table 3.3.

Table 3.3: RFSICS Center Frequencies (f_c) Used for NTR Collections.

| Configuration # | Low (MHz) | Mid (MHz) | High (MHz) |
|--------------------------------|-----------|-----------|------------|
| #1 Direct NTR Source Output | n/a | 580 | 1618 |
| #2 Direct NTR Tx Output | 373 | 581 | 800 |
| #3 Over Air Tx/Rx | 497 | 686 | 797 |

For collecting NTR signals, there were two conditions that were considered for pair-wise assessment, including NTR_{OFF} and NTR_{ON} . The NTR_{OFF} condition accounted for the collections including *background-only* noise responses. In this case,

the NTR system was off and not transmitting. The background noise consisted of emissions from devices typically operating in an office environment, i.e., computers, cellular phones, power transformers in lights, etc. For Configuration #1 and Configuration #2, the background noise level was low because the RFSICS was directly connected to the NTR transmitter. For Configuration #3, the collection receiver was connected to a high gain log-periodic antenna and collections included environmental background noise. The NTR_{ON} condition accounted for collections made while the NTR system was transmitting. Thus, the responses collected included the NTR signal plus background noise that was associated with the collection configuration.

3.4.1 Configuration #1: Direct NTR Noise Source. Configuration #1 is illustrated in Figure 3.4. The RFSICS was directly connected to the NTR noise generator which was thermal noise [25,30]. This configuration captured the characteristics that were truly inherent to the NTR noise generator. In this configuration, the NTR noise generator was connected by a 9.0 ft cable to a 15 dB attenuator. The attenuator was then directly connected to the power divider. From the power divider, the NTR signal was split into the RFSICS and the ADC, using two separate 3.0 ft cables. The ADC then fed the NTR signal into the spectrum analyzer on the laptop, which was used to verify that the NTR system was transmitting. On the other end, the RFSICS sent the NTR signal to another laptop that controlled the RFSICS and recorded the collections. For Configuration #1, the NTR signal $W_{config\#1}$ was ≈ 1.7 GHz and the f_c = for the two 36 MHz NB collections frequency were approximately $f_c = 580$ MHz (middle of the $W_{config\#1}$), and $f_c = 1681$ MHz (high frequency roll-off).

3.4.2 Configuration #2: Direct NTR Tx Output. Configuration #2 is illustrated in Figure 3.5. The RFSICS was directly connected to the NTR transmitter output. This configuration captured the NTR signal “colored” by filtering. Within the NTR transmitter, the NTR noise generator was filtered twice by a low and high

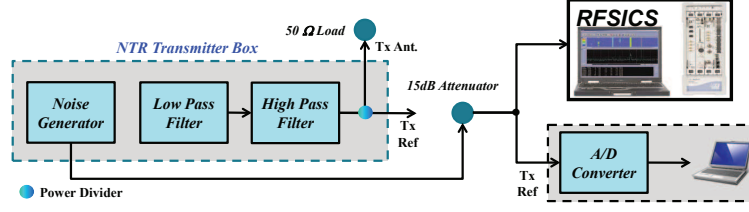


Figure 3.4: NTR Configuration #1, direct connection from the NTR Source.

pass filter. The NTR signal was then split. One end of the NTR transmitter output was terminated by a $R_L = 50 \, \Omega$ load and the other NTR transmitter output was connected by a 9.0 ft cable to a 15 dB attenuator. The attenuator was then directly connected to the power divider. From the power divider, the NTR signal was split into the RFSICS and the ADC, using two separate 3.0 ft cables. The ADC then fed the NTR signal into the spectrum analyzer on the laptop, which was used to verify that the NTR system was transmitting. On the other end, the RFSICS sent the NTR signal to another laptop, which controlled the RFSICS and recorded the collections. For Configuration #2, the NTR signal $W_{config\#2}$ was ≈ 400 MHz [30] and the f_c for the three 36 MHz NB collections frequency were approximately $f_c = 581$ MHz (middle of the $W_{config\#2}$), $f_c = 373$ MHz (low frequency roll-off), and $f_c = 800$ MHz (high frequency roll-off).

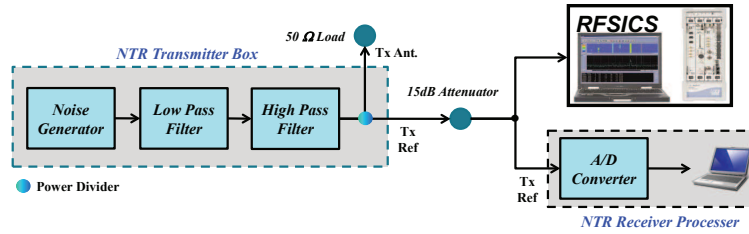


Figure 3.5: NTR Configuration #2, direct connection from the NTR Tx output.

3.4.3 *Configuration #3: Over Air Tx/Rx.* Configuration #3 is illustrated in Figure 3.6. The RFSICS and NTR transmitter were connected to two separate high gain log-periodic antennas. This configuration captured the NTR signal “colored” by filtering, the antennas, and air transmission background noise. Within the NTR transmitter block, the generated NTR noise signal was filtered twice: once by a low pass filter and once by a high pass filter. After filtering, the NTR signal was power divided with one output terminated by an $R_L = 50 \Omega$ load. The other output was the NTR transmitter output connected by a 9 ft cable to a 15 dB attenuator. The attenuator was then directly connected to the power divider. From the power divider, the NTR signal was split into high gain log-periodic antennas and the ADC, using two separate 3 ft cables. The ADC then fed the NTR signal into the spectrum analyzer on the laptop which was used to verify that the NTR system was transmitting. On the other end, the high gain log-periodic antenna was in close proximity (≈ 2 inches) to another high gain log-periodic antenna which was connected to the RFSICS with a 3 ft cable. The NTR signal was transmitted and received over the air. The RFSICS finally sent the NTR signal to another laptop, which controlled the RFSICS and recorded the collections. For Configuration #3, the NTR signal $W_{config\#3}$ was ≈ 400 MHz [30] and the f_c for the three 36 MHz NB collections frequency were approximately $f_c = 686$ MHz (middle of the $W_{config\#3}$), $f_c = 497$ MHz (low frequency roll-off), and $f_c = 797$ MHz (high frequency roll-off).

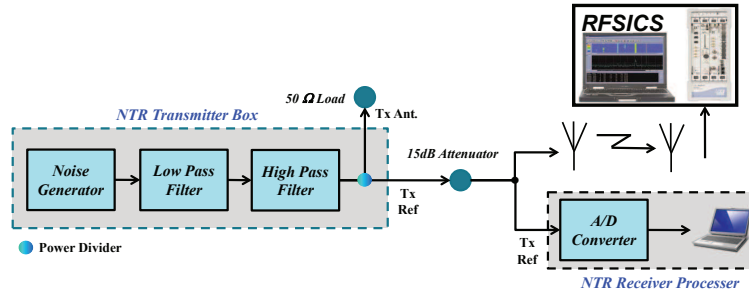


Figure 3.6: NTR Configuration #3, over the air transmission and receiver.

3.5 Post-Collection Processing

Figure 3.7 shows the post-collection processing that all collected data goes through prior to QMFB processing.

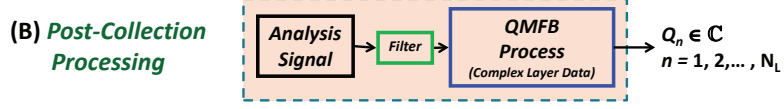


Figure 3.7: Post-collection processing.

3.5.1 Analysis Signal Generation. For a collection time period of $T_c = 4.0$ s RFSICS collection and a resultant baseband sample frequency of $f_s = 4.75$ Msps, the sequence of collected NTR signal samples $\{R(k)\}$ contained $N_S \approx 19$ million samples. To make post-collection processing manageable, a total of $N_Q = 2^n \ll N_S$ (n a positive integer) samples were taken from $\{R(k)\}$ to represent one *realization* of the NTR signal. The selection of the QMFB process input $N_Q = 2^n$ samples per realization is addressed further in Section 2.2.

3.5.2 Baseband Butterworth Filtering. The N_Q samples of $\{R(k)\}$ were filtered using a 6th-order low-pass baseband Butterworth filter with a bandwidth of $W_{BB} = 18$ MHz. Filtering the signal prior to processing removed undesired noise components. The $W_{BB} = 18$ MHz was the maximum available given an RFSICS RF bandwidth of $W_{RF} = 36$ MHz.

3.5.3 QMFB Processing. The filtered N_Q samples $\{R(k)\}$ were processed through the QMFB process as described in Section 2.2. This process produced multiple non-transformed QMFB (Q_n) matrices for $(n = 1, 2, 3, \dots, N_L)$, where N_L was the total number of layers based on (2.6). A specific layer of the non-transformed QMFB Q_n was chosen to be further processed.

3.6 Multiple Realizations

Section 4.1 was based on using one NTR realization with pre-conditioned Q_{CTM}^{GM} prior to graphic generation. In an attempt to increase visual features of the NTR characteristics, multiple realizations of the NTR signal were considered ($N_R > 1$). The N_R realizations were extracted from $\{R(k)\}$ and represented contiguous sub-sequences of the collected $\{R(k)\}$ sequence containing N_S samples. Therefore, the number of available NTR realizations N_R was dependent on the length of N_S and the choice of N_Q . Figure 3.8 is an illustration of the multiple realization process for the pre-conditioned Q_{CTM}^{GM} with additional pre-conditioning. The multiple realizations of Q_{CTM}^{GM} were averaged to suppress any anomalies and to emphasize any details that were apparent across the realizations. After the averaging, the matrix was globally normalized to compare NTR_{OFF} and NTR_{ON} collection conditions.

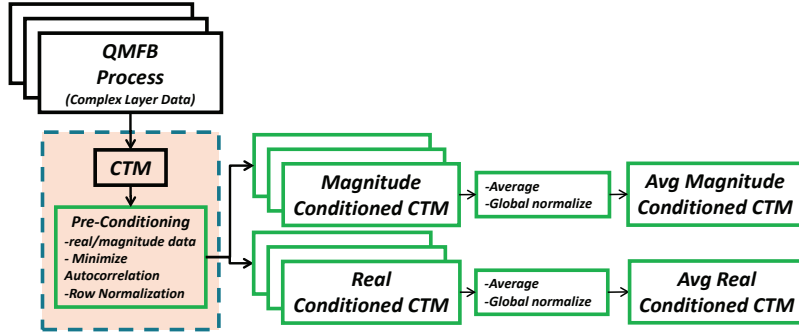


Figure 3.8: Detailed view of the multiple realizations of the pre-conditioned Q_{CTM}^{GM} .

3.6.1 Pre-Conditioning: Non-transformed QMFB. The Q_n was graphically represented using four graphic functions in MATLAB[®] described in Section 2.2 and Section 3.7. These graphic representations were successfully used in [11, 27] and represent the baseline for visual assessment of NTR signals in this research. However, in an attempt to graphically extract more features, data in the given Q_n were pre-conditioned before graphics generation.

The following provides details of various pre-conditioning steps that were considered in various orders during the research. Each collection condition was pre-conditioned individually, then pre-conditioned pair-wise. Using Q_n , the first pre-conditioning attempted was global *maximum magnitude* normalization in (3.2). Then, the resultant energy was converted to dB with (3.1). Lastly, pair-wise threshold/flooring was used for associated NTR_{OFF} and NTR_{ON} conditions using (3.10). Multiple combinations of these three pre-conditioning operations were attempted to reveal distinguishable features.

3.6.2 Pre-Conditioning: G-M Transformed QMFB. The G-M transformation process provides an alternate means for visually assessing potential information in the non-transformed QMFB output, Q_n . As adopted for this research and depicted in Figure 3.9, the G-M process has been used for assessing the detectability of UWB communication signals using a NB receiver [7, 8, 22, 23]. The G-M graphics visualization in [7, 8, 22, 23] was expanded under this research using the pre-conditioning of Section 3.1 as illustrated in Figure 3.9. The need for considering pre-conditions was driven by marginal visual detectability using the graphic functions in Section 3.7 with non-conditioned G-M matrices.

In the search to obtain the “best” results, multiple combinations of the pre-conditioning processes in Section 3.1 were attempted using trial-and-error. All of the considered combinations were qualitatively assessed using the MATLAB[®] graphics per Section 3.7. The operations attempted are illustrated in Figure 3.10 which shows that pre-conditioning was attempted both before and after all steps of the process.

3.7 Graphic Visual Assessment

Graphic visual assessment was performed for each matrix of interest, including non-transformed QMFB (Q_n), G-M transformed QMFB (Q_N^{GM} : Q_{TTM}^{GM} , Q_{CTM}^{GM} , Q_{SSM}^{GM} , Q_{CSM}^{GM}), and any variants thereof that had have been pre-conditioned per

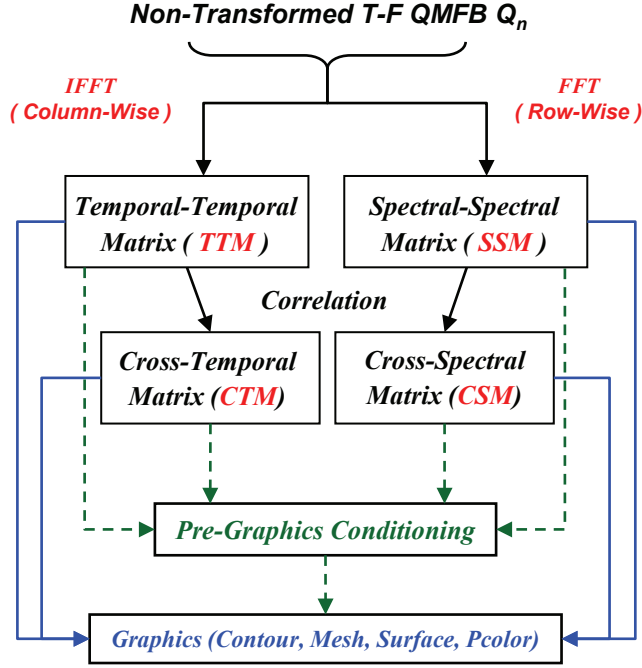


Figure 3.9: G-M process.

Section 3.1. As illustrated in Figure 3.1, this is accomplished using graphic functions of *contour*, *mesh*, *surface*, and *Pcolor* in MATLAB®. The *contour* graph is a 2-dimensional representation $Q(j, k)$ matrix with a time and frequency axis. The *mesh* graph is a 2-dimensional representation $Q(j, k)$ matrix with an energy and frequency axis. The *surf* graph is a 3-dimensional representation $Q(j, k)$ matrix with a time, frequency, and energy axis. The *Pcolor* graph is a 2-dimensional representation $Q(j, k)$ matrix with a time and frequency axis.

For all cases considered, graphics are provided for pair-wise assessment of NTR_{OFF} and NTR_{ON} conditions. This enables qualitative assessment of “What’s different?” in the pair of responses. The noted differences between *background-only* and *NTR-plus-background* responses represent a form of NTR signal detection, i.e., the “presence” of differences suggests that the NTR signal has influenced the composite response and its “presence” can be declared.

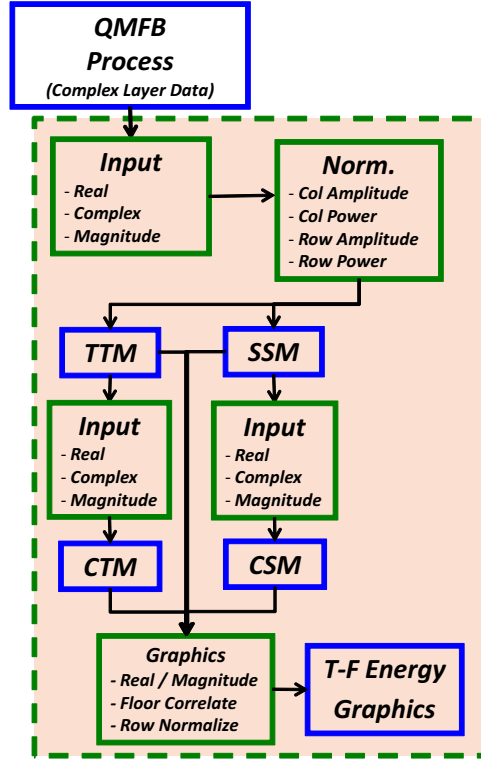


Figure 3.10: Pre-conditioning operations attempted for G-M transformed QMFB .

3.8 Wealth of Available Data

Accounting for all parameters of various processes depicted in Figure 3.1 and available for analyzing NTR detectability, there were a near-infinite number of scenarios that could be considered for analysis. To help quantify the number of possibilities, consider the following example:

1. $N_R = 1$ NTR realization (virtually unlimited N_R possibilities)
2. $N_{CC} = 3$ collection configurations
3. $N_{SB} = 9$ contiguous, non-overlapping NB sub-bands required to process entire NTR bandwidth of $W_{NTR} \approx 400$ MHz [30] using the RFSICS instantaneous bandwidth of $W_{RF} = 36$ MHz (virtually an unlimited number of N_{SB} as overlapping sub-bands are used)

4. $N_Q = 2^{N_L} = 2^{13}$ QMFB input samples produces $N_L = 13$ available Q_n output layer data and T-F matrices (virtually unlimited $N_Q = 2^{N_L}$ possibilities)
5. $N_{CL} = 1$ chosen layer from N_L complex T-F Q_n (12 of 13 available Q_n remain for $N_Q = 2^{13}$)
6. $N_{GM} = 4$ G-M transformations for Q_n

Accounting for parameters in #1 though #6 above, there were $N_R \times N_{CC} \times N_{SB} \times N_{CL} \times N_{GM} = 108$ complex T-F matrices available for graphic analysis. This was based on 27 non-transformed QMFB Q_n before G-M transformation and $27 \times 4 = 108$ Q_{TTM}^{GM} , Q_{CTM}^{GM} , Q_{SSM}^{GM} , and Q_{CSM}^{GM} after transformation. So in total, there are 108 possible matrices.

Using $N_{CL} = 1$ chosen layer, say Q_{12} , there were $N_G^Q = 4$ QMFB T-F graphics and $N_G^{preQ} = 2$ pre-conditioned QMFB T-F graphic representations (12 of 13 available Q_n remain). Applying G-M to given Q_{12} , there were $N_G^{GM} = 4$ G-M T-F graphics and $N_G^{preGM} = 1$ pre-conditioned G-M T-F graphic representations.

Considering the stated scenario conditions, there were

$$N_R \times N_{CC} \times N_{SB} \times N_{CL} \times (N_G^Q + N_G^{preQ} + N_G^{GM} + N_G^{preGM}) = 297 Graphics \quad (3.12)$$

There are 297 possible graphics for a single realization, three collection configuration, non-overlapping collection, and $N_Q = 2^{13}$ samples. Considering multiple realizations with the same conditions stated above and a collection duration of $T_c = 4s$ and using $N_Q = 2^{13}$ samples results in $N_R \approx 2,000$ realizations and more than 500 thousand matrices and graphics would be generated. The need for down-selection was obvious.

To complete the research within available time constraints and to ensure that only useful graphic data are presented, results were generated for a limited subset of available combinations. From these results, only a limited subset is presented

as required to support research conclusions. The final subset is based on empirical down-selection that took place at each step along the research. The down-selection was based on qualitative assessment of graphics per Section 3.7 and those representations that provided the most visually discernible features. The baseline for down-selection decisions is the previous research of [27].

Summary

This chapter provided the details for the detection process that was built on two previous areas of research. [27] research provided the foundation and [7, 8, 22, 23] provided another avenue to view the previous [27] research. Detailed step-by-step results for one realization of the detection process and results for the multiple realizations are described in Chapter 4.

IV. Results

This chapter provides results for NTR signal characterization using the qualitative visual assessment process outlined in Chapter III. Section 4.1 presents the baseline simulation results for the Quadrature Mirror Filter Bank (QMFB) process using the Frequency Modulated Continuous Wave (FMCW) signal described in Section 3.3. These results are based on QMFB process procedures in Section 3.5.3 and are presented for validation against previous work in [27]. This includes the assessment and selection of QMFB process input sample size (N_Q) and layer selection for the NTR signal analysis.

Section 4.2 and Section 4.3 provide a representative sequence of NTR results obtained using the step-by-step detection procedures outlined Sections 3.5 and 3.6. These results were for a single realization of the NTR signal using a single collection configuration as well as fixed collection and post-collection processing parameters, including: 1) RFSICS center frequency (f_c) and collection bandwidth (W_{RF}), 2) N_Q samples per NTR realization, and 3) QMFB layer number. This enabled the empirical selection of the “best” graphic representation(s) for visually distinguishing signal features. Section 4.2 and Section 4.3 address specific areas of interest, including the effects of: 1) signal collection and post-collection Butterworth filtering, 2) using the QMFB process (output designated as non-transformed QMFB, Q_n), and 3) using Gronholz-Mims (G-M) process (output designated as G-M transformed QMFB, Q_N^{GM}). Each section provides an initial assessment of a single realization of the NTR signal detectability using MATLAB[®] graphic functions comparing NTR_{OFF} and NTR_{ON} conditions.

Next, Section 4.4 provides the results using multiple realizations (N_R) of the NTR signal using the pre-conditioned Q_{CTM}^{GM} for each of the three collection configurations: Configuration #1 in Section 4.4.1, Configuration #2 in Section 4.4.2, and Configuration #3 in Section 4.4.3. These results were collectively assessed to

ascertain the “best” graphical representation(s) and parametric combination(s) for revealing NTR signal features, i.e., those which highlighted characteristic differences and enabled discernment of NTR_{OFF} and NTR_{ON} conditions.

This chapter concludes by addressing two issues that represent opportunities for near-term research contribution. This includes preliminary results for assessing Spectral Scalloping in Section 4.5.1 and the effects of Synthesized Bi-Phase Coding in Section 4.5.2. Detailed analysis within each of these areas could not be completed due to research time constraints.

4.1 FMCW Signal Processing

The simulated FMCW signal described in Section 3.3 was analyzed using the QMFB process in Section 3.5.3. Note, the QMFB process requires an input sample size (N_Q) that is an integer power of two, $N_Q = 2^{N_L}$, where N_L is an integer and the total number of QMFB layers for Q_n . For the QMFB process, signals with a collected sample size (N_S) that did not have an integer power of two have two options: 1) parse or 2) zero-pad N_S samples as described in Section 2.2. As adopted from [27], the FMCW signal generated has $N_S = 12,000$ samples. Since $\log_2(12,000) = 13.55$, N_S can either be parsed to $N_Q = 2^{13}$ samples or zero-padded to $N_Q = 2^{14}$ samples for processing. To focus on the signal, $N_Q = 2^{13}$ samples were first addressed.

Using the generated FMCW signal, the QMFB process was performed to generate multiple non-transformed QMFB (Q_n) matrices for each ($n = 1, 2, 3, \dots, N_L$). Each of these Q_n matrices are graphically represented using the graphical functions in MATLAB[®] described in Section 3.7. In particular, the four MATLAB[®] graphic functions utilized are *contour*, *mesh*, *surface*, and *Pcolor*. These four graphical representations are illustrated for Layer #4 to Layer #8 of the FMCW signal in Figure 2.4 and Appendix A. The *contour* graphic was ultimately chosen for further analysis because it visually presented the most structured appearance with distinguishable characteristics closely matching those of the generated signal. This is illustrated

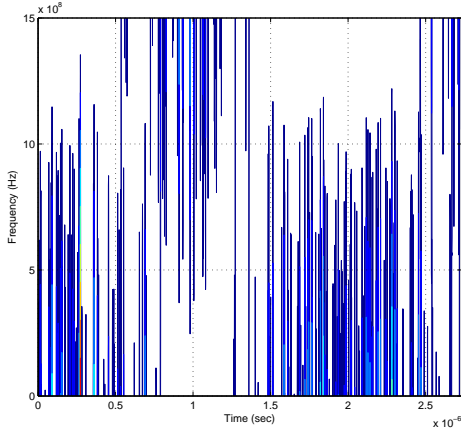
for the FMCW signal in Figure 4.1 and Figure 4.2 which depict Q_n as a *contour* graphics for $N_L = 13$ layers. However, there is no Q_{13} figure because Q_{N_L} is fully decimated to a vector. Consistent with previous work [11, 27], the response in Figure 4.3(a), Layer #6, has a triangular waveform response with a signal bandwidth of $W_{BP} \approx 600$ MHz, FM bandwidth of $W_{BP}^{FM} \approx 300$ MHz, signal period of $T_T \approx 2.0\mu s$, frequency modulation period of $T_M \approx 1.0\mu s$, and center frequency of $f_c \approx 700$ MHz.

Figure 4.3 To properly choose the appropriate N_Q sample size for further research, the zero-padded $N_Q = 2^{14}$ samples of the FMCW were also analyzed using the QMFB process. Comparative Layer #6 results for $N_Q = 2^{13}$ and $N_Q = 2^{14}$ samples are illustrated in Figure 4.3. When observing Figure 4.3, it was evident that the parsed FMCW with $N_Q = 2^{13}$ samples (left) yielded the same signal information as the zero-padded FMCW with $N_Q = 2^{14}$ samples (right). As a result, N_L is dependent on the parsed, signal-only sample size as in (2.7).

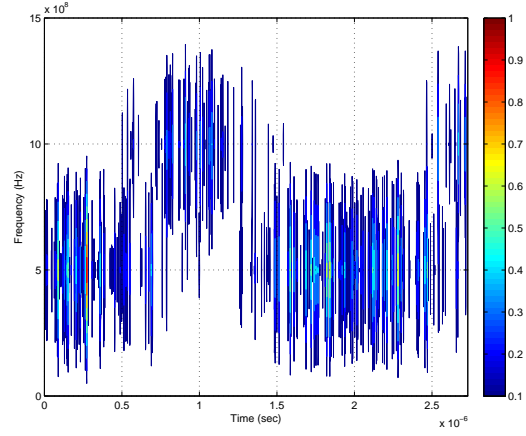
The results presented in this section are consistent with the analysis provided in [27] for QMFB processing of the FMCW signal. Research in [27] concluded that the *contour* graphic of Layer #6 had the same signal characteristics as presented here—validating that the QMFB process in Section 3.5.3 was properly implemented for subsequent application to the NTR signal. Thus, *contour* graphics of Layer #6 based on $N_Q = 2^{13}$ samples per realization was used for initial NTR investigation.

4.2 NTR Signal Processing

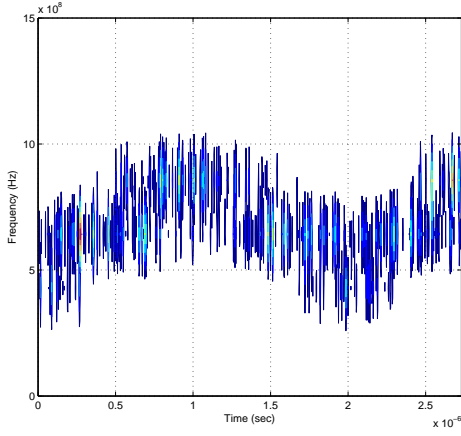
For initial NTR investigation, the collection scenario and post-collection parameters remained fixed throughout the detection process in Chapter III and Figure 3.1. The scenario included using collection Configuration #2 with a single realization of $N_Q = 2^{13}$ NTR samples collected with the RFSICS using $f_c = 581$ MHz and collection bandwidth of $W_c = 36$ MHz. This section also highlights empirical decisions that were made to limit the number of parameters and methods considered.



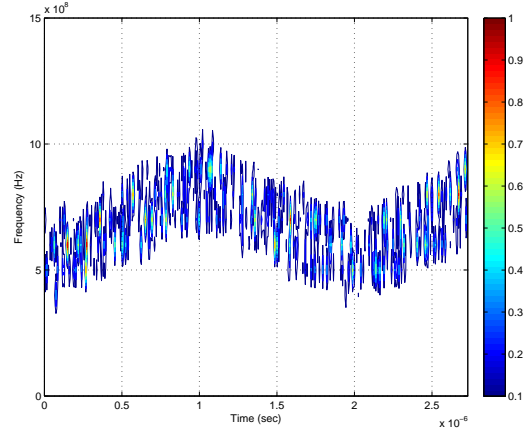
(a) Layer #1 (Q_1).



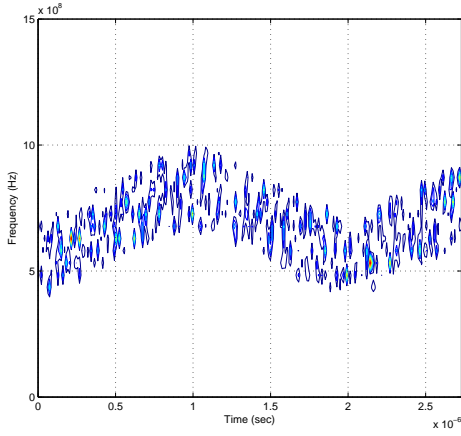
(b) Layer #2 (Q_2).



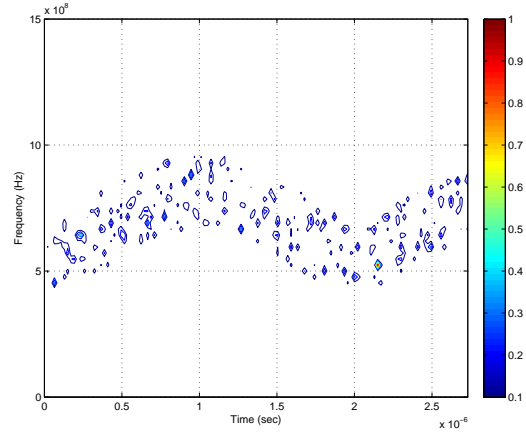
(c) Layer #3 (Q_3).



(d) Layer #4 (Q_4).

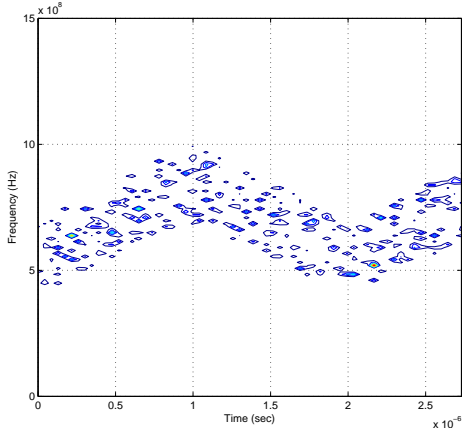


(e) Layer #5 (Q_5).

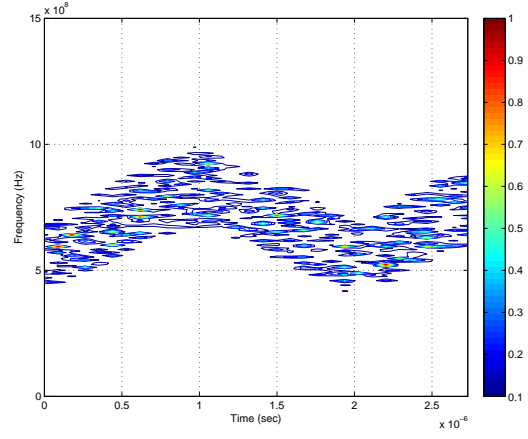


(f) Layer #6 (Q_6).

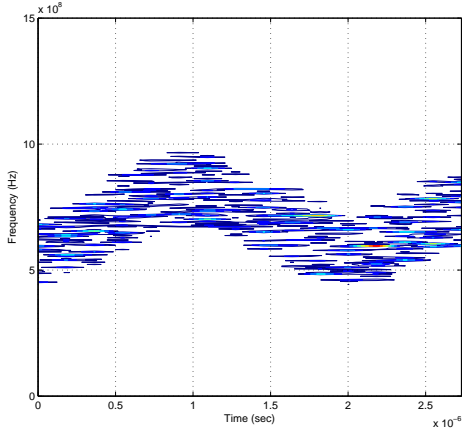
Figure 4.1: Baseline FMCW signal: *Non-Transformed QMFB* (Q_n) *contour* T-F Graphics for Layer #1 to Layer #6 using $N_Q=2^{13}$ samples.



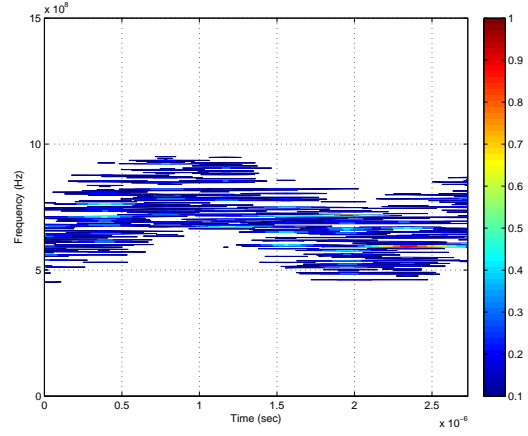
(a) Layer #7 (Q_7).



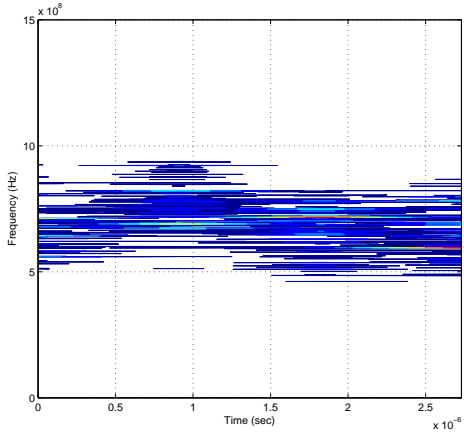
(b) Layer #8 (Q_8).



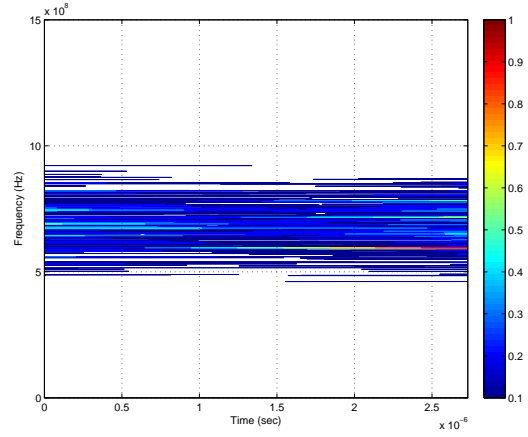
(c) Layer #9 (Q_9).



(d) Layer #10 (Q_{10}).



(e) Layer #11 (Q_{11}).



(f) Layer #12 (Q_{12}).

Figure 4.2: Baseline FMCW signal: *Non-Transformed QMFB* (Q_n) *contour* T-F graphics for Layer #7 to Layer #12 using $N_S = 2^{13}$ samples.

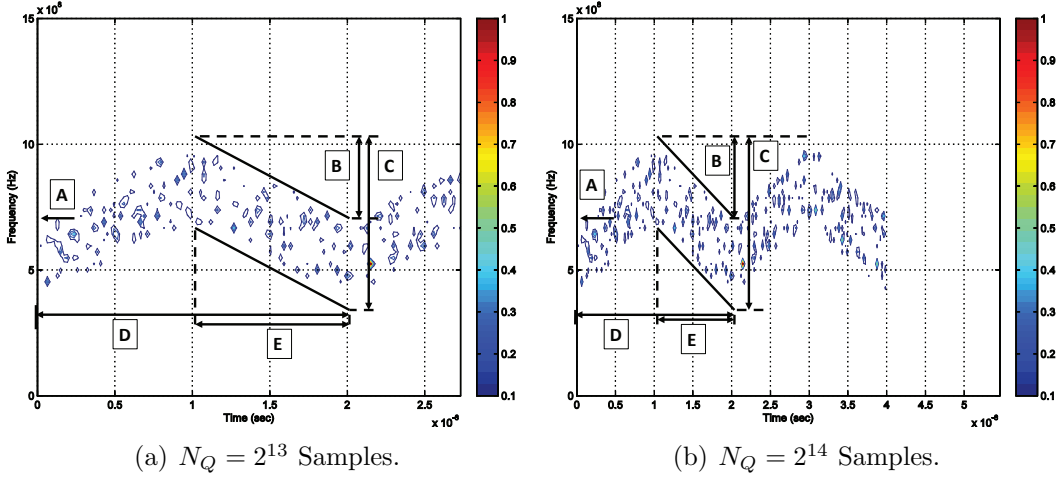


Figure 4.3: Baseline FMCW signal with $N_S = 12,000$ samples: Q_6 contour T-F graphics with (a) $N_Q = 2^{13}$ (parsed) and (b) $N_Q = 2^{14}$ (zero-padded) samples. Figure labels: A) $f_c = 700$ MHz, B) $W_{BP}^{FM} = 300$ MHz, C) $W_{BP} = 600$ MHz, D) $T_T = 2 \mu s$, and E) $T_M = 1 \mu s$.

$N_Q = 2^{13}$ samples was chosen because of success achieved in [27] and re-verified in Section 4.1. The two primary collection conditions are denoted as NTR_{OFF} (only background noise present) and NTR_{ON} (background plus NTR signal present). Each area of interest in the overall NTR detection process is detailed next, including the effects of: 1) signal collection and post-collection Butterworth filtering, 2) using the QMFB process (output designated as *non-transformed* QMFB, Q_n), and 3) using the Gronholz-Mims (G-M) process (output designated as G-M transformed QMFB, Q_N^{GM}).

4.2.1 Collection and Butterworth Filtering. Using NTR collection Configuration #2 in Section 3.4.2, received signals, $R(t)$, were collected for the NTR_{OFF} and NTR_{ON} conditions. The collected signals were then processed per Section 3.5. As a first step, the complex I&Q samples of $R(t)$ were parsed into contiguous sequences (realizations) of $N_Q = 2^{13}$ samples. Figure 4.4 illustrates temporal (top) and spectral (bottom) responses that are representative of one realization of NTR_{OFF} and NTR_{ON} conditions with $N_Q = 2^{13}$ samples. The amplitude in the NTR_{ON}

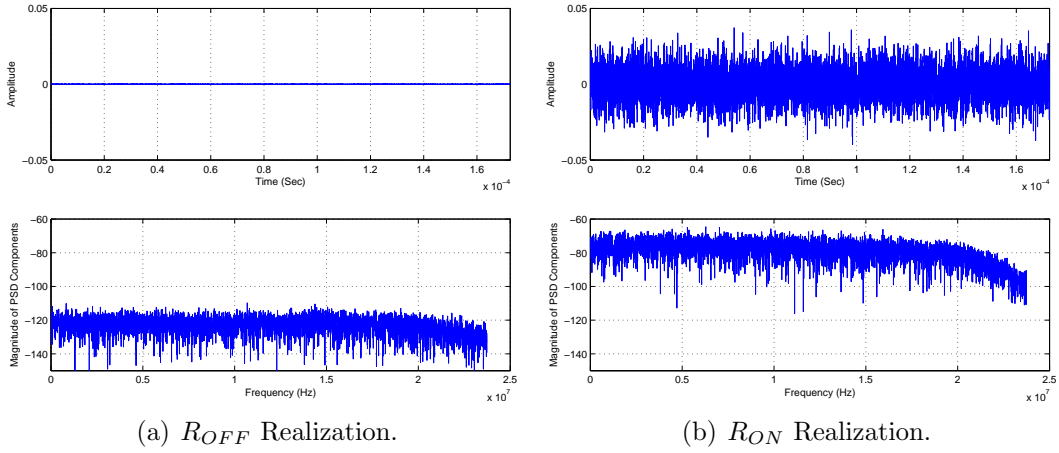


Figure 4.4: One realization for NTR_{OFF} and NTR_{ON} conditions with $N_Q = 2^{13}$ samples: temporal (top) and spectral (bottom) responses.

condition is 100 times greater than that of the NTR_{OFF} condition. This difference is clearly reflected in the PSD of the responses as well.

For both cases, $R(t)$ with N_Q sample sizes were baseband Butterworth-filtered as per Section 3.5.2 using a bandwidth of $W_{BB} = 18$ MHz. This produced the Butterworth-filtered $R(t)$ responses and corresponding PSD responses, illustrated in Figure 4.5. The spectral effect of the Butterworth filter is clearly evident by comparing the higher-frequency PSD responses (regions above 18 MHz) in Figure 4.4 and Figure 4.5.

4.2.2 QMFB Processing. Once filtered per Section 4.2.1, the resultant output $R(t)$ with $N_Q = 2^{13}$ samples were QMFB processed. This produced $N_L = 13$ layers of *non-transformed* QMFB output data that were stored as complex I&Q samples in multiple Q_n matrices ($n = 1, 2, \dots, N_L$). Per the discussion and justification provided in Section 4.1, only Layer #6 results are presented here for graphical generation using the four MATLAB[®] graphic functions: *contour*, *mesh*, *surface*, and *Pcolor* described in Section 3.7. Figure 4.6 and Figure 4.7 illustrate Q_6 as *contour* (top-left), *mesh* (top-right), *surface* (bottom-left), and *Pcolor* (bottom-right) for NTR_{OFF} and

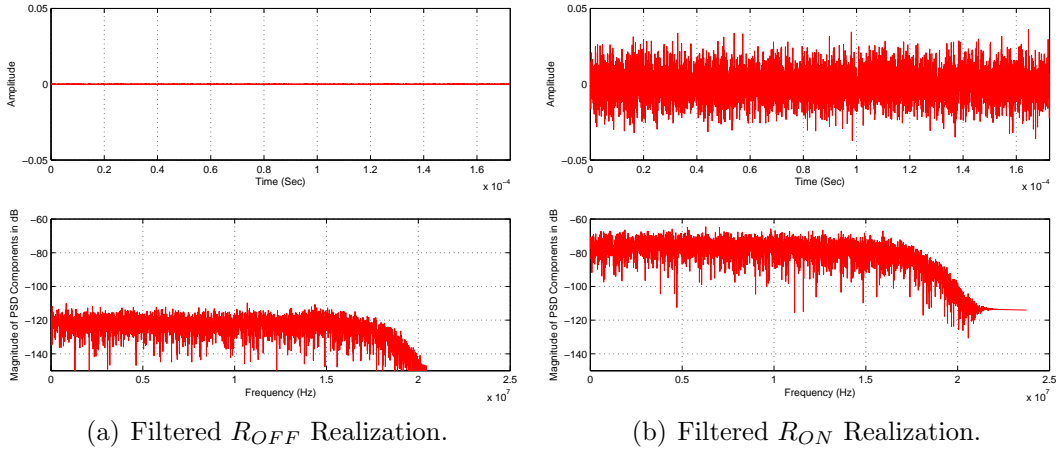


Figure 4.5: Post-collection Butterworth filtered NTR responses of NTR_{OFF} and NTR_{ON} with $N_Q = 2^{13}$ samples temporal realizations in Figure 4.4.

NTR_{ON} conditions, respectively. The energy in NTR_{ON} is 1000-times larger than NTR_{OFF} . The frequency ranges in the figures illustrate only the positive frequencies $f \in [0, 18]$ MHz and the signal time duration of $T_s = 0.17$ ms. Initial assessment of these graphics for all other QMFB layers revealed minimal distinguishable signal characteristics for both NTR_{OFF} and NTR_{ON} conditions. However, the *contour* and *Pcolor* graphics seemed the most promising for subsequent consideration and were considered further.

As a next step, Q_6 was pre-conditioned by 1) global *maximum magnitude* normalizing the magnitude of Q_6 using (3.1), 2) converting the squared resultant Q_6 energy responses to dB using (3.2), and 3) pair-wise flooring of the resulting matrix using (3.10). The pre-conditioned Q_6 was then graphically represented using the *contour* and *Pcolor* graphics in Figure 4.8 and Figure 4.9, respectively. This ensured that resultant *contour* graphics would have the same step size and have comparable scales. Upon observation, there were only slight differences between the NTR_{OFF} and NTR_{ON} responses. For the graphics considered thus far, there was no consistent or distinguishable characteristics in the responses and minimal insight is gained into detecting the NTR_{ON} condition. This motivated the need to

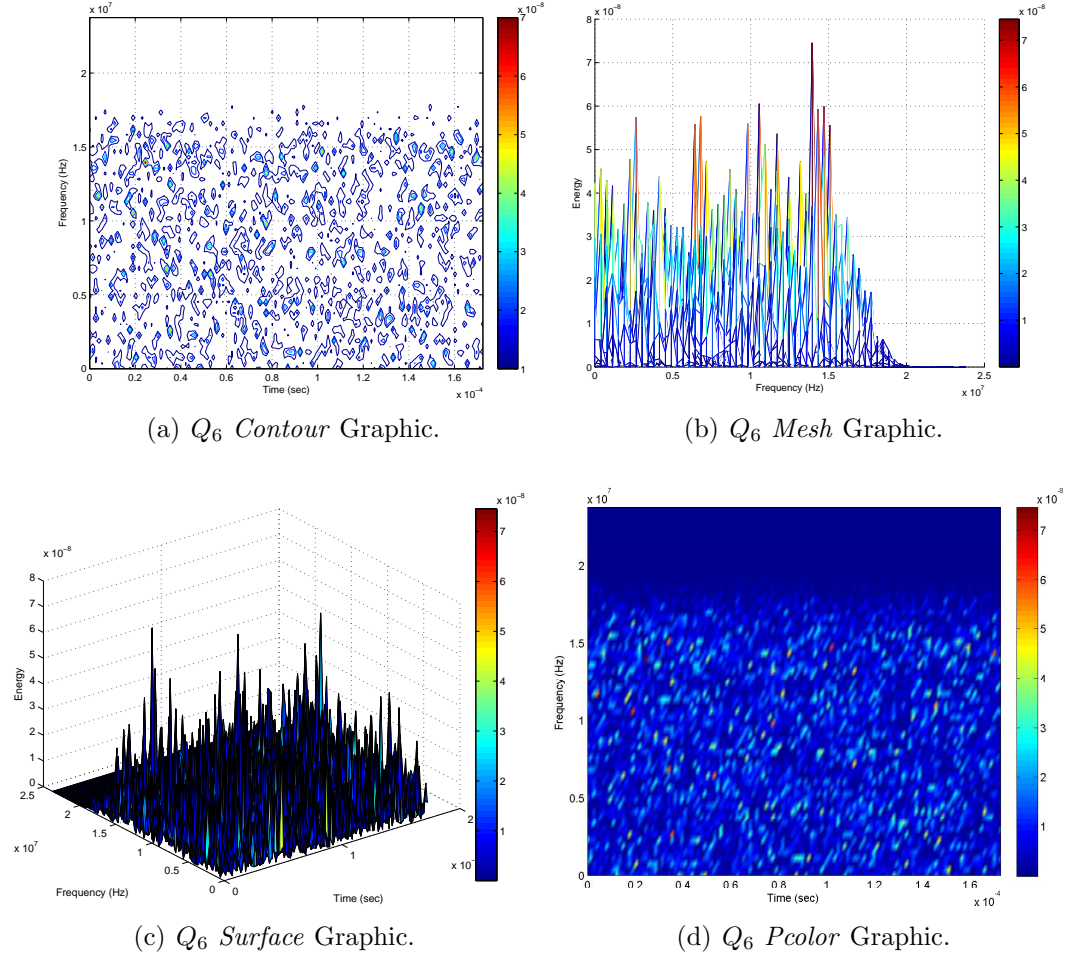


Figure 4.6: Four graphical representation (as indicated) of the *Non-Transformed* QMFB (Q_6) for Layer #6 NTR_{OFF} condition using $N_Q = 2^{13}$ samples.

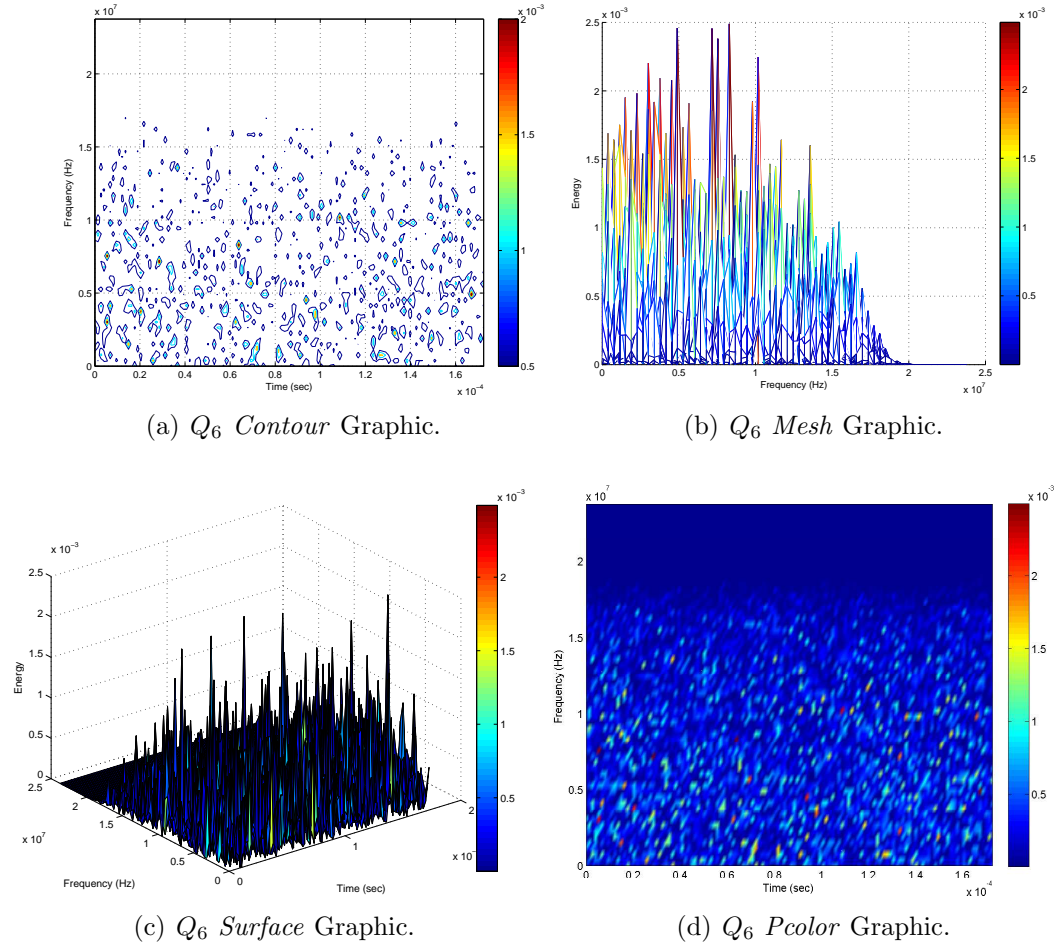
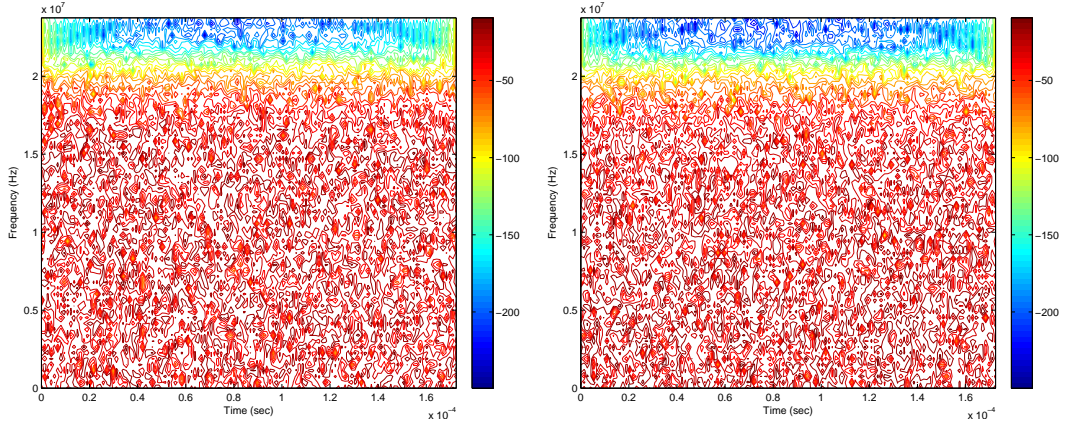


Figure 4.7: Four graphical representation (as indicated) of the *Non-Transformed* QMFB (Q_6) for Layer #6 NTR_{ON} condition using $N_Q = 2^{13}$ samples.

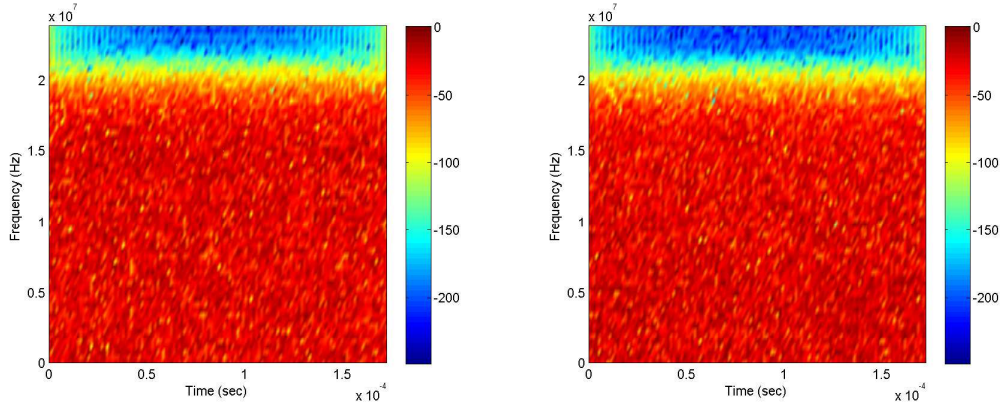
consider alternatives, and the research progressed to applying the G-M process after the QMFB process.



(a) Q_6 Response (dB) for NTR_{OFF} .

(b) Q_6 Response (dB) for NTR_{ON} .

Figure 4.8: Pre-conditioned *Non-Transformed* QMFB Layer #6 (Q_6) *contour* graphics (dB scale) using $N_Q = 2^{13}$ samples: (a) NTR_{OFF} and (b) NTR_{ON} Conditions.



(a) Q_6 Response (dB) for NTR_{OFF} .

(b) Q_6 Response (dB) for NTR_{ON} .

Figure 4.9: Pre-conditioned *Non-Transformed* QMFB Layer #6 (Q_6) *Pcolor* graphics (dB scale) using $N_Q = 2^{13}$ samples: (a) NTR_{OFF} and (b) NTR_{ON} Conditions.

4.3 NTR G-M Processing

As detailed in Section 3.6.2, the G-M process was used to transform the output of a given non-transformed QMFB layer (Q_n) into four different G-M transformed outputs. Given that *Pcolor* graphics provided the best clarity in previous results, only *Pcolor* graphics is considered henceforth. Each G-M transformation produced complex output samples that were stored in a matrix. These matrices are identified here according to the type of G-M transform that has been applied and includes: Q_{TTM}^{GM} for Temporal-Temporal Matrix (TTM) transformation, Q_{CTM}^{GM} for Cross-Temporal Matrix (CTM) transformation, Q_{SSM}^{GM} for Spectral-Spectral Matrix (SSM) transformation, and Q_{CSM}^{GM} for Cross-Spectral Matrix (CSM) transformation. In practice, there are actually two different ways to generate correlation-based Q_{CTM}^{GM} and Q_{CSM}^{GM} results, one by performing row-wise cross-correlation and another by performing column-wise cross-correlation [7, 8, 22, 23] in (3.11). Generally, the G-M process produces a G-M transformed QMFB represented as Q_N^{GM} , and specific G-M transformations are referred to as Q_{TTM}^{GM} , Q_{CTM}^{GM} , Q_{SSM}^{GM} , and Q_{CSM}^{GM} , where N = layer number.

4.3.1 Single NTR Realization. The effect of the G-M process on non-transformed QMFB output data is illustrated using the same NTR_{OFF} and NTR_{ON} realizations and Q_6 data from Section 4.2.2. Results for the two non-correlated Q_{TTM}^{GM} and Q_{SSM}^{GM} cases are presented in Figure 4.10, which illustrates Q_{TTM}^{GM} (top) and Q_{SSM}^{GM} (bottom) *Pcolor* graphics for NTR_{OFF} (left) and NTR_{ON} (right) conditions as indicated. Results for two of the four possible correlation-based transformations, Q_{CTM}^{GM} and Q_{CSM}^{GM} , are presented in Figure 4.11 for row-wise correlation. These results illustrate Q_{CTM}^{GM} (top) and Q_{CSM}^{GM} (bottom) results using *Pcolor* graphics for NTR_{OFF} (left) and NTR_{ON} (right) conditions as indicated. The row-wise results are presented here because they provided the greatest discernibility. Note that the scales for NTR_{OFF} and NTR_{ON} conditions in Figure 4.10 and Figure 4.11 are not the same, and therefore, the results cannot be compared directly. However, among

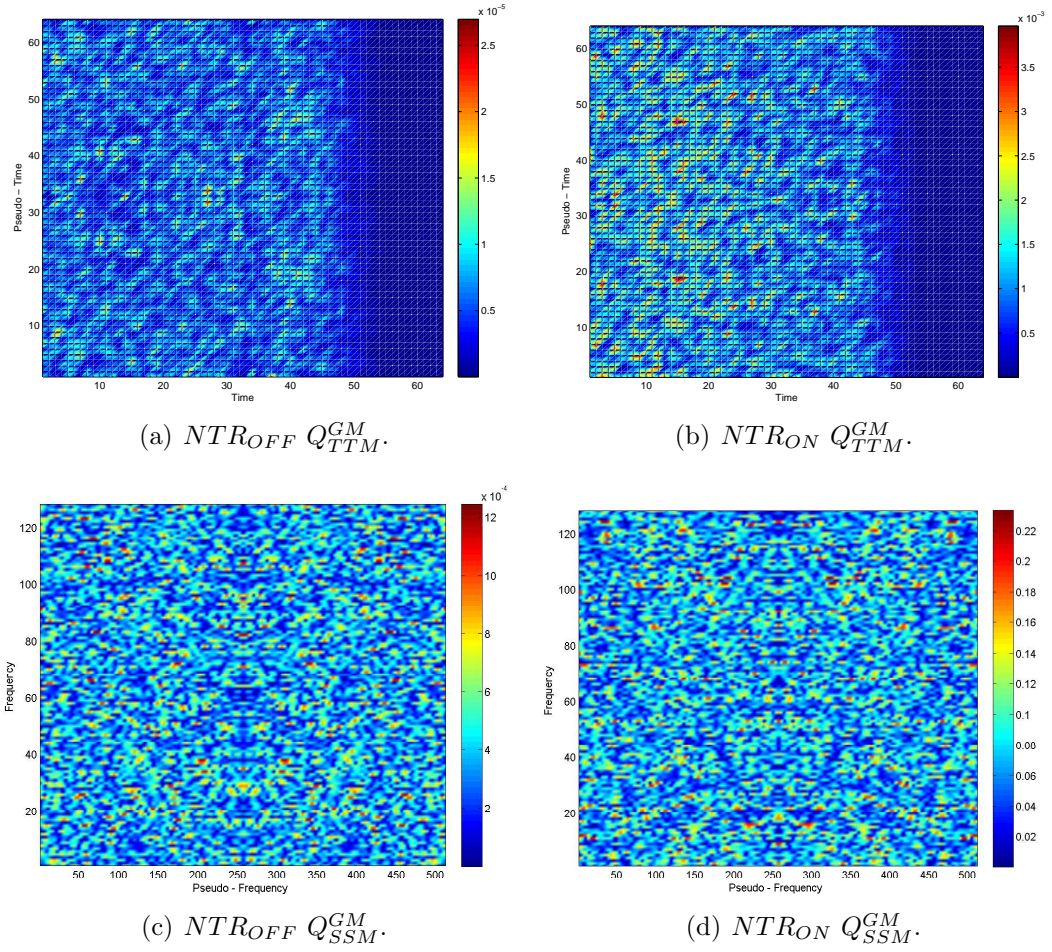


Figure 4.10: G - M Transformed QMFB Layer #6 (Q_6) P color graphics using non-correlated TTM (top) and SSM (bottom) data with $N_Q = 2^{13}$ samples.

the figures presented only the row-wise CTM response visually appears to have a distinct pattern. Therefore, row-wise CTM was selected for generating Q_{CTM}^{GM} and considered for further evaluation using pre-conditioning to enhance the visually discernible features.

In an attempt to enhance and extract features from the Q_{CTM}^{GM} , multiple pre-configuration combinations were attempted in Figure 3.10 from Section 3.1. Presented below was chosen as the “best” configuration.

1. $Real [Q_6] (\mathbb{R})$

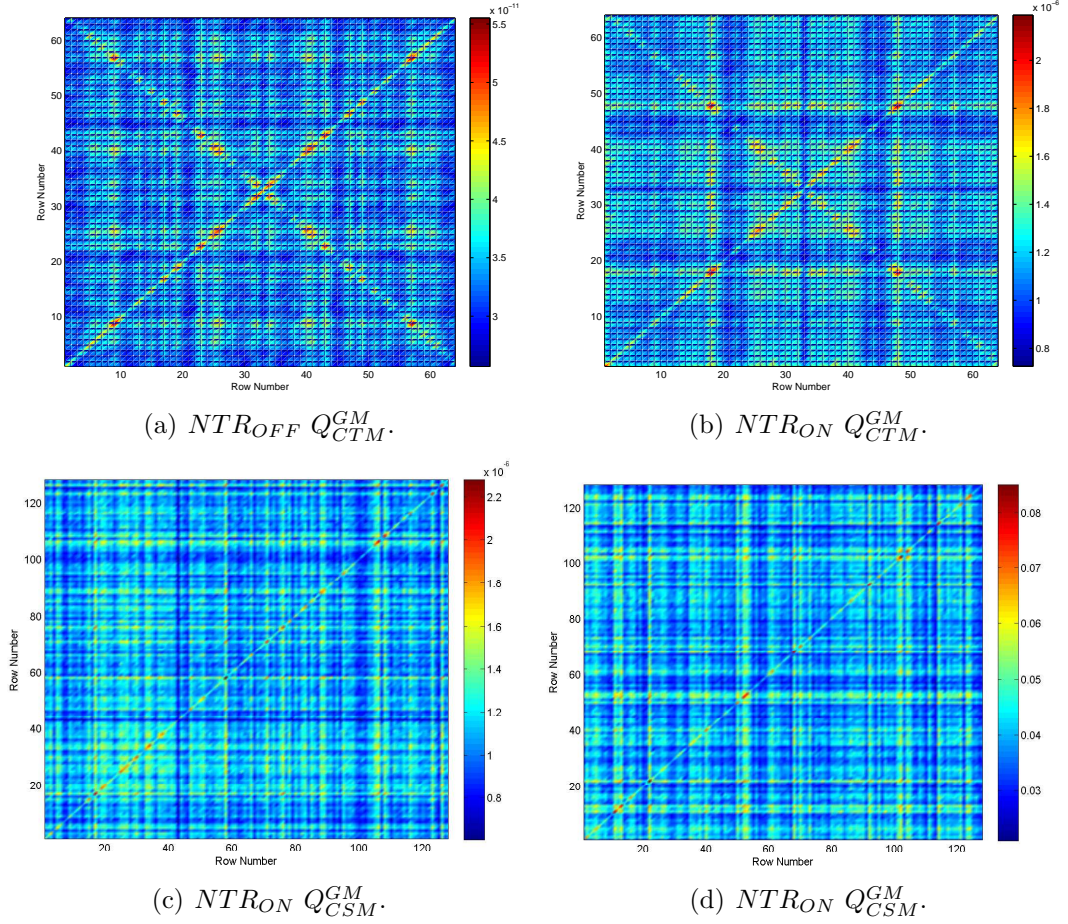


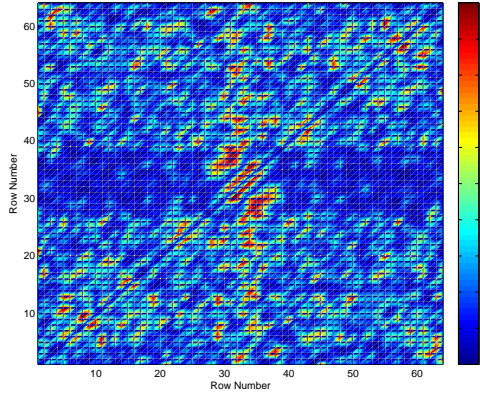
Figure 4.11: G - M Transformed QMFB Layer #6 (Q_6) $Pcolor$ graphics using row-wise correlated CTM (top) and CSM (bottom) data with $N_Q = 2^{13}$ samples.

2. Row-Wise *Power* Normalization using (3.5)
3. Calculate Q_{TTM}^{GM} from Section 2.3
4. Use the Q_{TTM}^{GM} (\mathbb{C})
5. Row-Wise Cross-Correlation [7,8] using (3.11)
6. Take the magnitude. $|Q_{CTM}^{GM}|$
7. Threshold/Floor the autocorrelation diagonal using (3.9)
8. Row-Wise *Maximum Magnitude* Normalization using (3.3)

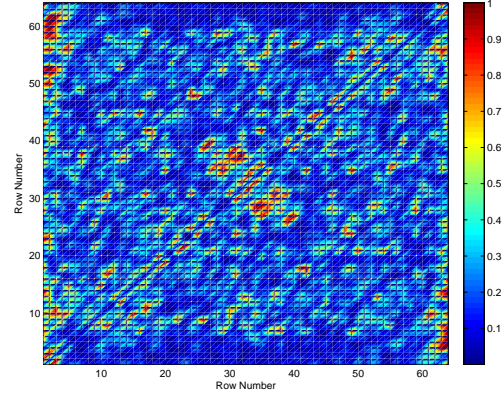
Since cross-correlation values are complex in process #5 above, the absolute real and magnitude values were evaluated for proceeding processes #6 through #8 above and are illustrated in Figure 4.12. These figures illustrate the absolute real value results (top) and magnitude value results (bottom) using *Pcolor* for NTR_{OFF} (left) and NTR_{ON} (right) conditions as indicated. The magnitude-based response seemed to reveal a more distinct pattern. Therefore, the magnitude-valued responses of the preconditioned Q_{CTM}^{GM} were selected for further processing. However, discernibility between responses for NTR_{OFF} and NTR_{ON} conditions using the pre-conditioned Q_{CTM}^{GM} remained low, and additional improvement was sought. Thus, the research shifted from processing a single NTR realization to evaluating performance using multiple NTR realizations. This was done to determine if any “processing gain” could be realized and provide increased visual discernibility.

4.4 Multiple NTR Realizations: Pre-Conditioned Q_{CTM}^{GM}

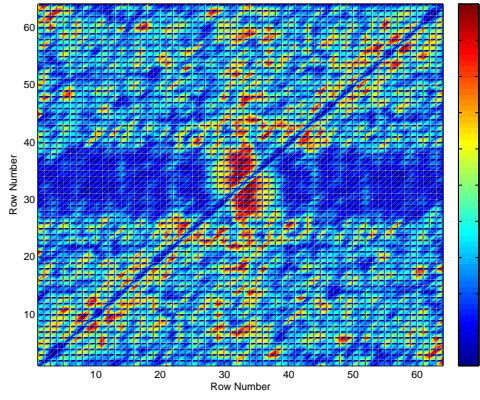
Multiple NTR realizations of the pre-conditioned Q_{CTM}^{GM} were evaluated to characterize how the NTR signal response changes over time. The six sequential realizations of the pre-conditioned Q_{CTM}^{GM} are graphically illustrated using *Pcolor* in Figure 4.13 and Figure 4.14 for NTR_{OFF} and NTR_{ON} conditions, respectively. These figures illustrate that the pre-conditioned Q_{CTM}^{GM} response changes over time and that responses for both collection conditions share some similar traits. To obtain



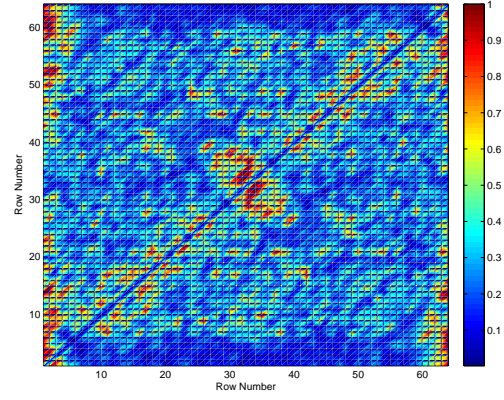
(a) NTR_{OFF} : Abs. Real Value of Q_{CTM}^{GM} .



(b) NTR_{ON} : Abs. Real Value of Q_{CTM}^{GM} .



(c) NTR_{Off} : Magnitude of Q_{CTM}^{GM} .



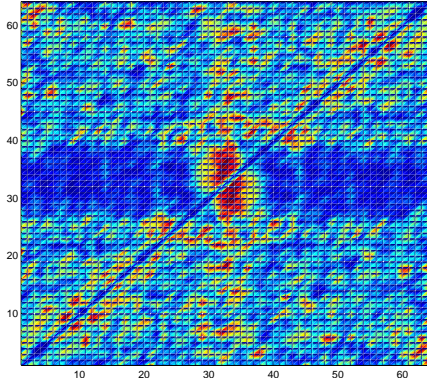
(d) NTR_{ON} : Magnitude of Q_{CTM}^{GM} .

Figure 4.12: Pre-conditioned Q_{CTM}^{GM} QMFB Layer #6 (Q_6) *Pcolor* graphics using the absolute real values (top) or magnitude values (bottom) of the CTM data with $N_Q = 2^{13}$ samples.

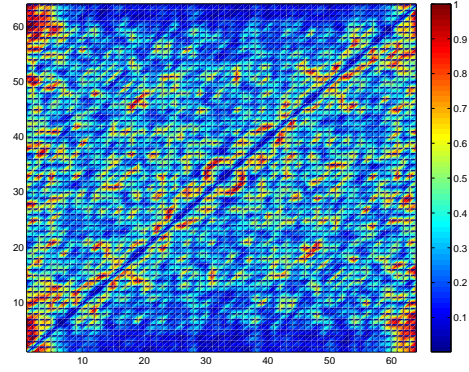
a single comparable figures, the multiple realizations of the pre-conditioned Q_{CTM}^{GM} were again pre-conditioned by: 1) calculating the multiple realization of Q_{CTM}^{GM} , 2) averaging the results and 3) global *maximum magnitude* normalizing the data using (3.2). This created multiple realizations of the pre-conditioned Q_{CTM}^{GM} and is illustrated in Figure 4.15 with $N_Q = 2^{13}$ samples and $N_R = 3000$ realizations for both NTR_{OFF} (left) and NTR_{ON} (right) conditions. These figures illustrate some slight differences between NTR_{OFF} and NTR_{ON} with a subtle pattern emerging. Given that these were the most discernible features observed up to this point in the research, multiple realization processing was carried into the final phase of the research, and performance characterized for scenario variation in 1) collection configuration number, 2) center frequency (f_c), and 3) number of input samples to the QMFB process (N_Q). The N_Q values are closely associated with the number of realizations (N_R) used and the collected sample size (N_S) described in Section 3.6. Therefore, for each N_Q , there is a particular N_R .

4.4.1 Configuration #1: Direct NTR Noise Source. Results here are for Configuration #1 as detailed in Section 3.4.1 and depicted in Figure 3.4. The effect of three NTR N_Q sample sizes were analyzed for the two f_c . Then, the “best” overall N_Q and f_c scenario were selected because these values extracted the most signal characteristics and highlighted distinct differences between NTR_{OFF} and NTR_{ON} conditions from Configuration #1.

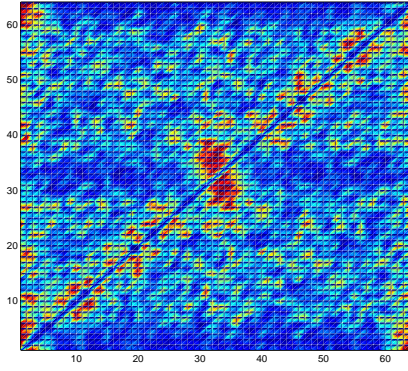
The *multiple realization* of the pre-conditioned Q_{CTM}^{GM} for Configuration #1 are graphically-illustrated as *Pcolor* in Section 4.4.1.1, Section 4.4.1.2, and Section 4.4.1.3. These graphics were based on using three different N_Q for $f_c = 580$ MHz and $f_c = 1618$ MHz. When comparing the performance for different N_Q and f_c values and for NTR_{OFF} / NTR_{ON} conditions, the differences appeared minute, and it was very difficult to visually discern between the two. However, one particular N_Q and f_c scenario visually appeared to have a slightly more discernible difference



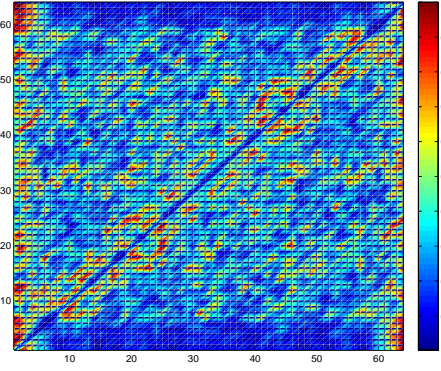
(a) NTR_{OFF} Realization 1.



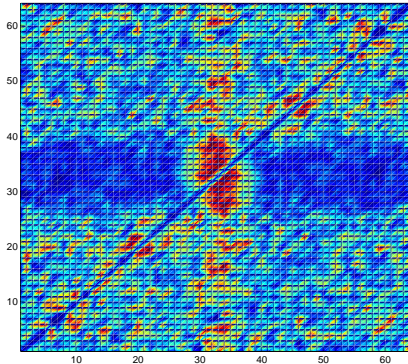
(b) NTR_{OFF} Realization 2.



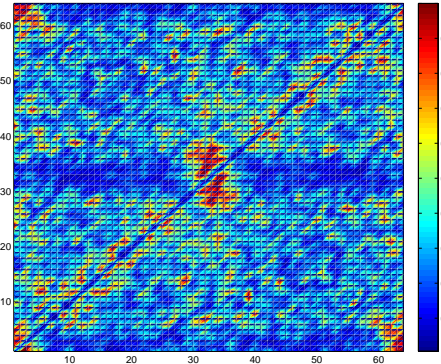
(c) NTR_{OFF} Realization 3.



(d) NTR_{OFF} Realization 4.

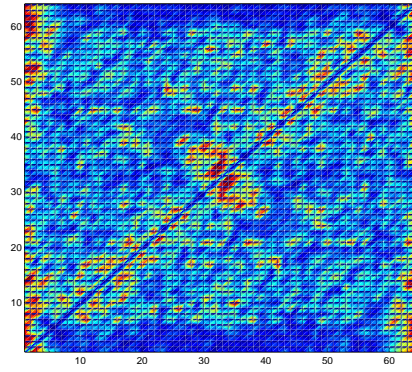


(e) NTR_{OFF} Realization 5.

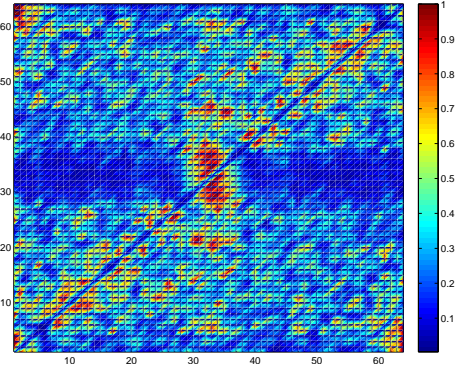


(f) NTR_{OFF} Realization 6.

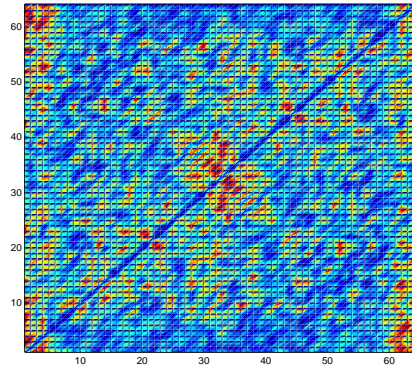
Figure 4.13: Six sequential realizations of the pre-conditioned Q_{CTM}^{GM} $Pcolor$ graphics for NTR_{OFF} using $N_S = 2^{13}$ samples.



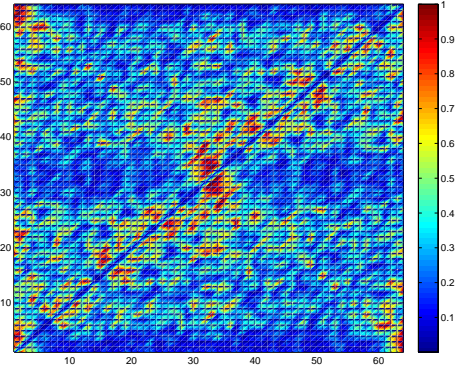
(a) NTR_{ON} Realization 1.



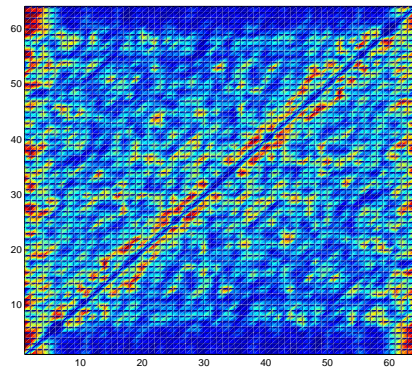
(b) NTR_{ON} Realization 2.



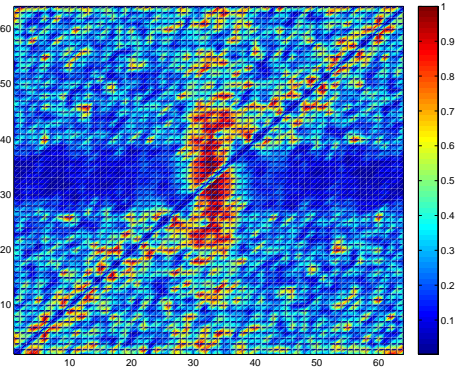
(c) NTR_{ON} Realization 3.



(d) NTR_{ON} Realization 4.



(e) NTR_{ON} Realization 5.



(f) NTR_{ON} Realization 6.

Figure 4.14: Six sequential realizations of the pre-conditioned Q_{CSM}^{GM} $Pcolor$ graphics for NTR_{ON} using $N_S = 2^{13}$ samples.

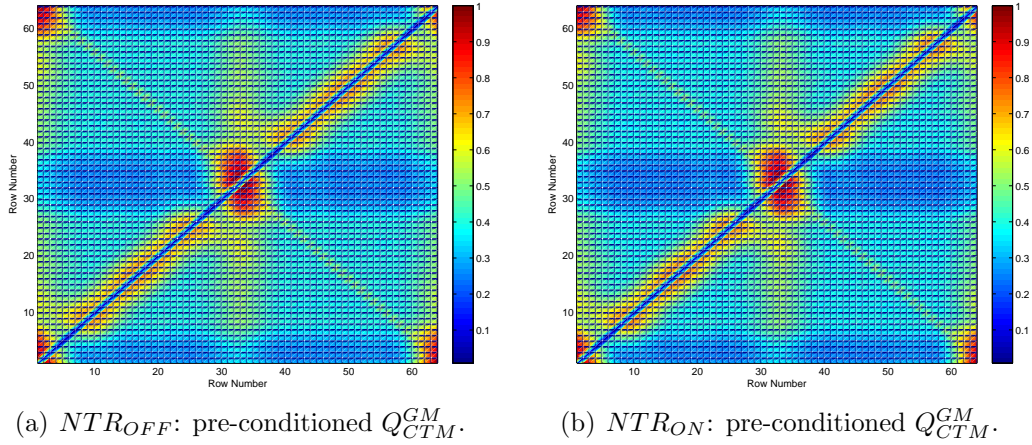
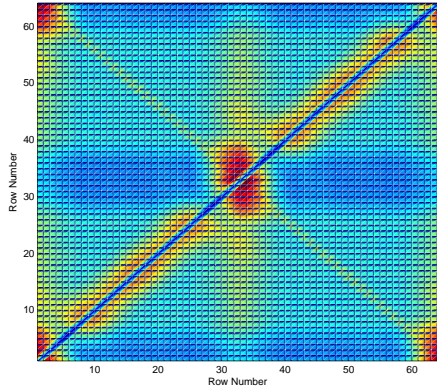


Figure 4.15: $N_Q = 2^{13}$ & $N_R = 3000$: multiple realizations of the pre-conditioned Q_{CTM}^{GM} for NTR_{OFF} (a) and NTR_{ON} (b) conditions using *Pcolor* graphical representation.

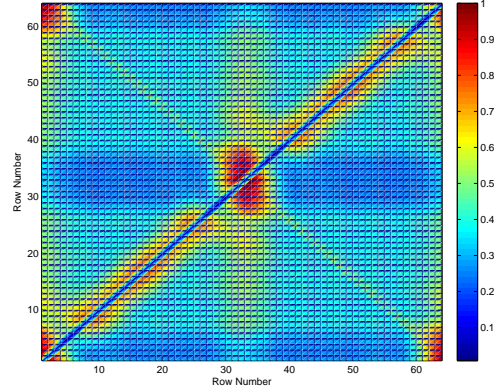
between NTR_{OFF} and NTR_{ON} conditions. The noticeable differences were in the shapes and colors, which equated to energy levels.

4.4.1.1 Configuration #1: $N_Q = 2^{13}$ Samples and $N_R = 3000$ Realizations. Among the two f_c in Figure 4.16, $f_c = 1618$ MHz was chosen because for NTR_{OFF} in Figure 4.16(c) and NTR_{ON} in Figure 4.16(d), these graphics had the most noticeable differences between the two collection conditions in the shapes and colors. In NTR_{ON} , the yellow-red ellipse on the autocorrelation line had slightly more red color when compared to NTR_{OFF} . The middle yellow-blue-green vertical ellipse on the x-axis row number 33 was darker green and had more distinct yellow areas with NTR_{ON} which appeared to have stronger color areas (more energy) compared to NTR_{OFF} .

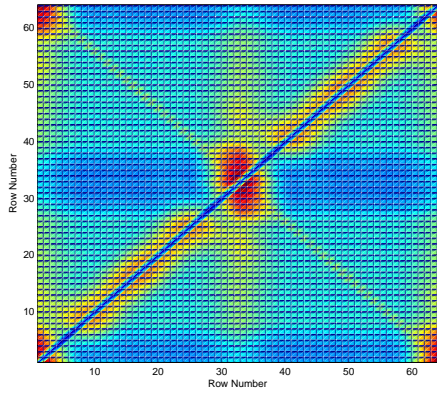
4.4.1.2 Configuration #1: $N_Q = 2^{16}$ Samples and $N_R = 600$ Realizations. Among the two f_c in Figure 4.17, $f_c = 580$ MHz was chosen because for NTR_{OFF} in Figure 4.17(a) and NTR_{ON} in Figure 4.17(b), these graphics had the most noticeable differences between the two collection conditions in the shapes and



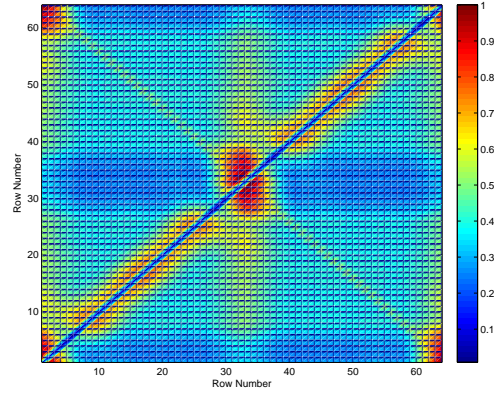
(a) NTR_{OFF} : $f_c = 580$ MHz.



(b) NTR_{ON} : $f_c = 580$ MHz.



(c) NTR_{OFF} : $f_c = 1618$ MHz.



(d) NTR_{ON} : $f_c = 1618$ MHz

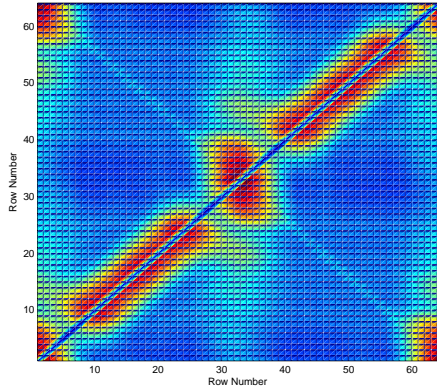
Figure 4.16: Configuration #1, NTR_{OFF} and NTR_{ON} multiple realization of the pre-conditioned Q_{CTM}^{GM} $Pcolor$ graphical representation with the settings $N_Q = 2^{13}$ samples and $N_R = 3000$ realizations for $f_c = 580, 1618$ MHz.

colors. The orange-red diagonal ellipses for NTR_{ON} had more yellow (more energy) connecting to the blue-green-yellow vertical ellipse at coordinates [33,20] and [33,45].

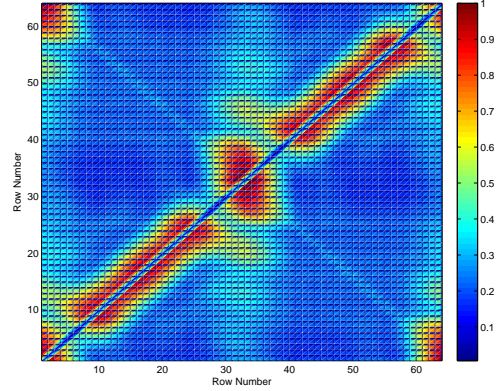
4.4.1.3 Configuration #1: $N_Q = 2^{18}$ Samples and $N_R = 210$ Realizations. Among the two f_c in Figure 4.18, $f_c = 580$ MHz was chosen because for NTR_{OFF} in Figure 4.18(a) and NTR_{ON} in Figure 4.18(b), these graphics had the most noticeable differences between the two collection conditions in the shapes and colors. The orange-red diagonal ellipses in NTR_{ON} had more yellow (more energy) connecting to the blue-green-yellow vertical ellipse at coordinates [33,20] and [33,45]. The center of NTR_{ON} had a darker red area (more energy). Also, the orange-red diagonal ellipses for NTR_{ON} was straighter on the major axis when compared with NTR_{OFF} .

4.4.1.4 Configuration #1 Summary. Comparing NTR_{OFF} and NTR_{ON} conditions, there were some subtle differences that seemed to occur in the same general response areas for all N_Q and f_c considered. The NTR_{ON} response appeared to have stronger color areas and larger color separation when compared with NTR_{OFF} , which equated to having more energy in certain locations. Overall, Figure 4.18(a) and Figure 4.18(b) for $N_Q = 2^{18}$ samples and $f_c = 580$ MHz appeared to provide the most noticeable differences between NTR_{OFF} and NTR_{ON} conditions.

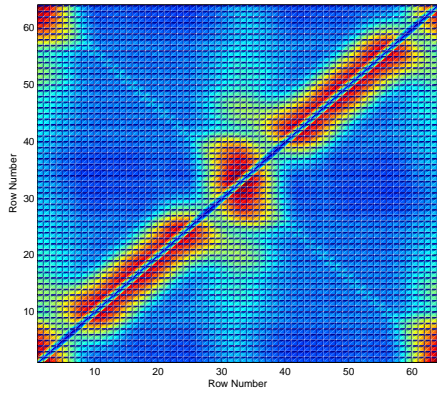
4.4.2 Configuration #2: Direct NTR Tx Output. Results here are for Configuration #2 as detailed in Section 3.4.1 and depicted in Figure 3.5. The effect of three NTR N_Q sample sizes were analyzed for the three f_c . Then, the “best” overall N_Q and f_c scenario were selected because these values extracted the most signal characteristics and highlighted distinct differences between NTR_{OFF} and NTR_{ON} conditions from Configuration #2.



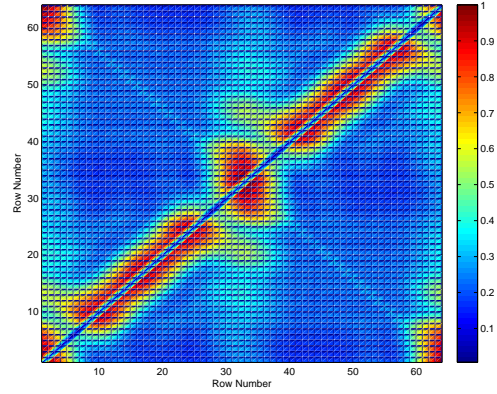
(a) NTR_{OFF} : $f_c = 580$ MHz.



(b) NTR_{ON} : $f_c = 580$ MHz.

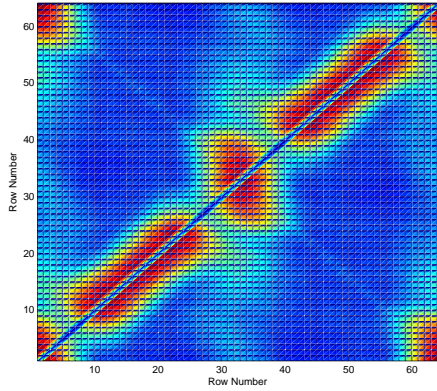


(c) NTR_{OFF} : $f_c = 1618$ MHz.

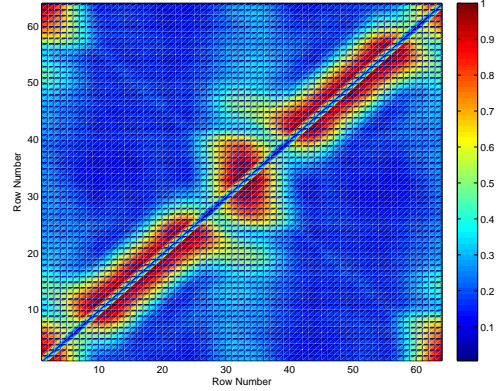


(d) NTR_{ON} and $f_c = 1618$ MHz

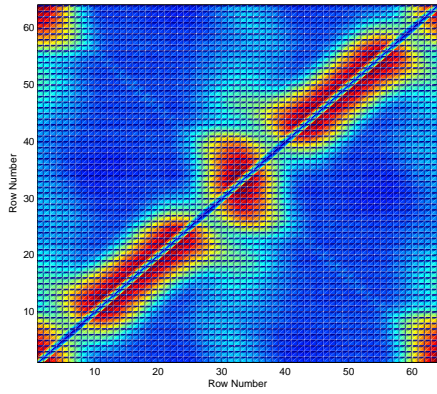
Figure 4.17: Configuration #1, NTR_{OFF} and NTR_{ON} multiple realization of the pre-conditioned Q_{CTM}^{GM} $Pcolor$ graphical representation with the settings $N_Q = 2^{16}$ samples and $N_R = 600$ realizations for $f_c = 580, 1618$ MHz.



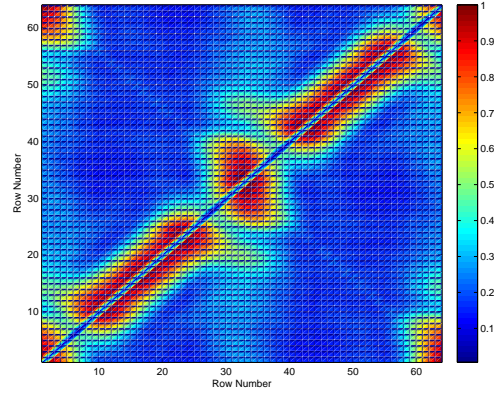
(a) NTR_{OFF} : $f_c = 580$ MHz.



(b) NTR_{ON} : $f_c = 580$ MHz.



(c) NTR_{OFF} : $f_c = 1618$ MHz.



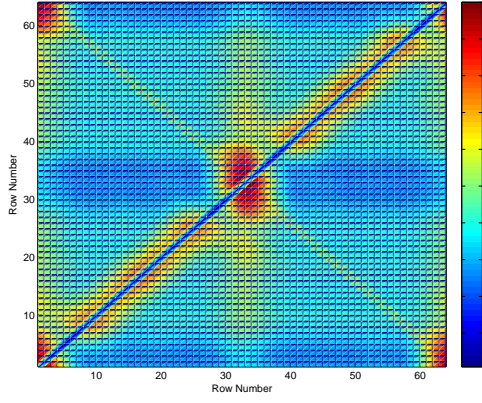
(d) NTR_{ON} and $f_c = 1618$ MHz

Figure 4.18: Configuration #1, NTR_{OFF} and NTR_{ON} multiple realization of the pre-conditioned Q_{CTM}^{GM} $Pcolor$ graphical representation with the settings $N_Q = 2^{18}$ samples and $N_R = 210$ realizations for $f_c = 580, 1618$ MHz.

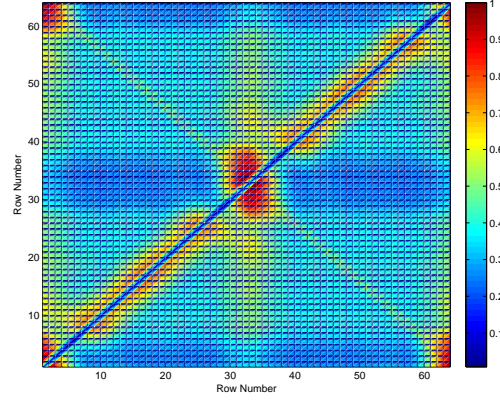
The *multiple realization* of the pre-conditioned Q_{CTM}^{GM} for Configuration #2 are graphically-illustrated as *Pcolor* in Section 4.4.2.1, Section 4.4.2.2, and Section 4.4.2.3. These graphics were based on using three different N_Q for $f_c = 373$ MHz, $f_c = 581$ MHz, and $f_c = 800$ MHz. When comparing the performance for different N_Q and f_c values and for NTR_{OFF} / NTR_{ON} conditions, the differences appeared minute and it was very difficult to visually discern between the three. However, one particular N_Q and f_c scenario visually appeared to have a slightly more discernible difference between NTR_{OFF} and NTR_{ON} conditions. The noticeable differences were in the shapes and colors, which equated to energy levels.

4.4.2.1 Configuration #2: $N_Q = 2^{13}$ Samples and $N_R = 3000$ Realizations. Among the three f_c in Figure 4.19, $f_c = 581$ MHz was chosen because for NTR_{OFF} in Figure 4.19(c) and NTR_{ON} in Figure 4.19(d), these graphics had the most noticeable differences between the two collection conditions in the shapes and colors. In NTR_{ON} , the yellow-red ellipse on the autocorrelation line had slightly more red color (more energy) when compared to NTR_{OFF} . The middle yellow-blue-green vertical ellipse on the x-axis row number 33 was darker (less energy) in the NTR_{ON} . The yellow diagonal shape in NTR_{ON} had more yellow (more energy) connections to the green vertical shape and to the vertical walls.

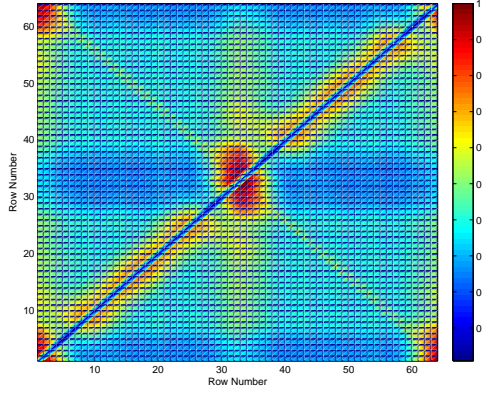
4.4.2.2 Configuration #2: $N_Q = 2^{16}$ Samples and $N_R = 600$ Realizations. Among the three f_c in Figure 4.20, $f_c = 373$ MHz was chosen because for NTR_{OFF} in Figure 4.20(a) and NTR_{ON} in Figure 4.20(b), these graphics had the most noticeable differences between the two collection conditions in the shapes and colors. In the middle light blue-green-yellow vertical ellipse on the x-axis row number 33, the green area was more separated with stronger green-yellow areas (more energy) in the NTR_{ON} than NTR_{OFF} . The orange-red diagonal ellipses in NTR_{ON} had more yellow (more energy) connecting to the blue-green-yellow vertical ellipse in



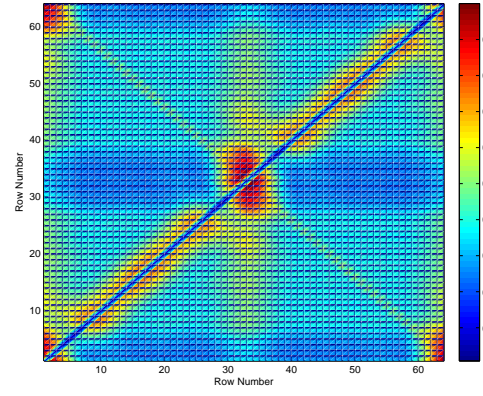
(a) NTR_{OFF} : $f_c = 373$ MHz.



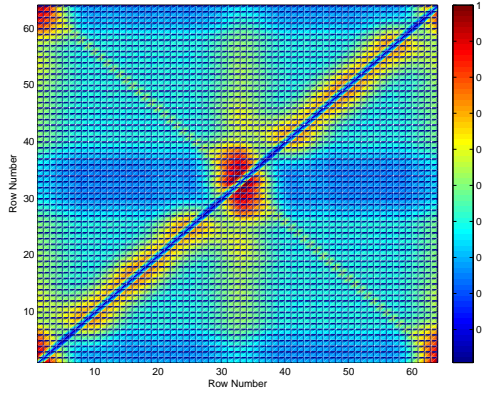
(b) NTR_{ON} : $f_c = 373$ MHz.



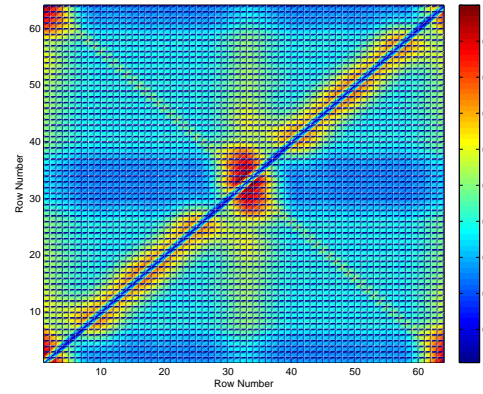
(c) NTR_{OFF} : $f_c = 581$ MHz.



(d) NTR_{ON} : $f_c = 581$ MHz.



(e) NTR_{OFF} : $f_c = 800$ MHz.



(f) NTR_{ON} : $f_c = 800$ MHz.

Figure 4.19: Config. #2, NTR_{OFF} & NTR_{ON} multi-realization of the pre-conditioned Q_{CTM}^{GM} $Pcolor$ graphics with the settings $N_Q = 2^{13}$ samples and $N_R = 3000$ realizations.

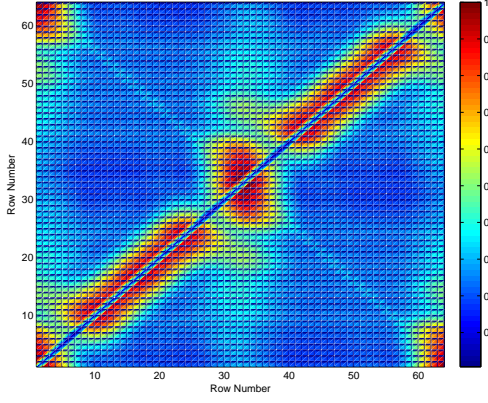
coordinates [33,20] and [33,45]. In NTR_{OFF} , the orange-red diagonal ellipses seemed to be more straight, whereas NTR_{ON} had more curves.

4.4.2.3 Configuration #2: $N_Q = 2^{18}$ Samples and $N_R = 210$ Realizations. Among the three f_c in Figure 4.21, $f_c = 373$ MHz was chosen because for NTR_{OFF} in Figure 4.21(a) and NTR_{ON} in Figure 4.21(b), these graphics had the most noticeable differences between the two collection conditions in the shapes and colors. The orange-red diagonal ellipses in NTR_{ON} had more yellow (more energy) connecting to the blue-green-yellow vertical ellipse in coordinates [33,20] and [33,45]. Also, in the three orange-red ellipse on the diagonal axis for NTR_{ON} , there were multiple darker red areas (more energy).

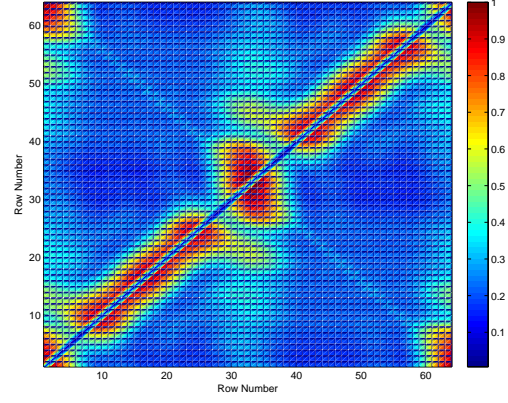
4.4.2.4 Configuration #2 Summary. Comparing NTR_{OFF} and NTR_{ON} conditions, there were some subtle differences that seemed to occur in the same general response areas for all N_Q and f_c considered. The NTR_{ON} response appeared to have stronger color areas and larger color separation when compared with NTR_{OFF} , which equated to having more energy in certain locations. Overall, Figure 4.21(a) and Figure 4.21(b) for $N_Q = 2^{18}$ samples and $f_c = 373$ MHz appeared to provide the most noticeable differences between NTR_{OFF} and NTR_{ON} conditions.

4.4.3 Configuration #3: Over Air Tx/Rx. Results here are for Configuration #3 as detailed in Section 3.4.3 and depicted in Figure 3.6. The effect of three NTR N_Q sample sizes were analyzed for the three f_c . Then, the “best” overall N_Q and f_c scenario were selected because these values extracted the most signal characteristics and highlighted distinct differences between NTR_{OFF} and NTR_{ON} conditions from Configuration #3.

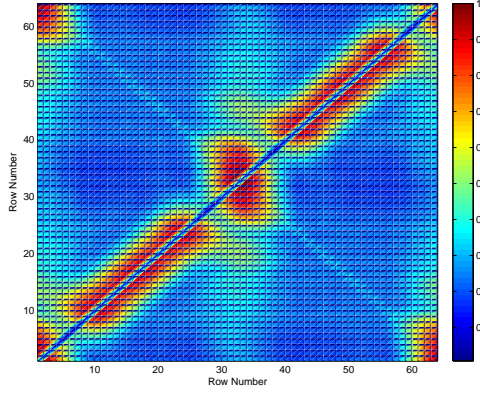
The *multiple realization* of the pre-conditioned Q_{CTM}^{GM} for Configuration #3 are graphically-illustrated as $Pcolor$ in Section 4.4.3.1, Section 4.4.3.2, and Section 4.4.3.3. These graphics were based on using three different N_Q for $f_c = 497$ MHz,



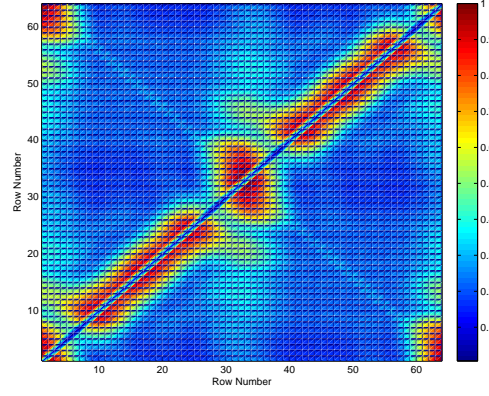
(a) NTR_{OFF} : $f_c = 373$ MHz.



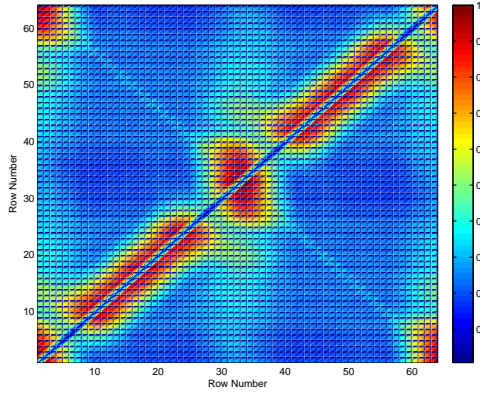
(b) NTR_{ON} : $f_c = 373$ MHz.



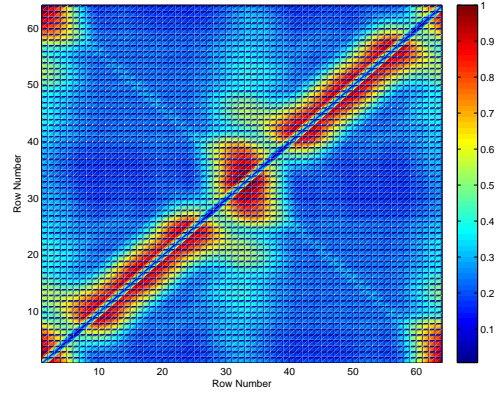
(c) NTR_{OFF} : $f_c = 581$ MHz.



(d) NTR_{ON} : $f_c = 581$ MHz.

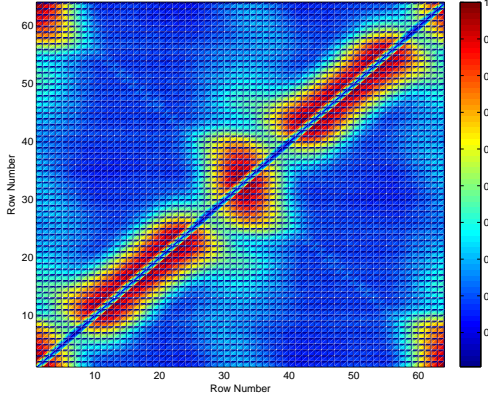


(e) NTR_{OFF} : $f_c = 800$ MHz.

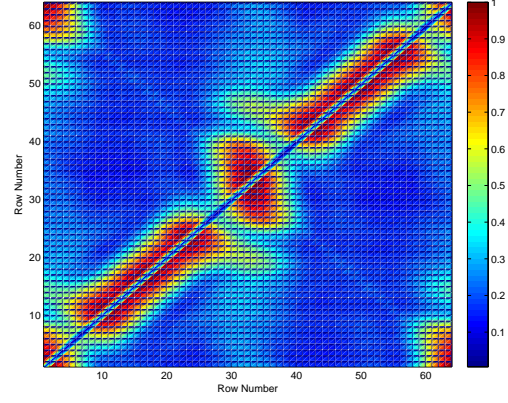


(f) NTR_{ON} and $f_c = 800$ MHz

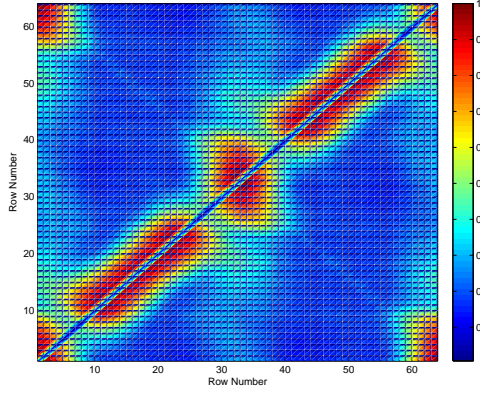
Figure 4.20: Config. #2, NTR_{OFF} & NTR_{ON} multi-realization of the pre-conditioned Q_{CTM}^{GM} $Pcolor$ graphics with the settings $N_Q = 2^{16}$ samples and $N_R = 600$ realizations.



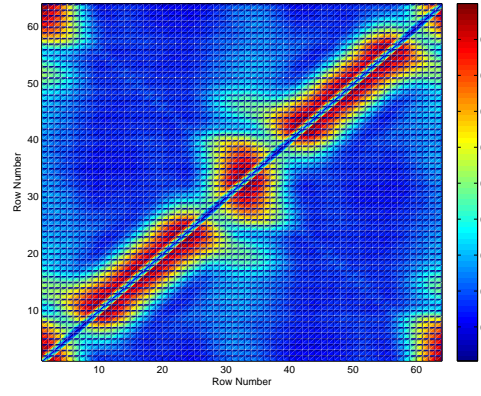
(a) NTR_{OFF} : $f_c = 373$ MHz.



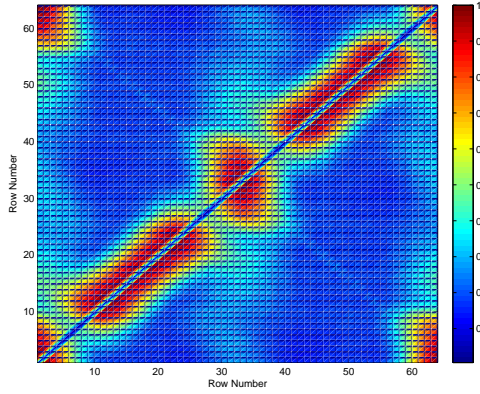
(b) NTR_{ON} : $f_c = 373$ MHz.



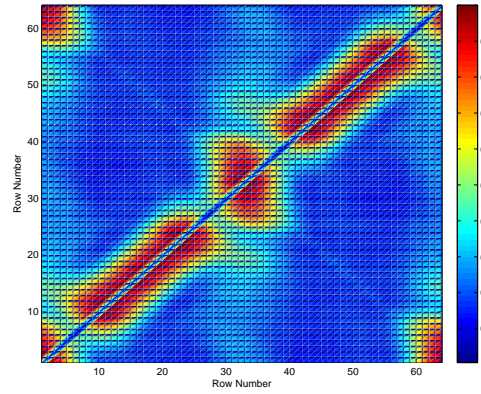
(c) NTR_{OFF} : $f_c = 581$ MHz.



(d) NTR_{ON} : $f_c = 581$ MHz.



(e) NTR_{OFF} : $f_c = 800$ MHz.



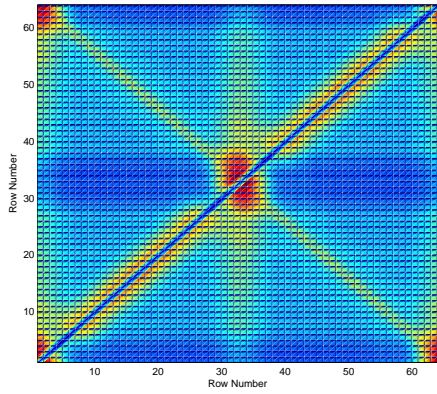
(f) NTR_{ON} : $f_c = 800$ MHz.

Figure 4.21: Config. #2, NTR_{OFF} & NTR_{ON} multi-realization of the pre-conditioned Q_{CTM}^{GM} $Pcolor$ graphics with the settings $N_Q = 2^{18}$ samples and $N_R = 2100$ realizations.

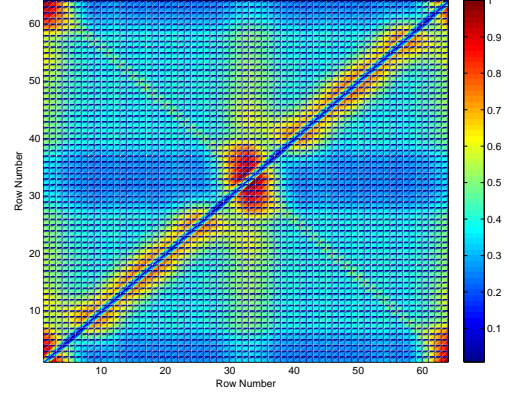
$f_c = 686$ MHz, and $f_c = 797$ MHz. When comparing performance for different N_Q and f_c values and for NTR_{OFF} / NTR_{ON} conditions, the differences appeared minute and it was very difficult to visually discern between the three. However, one particular N_Q and f_c scenario visually appeared to have a slightly more discernible difference between NTR_{OFF} and NTR_{ON} conditions. The noticeable differences were in the shapes and colors, which equated to energy levels.

4.4.3.1 Configuration #3: $N_Q = 2^{13}$ Samples and $N_R = 3000$ Realizations. Among the three f_c , $f_c = 686$ MHz was chosen because for NTR_{OFF} in Figure 4.22(c) and NTR_{ON} in Figure 4.22(d), these graphics had the most noticeable differences between the two collection conditions in the shapes and colors. In NTR_{OFF} , the yellow-red ellipse on the diagonal line was slightly more elongated and straight when compared to NTR_{ON} , where it had some defining features. The middle yellow-blue-green vertical ellipse on the x-axis row number 33 had a yellow line in the NTR_{OFF} . Finally, the center, red ellipse was larger (more energy) with a distinct shape for NTR_{ON} .

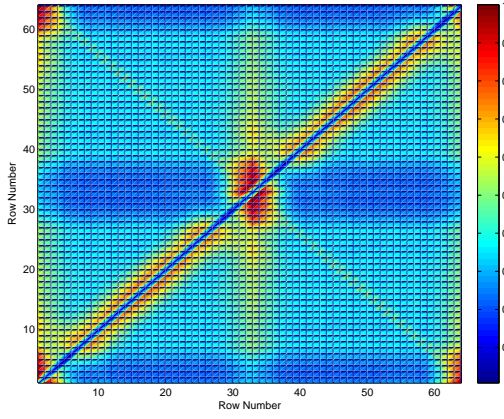
4.4.3.2 Configuration #3: $N_Q = 2^{16}$ Samples and $N_R = 600$ Realizations. Among the three f_c , $f_c = 686$ MHz was chosen because for NTR_{OFF} in Figure 4.23(c) and NTR_{ON} in Figure 4.23(d), these graphics had the most noticeable differences between the two collection conditions in the shapes and colors. In NTR_{OFF} , the yellow-red ellipse on the diagonal line was slightly more elongated and straight when compared to NTR_{ON} , where it had some defining features. The middle yellow-blue-green vertical ellipse on the x-axis row number 33 was divided into green areas in NTR_{ON} compared to NTR_{OFF} , where it was a large green-blue area. The yellow-red diagonal shape in NTR_{ON} had more yellow (more energy) connections to the green vertical shape on the x-axis row number 33. Finally, the center, red ellipse was larger (more energy) with a distinct shape for NTR_{ON} .



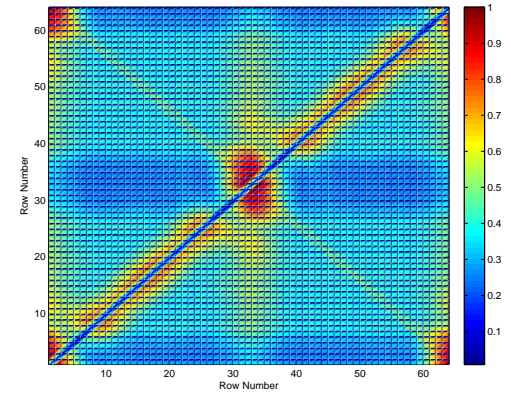
(a) NTR_{OFF} : $f_c = 497$ MHz.



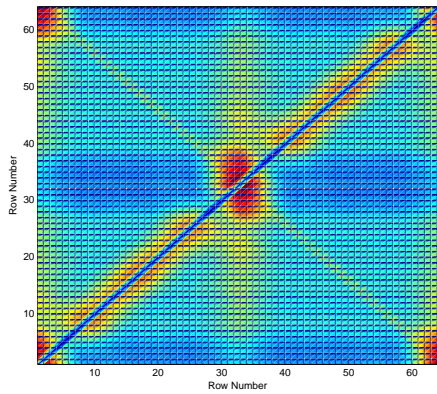
(b) NTR_{ON} : $f_c = 497$ MHz.



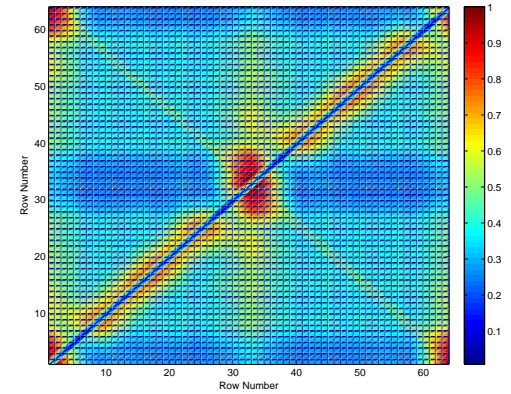
(c) NTR_{OFF} : $f_c = 686$ MHz.



(d) NTR_{ON} : $f_c = 686$ MHz.

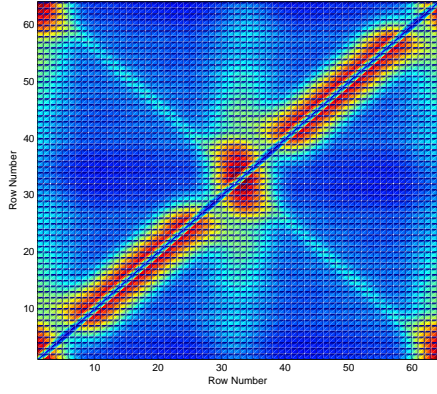


(e) NTR_{OFF} : $f_c = 797$ MHz.

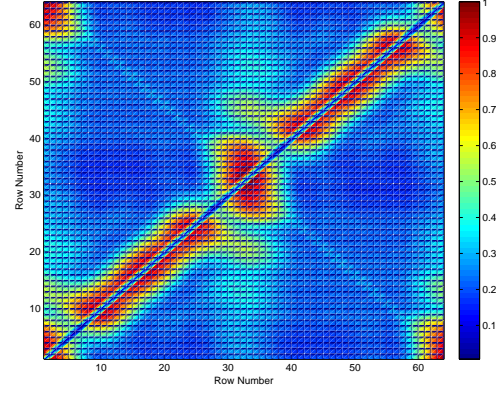


(f) NTR_{ON} : $f_c = 797$ MHz.

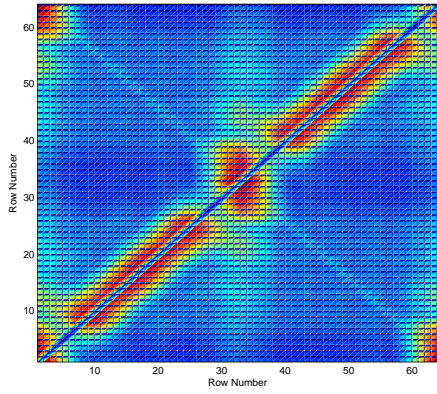
Figure 4.22: Config. #3, NTR_{OFF} & NTR_{ON} multi-realization of the pre-conditioned Q_{CTM}^{GM} $Pcolor$ graphics with the settings $N_Q = 2^{13}$ samples and $N_R = 3000$ realizations.



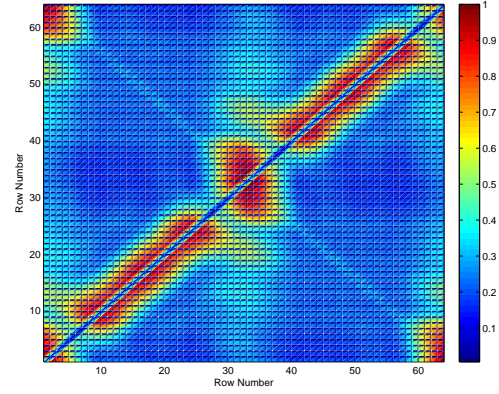
(a) NTR_{OFF} : $f_c = 497$ MHz.



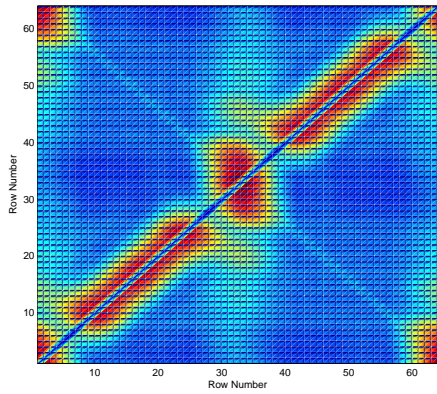
(b) NTR_{ON} : $f_c = 497$ MHz.



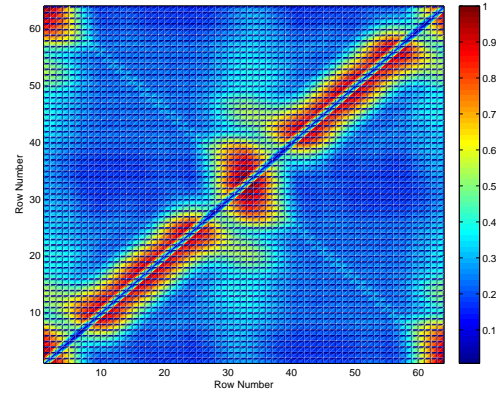
(c) NTR_{OFF} : $f_c = 686$ MHz.



(d) NTR_{ON} : $f_c = 686$ MHz.



(e) NTR_{OFF} : $f_c = 797$ MHz.



(f) NTR_{ON} : $f_c = 797$ MHz.

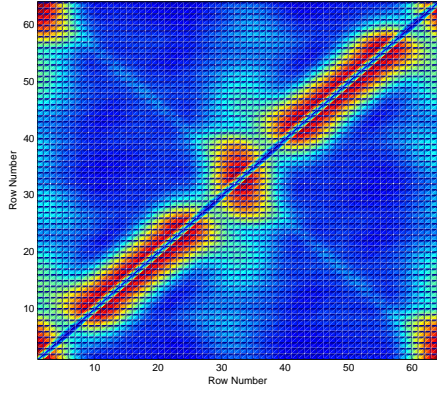
Figure 4.23: Config. #3, NTR_{OFF} & NTR_{ON} multi-realization of the pre-conditioned Q_{CTM}^{GM} $Pcolor$ graphics with the settings $N_Q = 2^{16}$ samples and $N_R = 600$ realizations.

4.4.3.3 *Configuration #3: $N_Q = 2^{18}$ Samples and $N_R = 210$ Realizations.* Among the three f_c , $f_c = 497$ MHz was chosen because for NTR_{OFF} in Figure 4.24(a) and NTR_{ON} in Figure 4.24(b), these graphics had the most noticeable differences between the two collection conditions in the shapes and colors. In NTR_{OFF} , the yellow-red ellipse on the diagonal line was slightly more elongated and straight when compared to NTR_{ON} , where it had some defining features. The yellow-red diagonal shape in NTR_{ON} had more yellow (more energy) connections to the green vertical shape on the x-axis row number 33. Finally, the center, red ellipse was larger (more energy) with a distinct shape for NTR_{ON} .

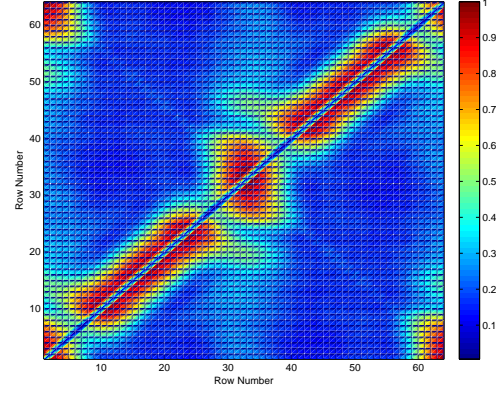
4.4.3.4 *Configuration #3 Summary.* Comparing NTR_{OFF} and NTR_{ON} conditions, there were some subtle differences that seemed to occur in the same general response areas for all N_Q and f_c considered. The NTR_{ON} response appeared to have stronger color areas and larger color separation when compared with NTR_{OFF} , which equated to having more energy in certain locations. Overall, Figure 4.24(a) and Figure 4.24(b) for $N_Q = 2^{18}$ samples and $f_c = 497$ MHz appeared to provide the most noticeable differences between NTR_{OFF} and NTR_{ON} conditions.

4.5 Near-Term Research Opportunities

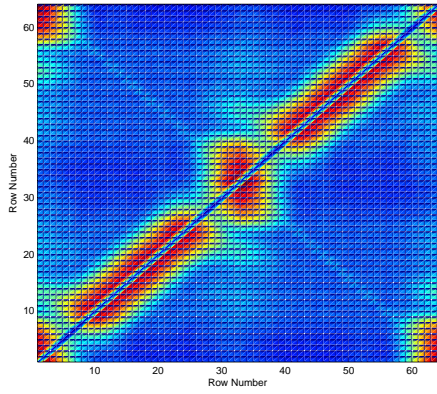
4.5.1 *Spectral Scalloping.* The NTR signal spectrum in Figure 3.3 exhibits spectral scalloping characteristics similar to what occurs when taking the FFT of a truncated signal [20]. For the NTR signal considered here, this is potentially the result of 1) the NTR signal inherently possessing such characteristics, 2) the WB scanning of a NB filter in the RFSICS, or 3) a combination thereof. For an initial “Quick-look” assessment into the cause of spectral scalloping, the RFSICS was used with NTR Configuration #2 as a fixed, non-scanning NB receiver with the ADC dynamic range fixed and the bandwidth set to $W_c = 5$ MHz. This NB filter was sequentially centered at eleven specific frequencies that corresponded with peak and null responses in the NTR signal response in Figure 3.3. The resultant



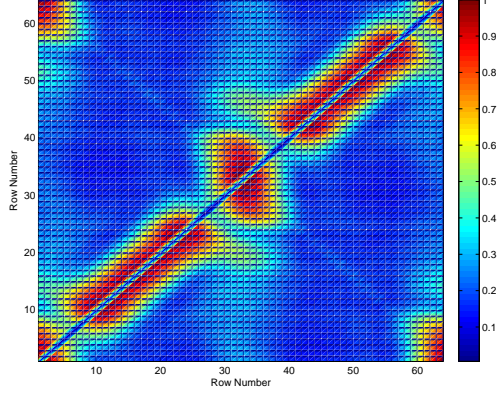
(a) NTR_{OFF} : $f_c = 497$ MHz.



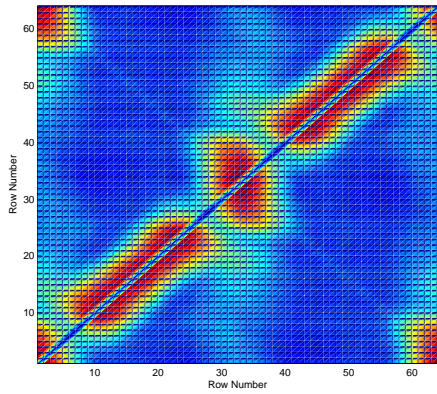
(b) NTR_{ON} : $f_c = 497$ MHz.



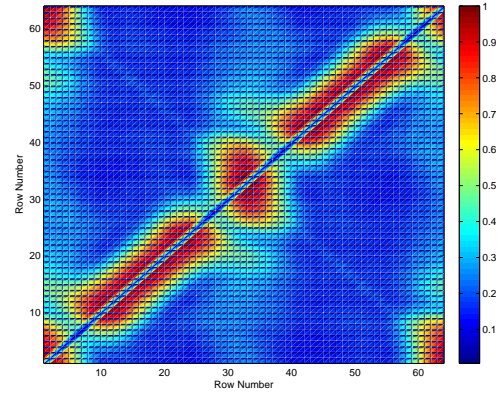
(c) NTR_{OFF} : $f_c = 686$ MHz.



(d) NTR_{ON} : $f_c = 686$ MHz.



(e) NTR_{OFF} : $f_c = 797$ MHz.



(f) NTR_{ON} : $f_c = 797$ MHz.

Figure 4.24: Config. #3, NTR_{OFF} & NTR_{ON} multi-realization of the pre-conditioned Q_{CTM}^{GM} $Pcolor$ graphics with the settings $N_Q = 2^{18}$ samples and $N_R = 210$ realizations.

collected data was averaged, normalized, and its power compared to the NTR signal spectrum. The results of mapping these eleven power values to the NTR signal response is shown in Figure 4.25. As indicated, the resultant high and low power responses are relatively consistent with the NTR PSD responses at each of the eleven frequencies considered. This suggests that the scalloping inherently exists in the NTR signal. However, this preliminary finding requires additional investigation as system calibration was not performed for this initial assessment. Given that this research focused on NTR assessment using non-scanning, NB RFSICS collections, the effects of spectral scalloping on the final results in previous sections should be non-existent.

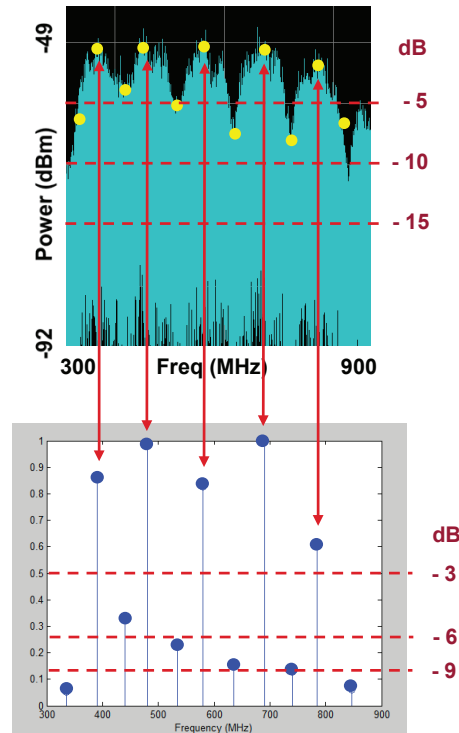


Figure 4.25: Top graphic is a WB RFSICS snapshot of Configuration #2 mapped to the bottom graphic which is the processed collection.

4.5.2 Synthesized Bi-Phase Coding. The effectiveness of G-M process with a synthesized bi-phase coded NTR signal was assessed using the resulting detection process and Q_{CTM}^{GM} from Section 4.2.2. The synthesized bi-phase coded NTR signal was generated using the process shown in Figure 4.26. To enable direct comparison between uncoded NTR and synthesized bi-phase coded NTR detectability, the collected $\{R(k)\}$ that was used to generate uncoded NTR_{ON} results in Figure 4.7(a) of Section 4.2.2 was selected and bi-phase modulated per Figure 4.26. This particular $\{R(k)\}$ contained $N_S = 2^{13}$ samples. As illustrated in Figure 4.27, the periodic bi-phase coding waveform $c(t)$ was generated with $N_S = 2^{13}$ samples and contained four periods with five “chip” intervals per period. The first symbol period in Figure 4.27 is colored red, followed by three additional duplicate symbols in blue. Given that an amplitude value of ± 1 was used for $c(t)$, the bi-phase coding did not impact the signal’s energy or power characteristics. This can be seen in Figure 4.28 which illustrates the PSDs for the uncoded NTR signal (left) and the synthesized bi-phase coded NTR signal (right). Furthermore, such coding is generally undetectable using power-based or energy-based receiver processing methods.

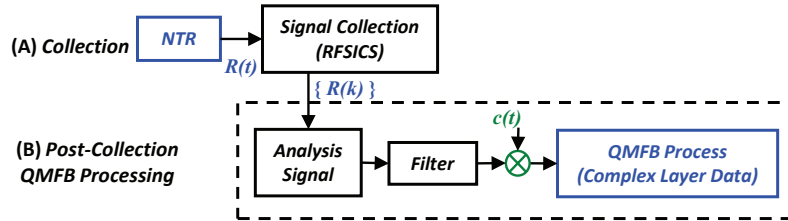


Figure 4.26: Process for synthesizing bi-phase coded NTR signals.

The synthesized bi-phase coded NTR signal was processed and analyzed using the final QMFB process presented in Section 4.2.2 using collected data from Configuration #2 with $N_Q = 2^{13}$ samples and $N_R = 1$ realization. The resulting *non-transformed* QMFB, Q_6 , contour graphic for the bi-phase coded signal is presented in Figure 4.29 and possesses virtually no distinguishing features that can be associated with the phase-code characteristics in Figure 4.27. Relative to uncoded NTR_{ON} results presented previously in Figure 4.7(a) of Section 4.2.2, there are no

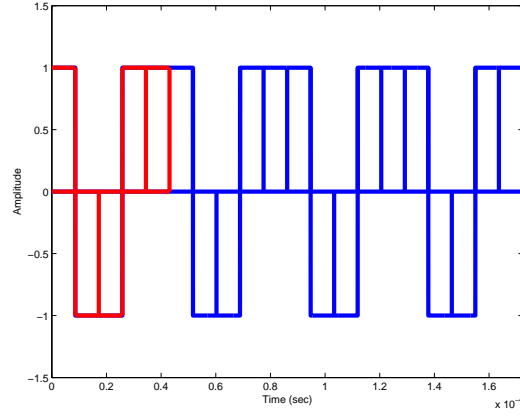


Figure 4.27: Coding waveform $c(t)$ used for generating the synthesized bi-phase coded NTR signal.

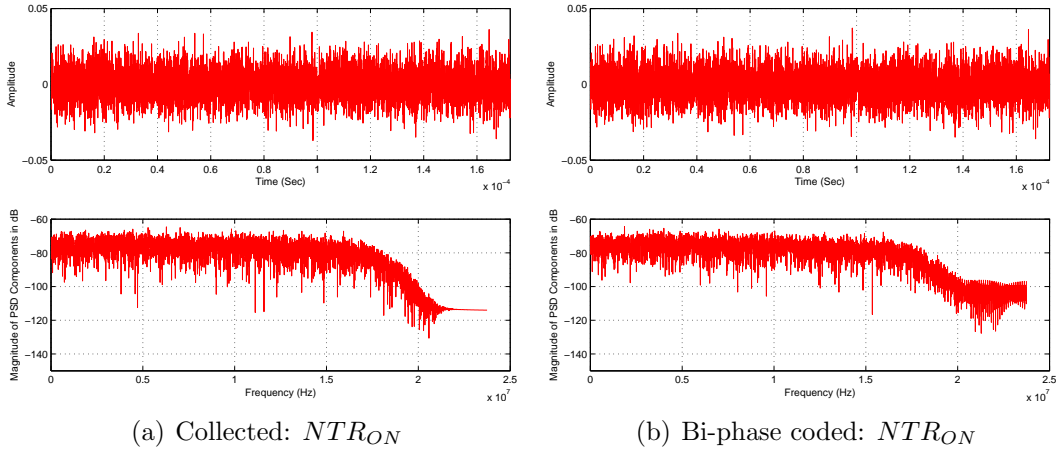


Figure 4.28: Synthesized bi-phase coded and collected NTR PSDs.

discernible difference. The same Q_6 was then *G-M transformed* to produce Q_{CTM}^{GM} per Section 4.3.1 and *Pcolor* graphics were generated which is illustrated in Figure 4.30(b). Relative to the corresponding uncoded QMFB result in Figure 4.30(a) which is provided for comparison, the G-M process produces a favorable response for the phase-coded NTR signal, i.e., there visually discernable islands of high energy concentration along the diagonal that are qualitatively attributable to the phase coding in Figure 4.27.

Performance of the G-M process with the synthesized bi-phase coded NTR signal can be viewed as either 1) a potential item of concern from the NTR development

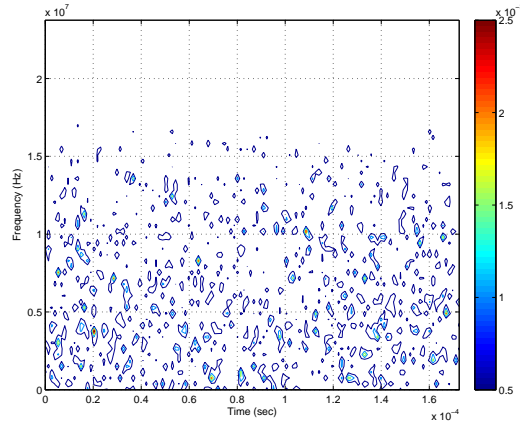


Figure 4.29: *Contour* Graphic of *Non-transformed* Q_6 synthesized bi-phase coded NTR signal and NTR_{ON} condition.

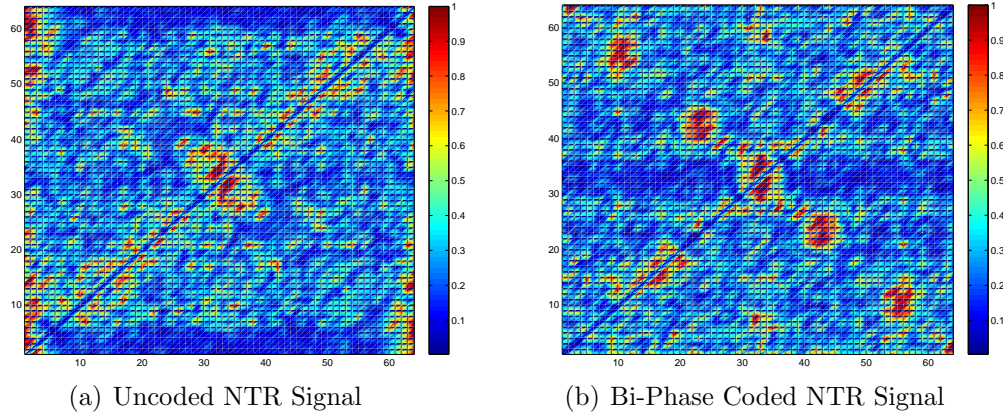


Figure 4.30: *Pcolor* graphics for *G-M transformed* (Q_{CTM}^{GM}) QMFB Q_6 for uncoded and synthesized bi-phased coded NTR signals.

perspective or 2) a potential item of promise from an NTR exploitation perspective. Regardless of the perspective taken, the “presence” aspect of NTR detectability has been demonstrated and there is near-term opportunity for continued research in this area.

Summary

This chapter provided results for the qualitative visual assessment and analysis of NTR detectability. Various configurations, center frequencies (f_c), and number of

Table 4.1: Summary of Multiple NTR Realization Results. Bold entries denote “best” combinations.

| Configuration | N_Q Samples | N_R Realizations | f_c (MHz) |
|------------------------|---------------|--------------------|-------------|
| #1 – NTR Source Output | 2^{13} | 3000 | 1618 |
| | 2^{16} | 600 | 580 |
| | 2^{18} | 210 | 580 |
| #2 – NTR Tx Output | 2^{13} | 3000 | 581 |
| | 2^{16} | 600 | 373 |
| | 2^{18} | 210 | 373 |
| #3 – Over Air Tx/Rx | 2^{13} | 3000 | 686 |
| | 2^{16} | 600 | 686 |
| | 2^{18} | 210 | 497 |

input samples to the QMFB process (N_Q) were analyzed. For collected *unstructured* NTR signals, Table 4.5.2 provides a summary of the “best” f_c and N_R scenario for each configuration in boldface text. Among all the *unstructured* NTR signals collections, the best performance was achieved using Configuration #3 (Over Air Tx/Rx) with a QMFB input sample size of $N_Q = 2^{18}$ samples and RF center frequency $f_c = 497$ MHz because of the fluctuation of the background noise and the strong NTR signal produced. While this scenario provided the most noticeable differences between NTR_{OFF} and NTR_{ON} conditions using *Pcolor* graphics, the overall discernibility was minimal, and detection remained very challenging. For synthesized *structured* NTR signals created by adding bi-phase coding to a collected NTR signal with identical configuration and collection parameters maintained, there were distinct differences between NTR_{OFF} and NTR_{ON} conditions. In this case, visually-observed features were detectable and corresponded to the induced bi-phase code features. Ultimately, the overall research objective was met in that the resultant G-M process was shown to be useful for assessing and influencing both NTR development (desire to maximize LPD/LPI potential) and NTR exploitation (desire to minimize LPD/LPI potential) activities.

V. Conclusion

This chapter summarizes the research activity and provides conclusions and recommendations for future research. This includes a summary of the research motivation, goals, techniques, and results, which are followed by a list of recommendations for near-term follow-on research activity. Supplementary appendices and the document bibliography are provided immediately thereafter.

5.1 Research Summary

The concept of noise radar was introduced circa 1950. However, its practical implementation is only now being realized in various Noise Technology Radar (NTR) systems. The reduction in computational complexity, as brought about by advances in Digital Signal Processing (DSP), has generated near-worldwide interest in NTR system development. As development continues, NTR deployment becomes more inevitable and interest within the RF Intelligence (RFINT) community heightens. Thus, the RFINT community is becoming proactive to ensure that their arsenal of RF awareness tools are up-to-date. The emergence of NTR systems will require new RFINT capabilities based on non-cooperative, non-matched filter detection techniques to exploit information in emerging signals of interest. This research provides an initial assessment of NTR signal detectability using such techniques.

The overall research objective was to assess NTR signal detectability using qualitative graphical visualization. The detection approach used a non-cooperative collection receiver and empirical pair-wise assessment of graphics obtained for NTR_{OFF} and NTR_{ON} collection conditions. The emergence of distinguishable feature characteristics and/or differences between the two conditions dictated NTR signal detectability. Relative to previous related research using *structured* signals [11,27], i.e., those containing intentional modulation features, the work here addressed *unstructured* Wideband (WB) NTR signals that are collected using a Narrowband (NB)

collection receiver. The signals of interest were collected from a typical NTR node in AFIT's Noise Network (NoNET) radar system. The NoNET system is an integrated group of NTR nodes with centralized processing for data acquisition, digital processing and multi-sensor image fusion [25, 30].

Two distinct NTR research veins are being pursued at AFIT, including: 1) NTR *developmental* work aimed at improving NTR performance from a *cooperative* radar detection perspective and 2) NTR *exploitation* work aimed at assessing NTR exploitability using *non-cooperative* detection methods—the focus of this research. The NoNET NTR node signals are low power, Continuous Wave (CW) signals that inherently possess Low Probability of Detection/Intercept (LPD/LPI) characteristics. Quadrature Mirror Filter Bank (QMFB) processing was adopted here for initial assessment of NTR signal detectability. Consistent with earlier work that effectively used QMFB processing for detecting *structured* LPD/LPI waveforms [11, 27], detectability was determined through graphical visual assessment of energy-based graphics from *non-transformed* QMFB output data. Results here for *unstructured* NTR signals revealed minimal discernability between NTR_{OFF} and NTR_{ON} conditions.

Improvement was sought using *transformed* QMFB based on previous AFIT research by Gronholz and Mims (G-M) [7, 8, 22, 23]. The G-M process was effectively used for detecting LPD/LPI Ultra Wideband (UWB) communication signals—common LPD/LPI characteristics of UWB and NTR signals suggested it was reasonable to consider G-M processing with NTR signals. Relative to *non-transformed* QMFB processing, results for *G-M transformed* QMFB process with NTR signals were mixed and included:

1. For the collected *unstructured* NTR signals, the best performance was achieved using Configuration #3 (Over Air Tx/Rx) with a QMFB input sample size of $N_Q = 2^{18}$ samples and RF center frequency $f_c = 497$ MHz because of the fluctuation of the background noise and the strong NTR signal produced. While

these conditions provided the most noticeable differences between NTR_{OFF} and NTR_{ON} conditions using Pcolor graphics, the overall discernibility was minimal and detection remained very challenging,

2. For synthesized *structured* NTR signals created by adding bi-phase coding to collected signals in 1 above, with identical configuration and collection parameters maintained, there were distinct differences between NTR_{OFF} and NTR_{ON} conditions. In this case, visually observed features were detectable and corresponded to the induced bi-phase code features.

The overall research objective was met in that the resultant *G-M transformed* QMFB process was shown to be useful for assessing and influencing both NTR development (desire to maximize LPD/LPI potential) and NTR exploitation (desire to minimize LPD/LPI potential) activities.

5.2 Recommendation for Future Research

This section provides recommendations for near-term research opportunities that exist as a result of this research. As demonstrated herein, NTR signal detectability poses a significant technical challenge and there are several areas that could be expanded upon. Ultimately, the goal of subsequent research would be to develop methods for improving NTR detectability by revealing or highlighting more substantial differences between NTR_{OFF} and NTR_{ON} conditions. This is particularly required when considering *unstructured* NTR signal cases. Subsequent research activity could include:

1. Quantitative Statistical vs. Qualitative Assessment

While graphical visual assessment is useful when considering system implementations having an operator interface, the transition to automated detection systems would generally require quantitative measures to characterize various “states” being observed by the system, i.e., NTR_{OFF} and NTR_{ON} conditions.

Such measures could be provided through statistical characteristic differences that may exist between the various states considered.

2. *Alternate Parameter Selection and Variational Analysis*

As noted in Section 3.8, results and conclusions here are based on a very small subset of the vast number of available parametric combinations. Additional and/or alternate combinations of the parameters considered here may produce better features that are more readily apparent when graphically assessed. Some of the obvious variations to the research presented here include using a different: non-transformed Q_n layer; collection signal sample size (N_S); input QMFB sample size (N_Q); collection receiver instantaneous bandwidth ($W_{RF} \leq 36$ MHz available using the RFSICS); collection center frequencies (f_c) that span the full NTR bandwidth (W_{NTR}) using either contiguous non-overlapping NB collections or non-contiguous overlapping NB collections.

3. *Alternate Collection Receiver Architectures*

Alternate receiver architectures include those having a wider maximum instantaneous bandwidth than the RFSICS ($W_{RF} = 36$ MHz). Using $W_{RF} = 100$ MHz, $W_{RF} = 200$ MHz, ... , would enable collection and processing of the full NTR bandwidth (NoNet $W_{NTR} \approx 400$ MHz) using either fewer sequential collections or a single collection capturing the entire signal if $W_{RF} = W_{NTR}$ is available. In either case, the instantaneous collection of larger segments of W_{NTR} may be more effective for capturing inherent Time-Frequency (T-F) variation that is not present in shorter duration, narrower bandwidth collections.

4. *Revisiting Spectral Scalping*

As discussed in Section 4.5.1, the preliminary power assessment showed that the observed spectral Scalping appears to be inherent in NTR Waveform. Once reconfirmed that this is indeed the case, subsequent research could consider spectral scalping features (minimum null / maximum lobe spacing, rel-

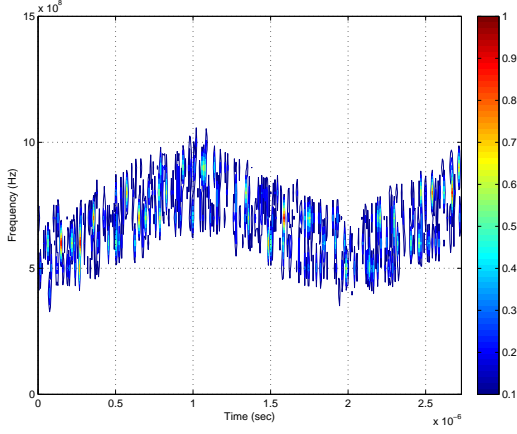
ative min-max levels, variation across multiple collections, etc.) as potentially exploitable for characterizing NTR signals.

5. *Modulated NTR Signal Analysis*

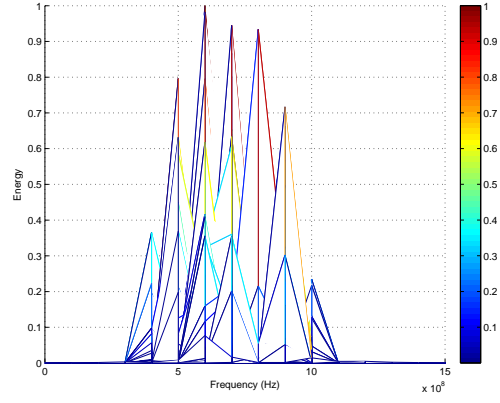
NTR signal modulation has been used to improve various aspects of NTR performance. There is pending future research at AFIT that includes adding some form of modulation to NoNet NTR nodes to improve Doppler resolution. Thus, there may be an opportunity at AFIT to assess detectable *structured* NTR signals. Preliminary results in Section 4.5.2 for the synthesized NTR signal with bi-phase coding suggests that *G-M transformed* QMFB processing may be well-suited for this task.

Appendix A. Additional FMCW Non-Transformed QMFB Figures

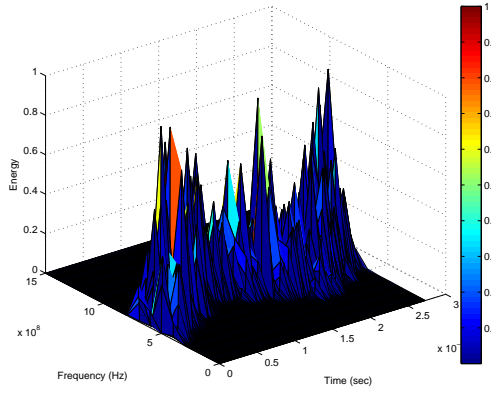
$Q_5, Q_6, Q_7,$ and Q_8



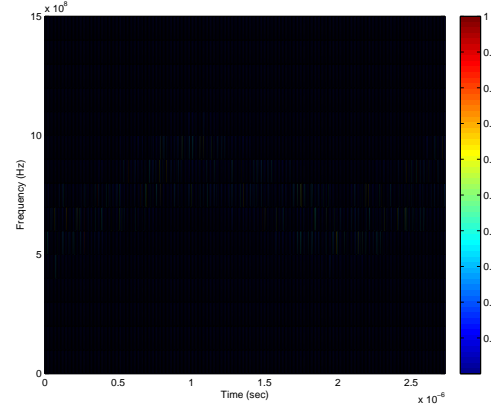
(a) Q_4 Contour Graphic.



(b) Q_4 Mesh Graphic.

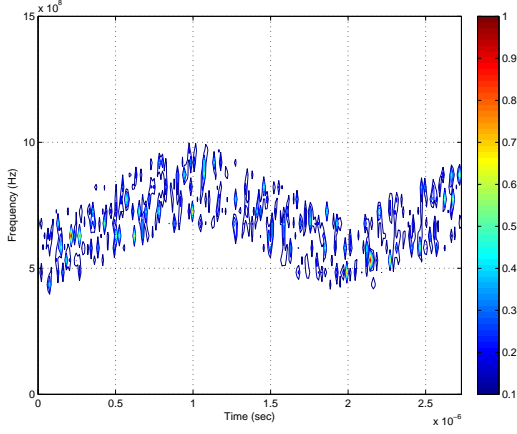


(c) Q_4 Surface Graphic.

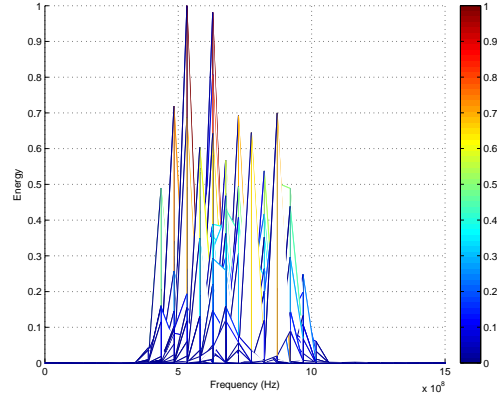


(d) Q_4 Pcolor Graphic.

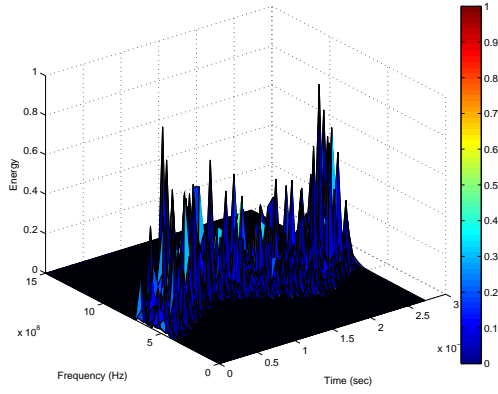
Figure 1: Four graphical representation (as indicated) of the *Non-Transformed* QMFB (Q_4) for Layer #4 NTR_{ON} condition using $N_Q = 2^{13}$ samples.



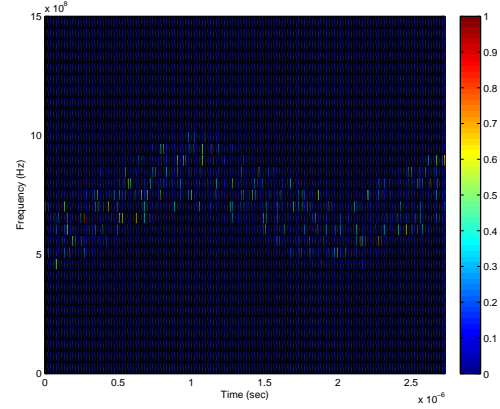
(a) Q_5 Contour Graphic.



(b) Q_5 Mesh Graphic.

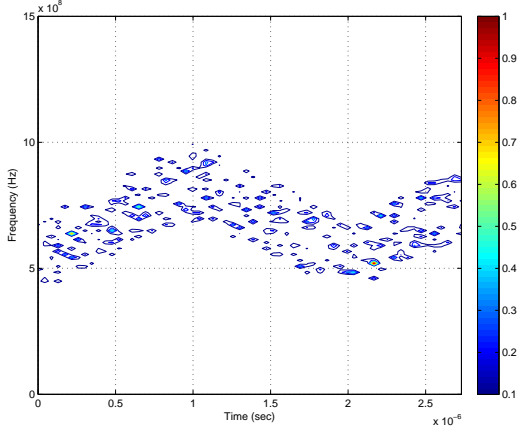


(c) Q_5 Surface Graphic.

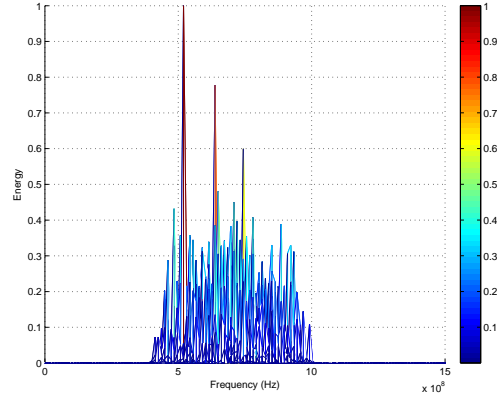


(d) Q_5 Pcolor Graphic.

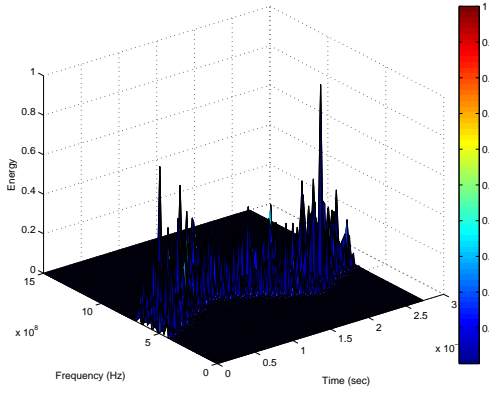
Figure 2: Four graphical representation (as indicated) of the *Non-Transformed* QMFB (Q_5) for Layer #5 NTR_{ON} condition using $N_Q = 2^{13}$ samples.



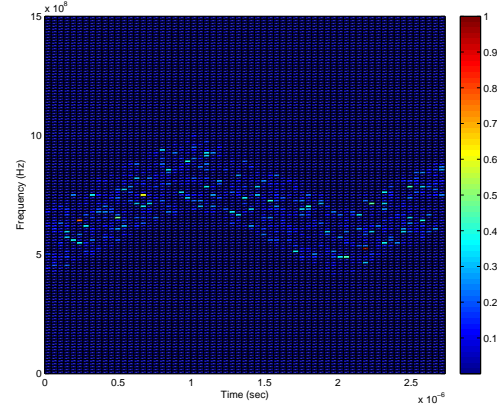
(a) Q_7 Contour Graphic.



(b) Q_7 Mesh Graphic.

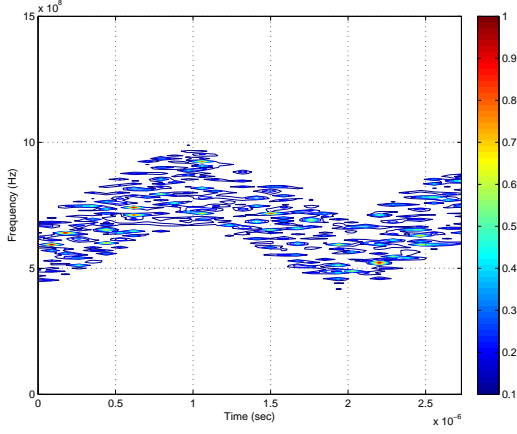


(c) Q_7 Surface Graphic.

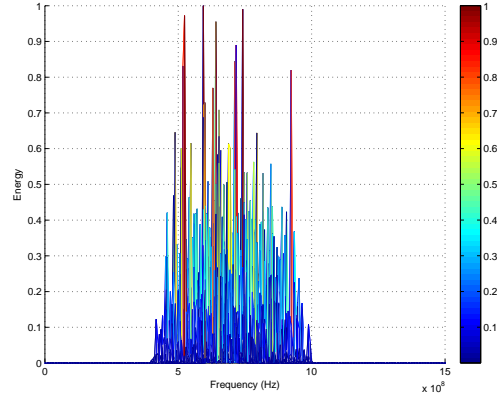


(d) Q_7 Pcolor Graphic.

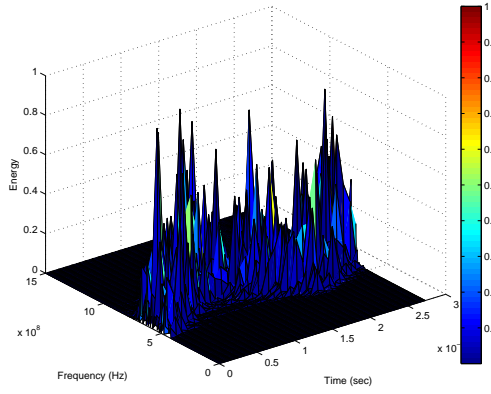
Figure 3: Four graphical representation (as indicated) of the *Non-Transformed* QMFB (Q_7) for Layer #7 NTR_{ON} condition using $N_Q = 2^{13}$ samples.



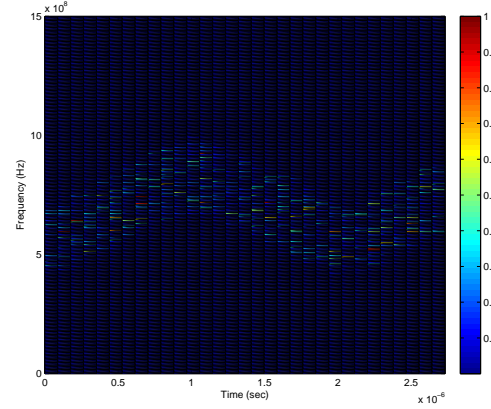
(a) Q_8 Contour Graphic.



(b) Q_8 Mesh Graphic.



(c) Q_8 Surface Graphic.



(d) Q_8 Pcolor Graphic.

Figure 4: Four graphical representation (as indicated) of the *Non-Transformed* QMFB (Q_8) for Layer #8 NTR_{ON} condition using $N_Q = 2^{13}$ samples.

Appendix B. MATLAB[®] Code

The appendix provides the main MATLAB[®] files used to functionally implement the QMFB and G-M process as described in Chapter III and used in Chapter IV.

B.1 QMFB Process

Listing B.1: Code/QMFB.m

```
1 % Originally startpoint.m by Dr.Pace
  % Modified by:
  % Daniel V. Atienza          EENG 799 -- Fall 2009
  %%%%%%%%%%%%%%%%%%%%%%%%%%%%%%%%%%%%%%%%%%%%%%%%%%%%%%%%%%%%%%%%%%%%%%%%%
  % name = name of orginal or parse file in quotes
6 % Tx = 0(off) or 1(on)
  % Dlayer = desired layer to be analyze for FreqConstant
  %          0 for all layers
  %%%%%%%%%%%%%%%%%%%%%%%%%%%%%%%%%%%%%%%%%%%%%%%%%%%%%%%%%%%%%%%%%%%%%%%%%

11 function ProduceLayers_v2(name,Tx,Dlayer)
  % clear all; clc; close all;

  format compact
  file=name;
16 [I Q fs] = convertYtoIQ(file);
  %-----
  % -- Ensures I & Q are in Column Format --
  [v,u]=size(I); % Since the QMFBT work with incoming signals as
                  % columns, this step is to transform the
21                  % incoming signal to a column vector if its a
                  % row vector

  if v==1
      I=I'; % This apply if the incoming signal is a row vector
      Q=Q'; % This apply if the incoming signal is a row vector
26 end
```

```

%-----
% -- Formatting the Signal --
%
T=1/fs;          % Period of the signal
31 signal=I+j*Q;  % Forming the signal

% disp('Length of signal');
L=length(signal); % Length of the signal
% disp('Number of Layers');
36 Lc=ceil(log2(L)); % It will give the number of layers.
% disp('Number of zeros in padding');
z=((2.^Lc) - L); % In the case that the signal length does not
                % correspond to a power of two the signal
                % will be padded with zeros until the next
41                % power of 2 (2^(number of layers))

% disp(['Length of signal, L = ', num2str(L)])
% disp(['Number of Layers, Lc = ', num2str(Lc)])
% disp(['Number of zeros in padding, z = ', num2str(z)])
46
zz=zeros(1,z); % Vector of zeros to be padded to incoming
               % signal to do it a power of two in length
tt=cat(1, signal, zz'); % New signal vector to be applied to
                        % the QMFB resulting from concatenate
51                        % the original signal with the zeros
NUM_SAMPLES = length(tt); % Length of the new signal

if Tx == 1
    Tx = 'N';
56 else
    Tx = 'Bg';
end
%-----
% -- Filtering the Signal with the QMFB -- (qmfb function)

```

```

61 qmfb_v2(Tx,tt,'tsinc',fs,Dlayer); % Here the function qmfb is
    %    used, it will apply the filter bank to the
    %    signal with the sinc modified filter

end

66 %%%%%%%%%%%%%%%%%%%%%%%%%%%%%%%%%%%%%%%%%%%%%%%%%%%%%%%%%%%%%%%%%%%%%%%%%
%
convertYtoIQ
%
71 % Daniel V. Atienza          EENG 799 -- Fall 2009
%
% file = converted data file from RFSICS
%
function [I Q Fsamp] = convertYtoIQ(file)
76 load(file)
    I = real(Y);
    Q = imag(Y);
    Fsamp = 1/XDelta;
    return
81 %%%%%%%%%%%%%%%%%%%%%%%%%%%%%%%%%%%%%%%%%%%%%%%%%%%%%%%%%%%%%%%%%%%%%%%%%
%
qmfb_v2
%
86 % Originally qmfb.m by Dr.Pace
% Modified by:
% Daniel V. Atienza          EENG 799 -- Fall 2009
%
% filter = tsinc
91 % Tx = 0(off) or 1(on)
% fs = sampling frequency
% Dlayer = desired QMFB layer to analyzed or 0 for all
%          available layers

```

```

%%%%%%%%%%%%%%%%%%%%%%%%%%%%%%%%%%%%%%%%%%%%%%%%%%%%%%%%%%%%%%%%%%%%%%%%
96 function qmfb_v2(Tx,f,filter,fs,Dlayer)

% -- Number of Layers to Compute --
n = floor(log2(length(f))); % Determine the amount of layers
101 % from the length of the signal
% number of layers
if Dlayer == 0
    N = n;
else
106     N = Dlayer;
end
save('N');

%-----
% -- Formatting the Signal -- (to pass the signal through the
111 % filter bank)
I([1:2 .^n],1) = f([1:2 .^n]);
out = I;

%-----
% -- Generating the Output Layers --
116 % w = waitbar(0);
% Decompose the function
for lay = 1:N % layer
% disp(lay) % Show what layer is been generated
flag = 1; % Flag used to set up the columns in the
121 % output matrix
% waitbar(lay/N,w,['Layer Progress - ',...
% num2str(lay), '/', num2str(N)]);
% Reshape the output matrix
[r,c] = size(out);
126 out = zeros(r./2, c.*2);

for i = 1:2 .^(lay-1) % column of I (low to high)

```

```

        [G,H] = feval(filter, I(:,i)); % Evaluate the filter
                                     % (sinc modified) over the
131                                     % signal going by columns

% Setting the output matrix (Layer) by High Pass (G) and
% Low Pass (H) filtering output
    if flag
136        out(:, i.*2-1) = H;%LowPass Branch of QMFB Tree
        out(:, i.*2) = G; %HighPass Branch of QMFB Tree
    else
        out(:, i.*2-1) = G;%HighPass Branch of QMFB Tree
        out(:, i.*2) = H; %LowPass Branch of QMFB Tree
141    end;
        flag = ~flag; % Change in the flag value
    end;

% Output Matrix and data to work with
146 I = out; % Output matrix (signal already filtered)
    R = real(I); % Real part of the filtered signal
    Q = imag(I); % Imaginary part of the filtered signal

SigSize= max(size(f)); %Calculates signal size
151 if Dlayer == 0
    % Saving the data to the same directory
    save([num2str(SigSize)]);
else
    if lay == N
156    % Saving the data to the same directory
        save([num2str(SigSize)]);
    end
end

161 end;
    % close(w)

```

```

%%%%%%%%%%%%%%%%%%%%%%%%%%%%%%%%%%%%%%%%%%%%%%%%%%%%%%%%%%%%%%%%%%%%%%%%
%%%%%%%%%%%%%%%%%%%%%%%%%%%%%%%%%%%%%%%%%%%%%%%%%%%%%%%%%%%%%%%%%%%%%%%%
166 tsinc
%%%%%%%%%%%%%%%%%%%%%%%%%%%%%%%%%%%%%%%%%%%%%%%%%%%%%%%%%%%%%%%%%%%%%%%%
% Code by Dr.Pace
%%%%%%%%%%%%%%%%%%%%%%%%%%%%%%%%%%%%%%%%%%%%%%%%%%%%%%%%%%%%%%%%%%%%%%%%

171 function [d1, c1] = tsinc(c0)    % Sins Modified Filter function
% [d1, c1] = tsinc(c0)
%   Sinc Modified Filter function. It use truncated sinc
%   modified filter coefficients to decompose the column
%   vector c0 into a (high frequency) column vector d1 and
176 %   (low frequency) column vector c1.
%
%   tsinc_su must have been run previously to create h.dat and
%   g.dat files that contain the filter coefficients. That
%   program determines how many coefficients are used.
181
%-----
% -- Load Filter Coefficients (Sinc Modified) --
%
load h.dat;  h = h';
186 load g.dat;  g = g';
%-----
% -- Setting the Signal --
N = length(c0);           % Length of the signal (from qmfb
                           %   function "c0" is a column)
191 pad3 = length(h)./2 + 1; % pad with zeros to clear out filter
c0 = [c0; zeros(pad3,1)]; % padding with zeros
%-----
% Decompose the column vector c0
i = pad3:2:(N+pad3-2);    % i will decimate by 2
196

```

```

% c1 low frequency column vector
c1 = filter(fliplr(h),1,c0);          % compute c1
c1 = c1(i);                          % decimate

201 % d1 high frequency column vector d1
d1 = filter(fliplr(g),1,c0);          % compute d1
d1 = d1(i);                          % decimate
%-----

```

B.2 G-M Process

Listing B.2: Code/GMcode.m

```

% Willie H. Mims          EENG 799 -- Fall 2005/Winter 2006
% Updated and modified by:
% Daniel V. Atienza       EENG 799 -- Fall 2009

5 %function[CTMRnormR CTMRabsnormR]=...
%   GMcode(x,res,Xmatrix,REAL,norm,clr)
%%%%%%%%%%%%%%%%%%%%%%%%%%%%%%%%%%%%%%%%%%%%%%%%%%%%%%%%%%%%%%%%%%%%%%%%
%%% x   = R&Q data Layer name
%%% res = IFFT & FFT resolution
10 %%% Xmatrix: 1=CTM or 2=CSM
%%% REAL: 1=real or 3= magnitude or anything else = complex
%%% Norm: 1=Row power norm, 2=Col power norm
%%%       4=Row amplitude norm, 5=Col amplitude norm
%%%       anything else = baseline
15 %%% clr = 1 or 0 (min the autocorrelation)
%%%%%%%%%%%%%%%%%%%%%%%%%%%%%%%%%%%%%%%%%%%%%%%%%%%%%%%%%%%%%%%%%%%%%%%%

load(x);
Nifft = [64, 128, 256];
20 Nifft = [512, 1024, 2048];
Nifft = Nifft(res);
Nifft = Nifft(res);

```



```

M = R + j*Q;
25 x = M.';

if REAL ==1
    x= real(x);
elseif REAL==3
30     x = abs(x);
end

%%%_Row Normalization before processing_%%%%%%%%%%%%%%
if norm == 1
35     %%%%%%%%% Power Norm (Row)
    r=x;
    rSq = r.^2;
    P = sum(rSq,2)./size(r,2);
    PinvSq = (1./sqrt(P));
40    r1= r;
    for t = 1:size(r,1)
        r1(t,:) = r(t,:).*PinvSq(t);
    end
    x = r1;
45     %%%%%%%%%
elseif norm == 2
    %%%%%%%%% Power Norm (Col)
    r=x;
    rSq = r.^2;
50    P = sum(rSq,1)./size(r,1);
    PinvSq = (1./sqrt(P));

    r1= r;
    for t = 1:size(r,2)
55        r1(:,t) = r(:,t).*PinvSq(t);
    end
    x=r1;

```

```

        %%%%%%%%%
%AMP NORM
60 elseif norm ==4
    %%%_Amp Normalization(Row)
        xNorm = zeros(size(x,1),size(x,2));
        rowMax = max(abs(x),[],2);

65     for t = 1:size(x,1)
        xNorm(t,:) = x(t,:)/rowMax(t);
        end
        x=xNorm;
    elseif norm ==5
70 %%%_Amp Normalization(Col)
        xNorm = zeros(size(x,1),size(x,2));
        colMax = max(abs(x),[],1);
        for t = 1:size(x,2)
            xNorm(:,t) = x(:,t)/colMax(t);
75     end
        x=xNorm;
    end

%%%%%%%%%%%%%%

80 if Xmatrix == 1; % CTM
    X = ifft(x,Nfft,1);
    type = 'CTM';
    trans = 'IFFT';
elseif Xmatrix == 2 % CSM
85     X = fft(x,Nfft,2);
    type = 'CSM';
    trans = 'FFT';
end

90 %%% x = input vector/matrix
    %%% Nfft = Nfft-point inverse DFT of vector x

```

```

%%% Dim = accross dimention
% NOTE: M.' = (row,col)=(freq,time) therefore ifft has to be
%   the col to convert all the freq to time
95
[Row Col] = size(X);
clear CoutC CoutR

% Column-by-Column Correlation
100 CoutC = zeros(Col,Col);    % initialize matrix
    CoutC = X'*X/Row;          % C-by-C correlation

% Row-by-Row Correlation
    CoutR = zeros(Row,Row);    % initialize matrix
105 CoutR = X*X'/Col;          % R-by-R correlation

CTMR = abs(real(CoutR));
CTMC = abs(real(CoutC));
CTMRabs = abs(CoutR);
110 CTMCabs = abs(CoutC);

%%%%%%%%%%%%%%%%%%%%%%%%%%%%%%%%%%%%%%%%%%%%%%%%%%%%%%%%%%%%%%%%%%%%%%%%Minimize diagonal%%%%%%%%%%%%%%%%%%%%%%%%%%%%%%%%%%%%%%%%%%%%%%%%%%%%%%%%%%%%%%%%%%%%%%%%
if clr ==1

115     CTMR_min=min(min(CTMR));
        [CTMR_max CTMR_maxRowLoc]=max(CTMR,[],2);
        CTMRabs_min=min(min(CTMRabs));
        [CTMRabs_max CTMRabs_maxRowLoc]=max(CTMRabs,[],2);

120     for g = 1: length(CTMR)
            CTMR(g,CTMR_maxRowLoc(g))=CTMR_min;
            CTMRabs(g,CTMR_maxRowLoc(g))=CTMRabs_min;
        end
    end
125

```

```

%%%%%%%%%%%%%% Normalize
CTMC_MaxRowVal = max(CTMC,[],2);
CTMCnormR = CTMC;
for w = 1:size(CTMC,1)
130     CTMCnormR(w,:) = CTMC(w,:)/CTMC_MaxRowVal(w);
end

CTMR_MaxRowVal = max(CTMR,[],2);
CTMRnormR = CTMR;
135 for w = 1:size(CTMR,1)
     CTMRnormR(w,:) = CTMR(w,:)/CTMR_MaxRowVal(w);
end

CTMCabs_MaxRowVal = max(CTMCabs,[],2);
140 CTMCabsnormR = CTMCabs;
for w = 1:size(CTMCabs,1)
     CTMCabsnormR(w,:) = CTMCabs(w,:)/CTMCabs_MaxRowVal(w);
end

145 CTMRabs_MaxRowVal = max(CTMRabs,[],2);
CTMRabsnormR = CTMRabs;
for w = 1:size(CTMRabs,1)
     CTMRabsnormR(w,:) = CTMRabs(w,:)/CTMRabs_MaxRowVal(w);
end

```

Bibliography

1. Agilent Technologies. *Agilent E3238 Signal Intercept and Collection Solutions: Family Overview*. Publication 5989-1274EN, USA, 2004.
2. Axelsson, S. R. J. “Noise Radar for range/Doppler processing and digital beam-forming using low-bit ADC”. *Geoscience and Remote Sensing, IEEE Transactions on*, 41(12):2703–2720, 2003.
3. Axelsson, S. R. J. “Noise Radar Using Random Phase and Frequency Modulation”. *Geoscience and Remote Sensing, IEEE Transactions on*, 42(11):2370–2384, 2004.
4. Axelsson, S. R. J. “Random Noise Radar/Sodar With Ultrawideband Waveforms”. *Geoscience and Remote Sensing, IEEE Transactions on*, 45(5):1099–1114, 2007.
5. Dakovic, M., T. Thayaparan, S. Djukanovic, and L. J. Stankovic. “Time-frequency-based non-stationary interference suppression for noise radar systems”. *Radar, Sonar & Navigation, IET*, 2(4):306–314, 2008.
6. Farrell, T. C. and G. Prescott. “A Low Probability of Intercept Signal Detection Receiver Using Quadrature Mirror Filter Bank Trees”. *Acoustics, Speech, and Signal Processing, 1996. ICASSP-96. Conference Proceedings., 1996 IEEE International Conference on*, volume 3, 1558–1561 vol. 3. 1996.
7. Gronholz, B.D., M.A. Temple, R.F. Mills, and T.D Niedzwiecki. “Communication Channel Assessment: Detection of Ultra Wideband Signals Using a Channelized Receiver”. 1071–1076. 2005 IEEE Wireless Communications Conference (WIRECOM05), Jun 2005.
8. Gronholz, Brett D. *Non-Cooperative Detection of Ultra Wideband Signals*. Master’s thesis, Air Force Institute of Technology, GE-ENG-04-29, 2950 Hobson Way, WPAFB, OH, March 2004.
9. Guosui, Liu, Gu Hong, and Su Weimin. “Development of Random Signal Radars”. *Aerospace and Electronic Systems, IEEE Transactions on*, 35(3):770–777, 1999.
10. Hantscher, S., A. Reizenzahn, and C. G. Diskus. “Ultra-Wideband Radar Noise Reduction for Target Classification”. *Radar, Sonar & Navigation, IET*, 2(4):315–322, 2008.
11. Heuschel, Eugene R. *Time-Frequency, Bi-Frequency Detection Analysis of Noise Technology Radar*. Master’s thesis, Navy Postgraduate School, 1 University Circle, Montgomery, CA, September 2006.

12. Horton, B. M. "Noise-Modulated Distance Measuring Systems". *Proceedings of the IRE*, 47(5):821–828, 1959.
13. Kulpa, K. *Continuous Wave Radars Monostatic, Multistatic and Network*, volume 2. Springer, Netherlands, 2006.
14. Kulpa, K., Z. Gajo, and M. Malanowski. "Robustification of Noise Radar Detection". *Radar, Sonar & Navigation, IET*, 2(4):284–293, 2008.
15. Li, Zhixi and R. M. Narayanan. "Doppler Visibility of Coherent Ultrawideband Random Noise Radar Systems". *Aerospace and Electronic Systems, IEEE Transactions on*, 42(3):904–916, 2006.
16. Lievsay, James R. *Simultaneous Range and Velocity Detection with an Ultrawideband Random Noise Radar Through Fully Digital Cross-Correlation in the Time Domain*. Master's thesis, Air Force Institute of Technology, GE-ENG-11-24, 2950 Hobson Way, WPAFB, OH, March 2010.
17. Lukin, K. A., A. A. Mogyla, V. P. Palamarchuk, P. L. Vyplavin, O. V. Zemlyaniy, Y. A. Shiyan, and M. Zaets. "Ka-Band Bistatic Ground-Based Noise Waveform SAR for Short-Range Applications". *Radar, Sonar & Navigation, IET*, 2(4):233–243, 2008.
18. Lukin, K. A. and R. M. Narayanan. "Fifty Years of Noise Radar". *Physics and Engineering of Microwaves, Millimeter and Submillimeter Waves (MSMW), 2010 International Kharkov Symposium on*, 1–3. 2010.
19. Lukin, Konstantin A. "Noise Radar With Correlation Receiver as the Basis of Car Collision Avoidance System". *Microwave Conference, 1995. 25th European*, volume 1, 506–507. 1995.
20. Lyons, R. G. *Understanding Digital Signal Processing*. Prentice Hall, Second edition, 2004. ISBN 978-0-13-108989-1.
21. Mills, R. F. and G. E. Prescott. "A Comparison of Various Radiometer Detection Models". *IEEE Transactions on Aerospace and Electronic Systems*, 32(1):467–473, 1996.
22. Mims, W.H., M.A. Temple, R.F. Mills, and B.D. Grohnolz. "Spectral Sensing Ultra Wideband Signals Using a Down-Converting Channelized Receiver". 706–709. 2005 IEEE Dynamic Spectrum Access Networks Conference (DYSPAN05), Nov 2005.
23. Mims, Willie H. *Wideband Signal Detection Using a Down-Converting Channelized Receiver*. Master's thesis, Air Force Institute of Technology, GE-ENG-06-42, 2950 Hobson Way, WPAFB, OH, March 2006.
24. Narayanan, R. M. "Through-wall radar imaging using UWB noise waveform". *Science Direct, Journal of the Franklin Institute by ElSevier*, 659–678, 2008.

25. Nelms, Matthew E. *Development and Evaluation of a Multistatic Ultrawideband Random Noise Radar*. Master's thesis, Air Force Institute of Technology, GE-ENG-06-42, 2950 Hobson Way, WPAFB, OH, March 2010.
26. Nyquist, Harry. "Thermal Agitation of Electric Charge in Conductors". *Phys. Rev.*, 32:110, 1928.
27. Pace, P. E. *Detecting and Classifying Low Probability of Intercept Radar*. Artech House, Boston, second edition edition, 2008. ISBN 978-1-59693-234-0.
28. Priestly, John A. *AFIT NONET ENHANCEMENTS: SOFTWARE MODEL DEVELOPMENT AND OPTIMIZATION OF SIGNAL PROCESSING ARCHITECTURE*. Master's thesis, Air Force Institute of Technology, GE-ENG-11-34, 2950 Hobson Way, WPAFB, OH, March 2010.
29. Reising, Donald R. *Classifying Emissions From Global System For Mobile (GSM) Communication Devices Using Radio Frequency (RF) Fingerprints*. Master's thesis, Air Force Institute of Technology, GE-ENG-09-37, 2950 Hobson Way, WPAFB, OH, March 2009.
30. Schmitt, Ashley L. *Radar Imaging with a Network of Digital Noise Radar Systems*. Master's thesis, Air Force Institute of Technology, GE-ENG-06-42, 2950 Hobson Way, WPAFB, OH, March 2009.
31. Stephan, R. and H. Loele. "Theoretical and Practical Characterization of a Broadband Random Noise Radar". *Microwave Symposium Digest., 2000 IEEE MTT-S International*, volume 3, 1555–1558 vol.3. 2000.
32. Zhang, Yan and R. M. Narayanan. "Design Considerations for a Real-Time Random-Noise Tracking Radar". *Aerospace and Electronic Systems, IEEE Transactions on*, 40(2):434–445, 2004.

| REPORT DOCUMENTATION PAGE | | | | | Form Approved OMB No. 0704-0188 | |
|--|-------------|-----------------|----------------------------|---|--|--|
| <p>The public reporting burden for this collection of information is estimated to average 1 hour per response, including the time for reviewing instructions, searching existing data sources, gathering and maintaining the data needed, and completing and reviewing the collection of information. Send comments regarding this burden estimate or any other aspect of this collection of information, including suggestions for reducing this burden to Department of Defense, Washington Headquarters Services, Directorate for Information Operations and Reports (0704-0188), 1215 Jefferson Davis Highway, Suite 1204, Arlington, VA 22202-4302. Respondents should be aware that notwithstanding any other provision of law, no person shall be subject to any penalty for failing to comply with a collection of information if it does not display a currently valid OMB control number. PLEASE DO NOT RETURN YOUR FORM TO THE ABOVE ADDRESS.</p> | | | | | | |
| 1. REPORT DATE (DD-MM-YYYY) | | 2. REPORT TYPE | | 3. DATES COVERED (From — To) | | |
| 24-03-2011 | | Master's Thesis | | June 2009-March 2011 | | |
| 4. TITLE AND SUBTITLE Characterization of Noise Technology Radar Signal Detectability Using a Non-Cooperative Receiver | | | | 5a. CONTRACT NUMBER | | |
| | | | | 5b. GRANT NUMBER | | |
| | | | | 5c. PROGRAM ELEMENT NUMBER | | |
| | | | | 5d. PROJECT NUMBER | | |
| 6. AUTHOR(S) Atienza, Daniel V., Captain, USAF | | | | None | | |
| | | | | 5e. TASK NUMBER | | |
| | | | | 5f. WORK UNIT NUMBER | | |
| 7. PERFORMING ORGANIZATION NAME(S) AND ADDRESS(ES) Air Force Institute of Technology Graduate School of Engineering and Management (AFIT/EN) 2950 Hobson Way WPAFB OH 45433-7765 DSN: 785-3636 | | | | 8. PERFORMING ORGANIZATION REPORT NUMBER AFIT/GE/ENG/11-01 | | |
| 9. SPONSORING / MONITORING AGENCY NAME(S) AND ADDRESS(ES) Air Force Research Laboratory, Sensor Directorate Attn: Dr Steven K. Rogers 13th St. Bldg 620 Wright Patterson AFB, OH 45433-7734 DSN: 674-9891, steven.rogers@wpafb.af.mil | | | | 10. SPONSOR/MONITOR'S ACRONYM(S) AFRL/RY | | |
| | | | | 11. SPONSOR/MONITOR'S REPORT NUMBER(S) | | |
| 12. DISTRIBUTION / AVAILABILITY STATEMENT APPROVED FOR PUBLIC RELEASE; DISTRIBUTION UNLIMITED; This material is declared a work of the U.S. Government and is not subject to copyright protection in the United States. | | | | | | |
| 13. SUPPLEMENTARY NOTES | | | | | | |
| 14. ABSTRACT As Noise Technology Radar (NTR) systems emerge, there is a need for non-cooperative, non-matched filter detection and exploitation. This work is based on that need and AFIT's Noise Network (NoNET) radar system. These signals are associated with Low Probability of Detection/ Intercept (LPD/LPI) signals. Quadrature Mirror Filter Banks (QMFB) has been effectively used for non-cooperatively detecting structured LPD/LPI signals and extracting various waveform characteristics. However, the QMFB process performance with unstructured NTR signals was challenging and motivated a need for a transformed QMFB. This transform was based on AFIT research by Gronholz and Mims (G-M), who used a multi-channel receiver containing a bank of Narrowband contiguous filters that span the Ultra Wideband signal bandwidth. Given common LPD/LPI characteristics of UWB and NTR signals, the G-M transformed QMFB with NTR signals proved to be as effective as: 1) For as collected unstructured NTR signals, there was minimal discernible difference between NTR_{OFF} and NTR_{ON} conditions, and detection was very challenging, and 2) For synthesized structured NTR signals, there were distinct differences between NTR_{OFF} and NTR_{ON} conditions with detection occurring through visually-observed features that corresponded to the induced phase features. Overall, the research goal was met-the resultant G-M transformed QMFB is useful for both NTR development (desire to maximize LPD/LPI potential) and exploitation (desire to minimize LPD/LPI potential) research. | | | | | | |
| 15. SUBJECT TERMS Noise Technology Radar (NTR), Noise Network (NoNET), Quadrature Mirror Filter Banks (QMFB), Low Probability of Detection (LPD), Intercept (LPI), Gronholz-Mims (G-M) | | | | | | |
| 16. SECURITY CLASSIFICATION OF: | | | 17. LIMITATION OF ABSTRACT | 18. NUMBER OF PAGES | 19a. NAME OF RESPONSIBLE PERSON | |
| a. REPORT | b. ABSTRACT | c. THIS PAGE | | | Dr. Michael A. Temple (ENG) | |
| U | U | U | UU | 116 | 19b. TELEPHONE NUMBER (include area code) (937)255-3636x4279; email:michael.temple@afit.edu | |